2008

Nanomanufacturing of silica nanowires: Synthesis, characterization and applications

Praveen Kumar Sekhar
University of South Florida

Nanomanufacturing of Silica Nanowires: Synthesis, Characterization and Applications

by

Praveen Kumar Sekhar

A dissertation submitted in partial fulfillment
of the requirements for the degree of
Doctor of Philosophy
Department of Electrical Engineering
College of Engineering
University of South Florida

Major Professor: Shekhar Bhansali, Ph.D.
Rudy Schlaf, Ph.D.
Sanjuktha Bhanja, Ph.D.
Qiang Huang, Ph.D.
Xiao Li, Ph.D.
Robert Elliman, Ph.D.
Kanakasabapathi Subramanian, Ph.D.

Date of Approval:
October 29, 2008

Keywords: nanowires, silica, ion implantation, vapor liquid solid, catalyst

Dedication

This dissertation is dedicated to my family who had patiently supported and encouraged me though out this journey.

Acknowledgements

First and foremost, I would like to express my sincere gratitude to Dr. Shekhar Bhansali for providing me this wonderful opportunity to work in the BioMEMS and Microsystems laboratory. His encouragement, guidance, and direction during my entire stay at University of South Florida (USF) have been invaluable. In addition, his timely motivations have been vital to the success of this research. Next, I would like to thank Dr. Qiang Huang for co-advising me. His suggestions and critique were critical to the success of the National Science Foundation (NSF) funded proposal. Also, I take this opportunity to thank Dr. Rudy Schlaf, Dr. Sanjuktha Bhanja and Dr.Xiao Li for serving as my committee members. I really appreciate their time and consideration in reviewing my dissertation. An industrial perspective to this research was added by Dr.Kanakasabapthi Subramanian from GE Global Research. His critique, comments and feedback were quintessential to the success of this research.

I sincerely thank Prof. Robert Elliman, Head of the Department, for his untiring support, expert guidance and seamless support to the research infrastructure. Also, I take this opportunity to thank Dr.Andrew Wilkinson, Dr.Kidane Belay, David and Tae-Hyun for their peer like support in conducting experiments and analysis. My sincere appreciation and thanks to the senior scientist Dr.Dinesh Sood who ignited the passion for materials research along with his guidance on the nuances of materials characterization and analysis. I would like to thank the funding support from USF MEMS Fellowship, NSF CMMI 0700659, NSF ECCS 0630110 and 0239262 awards. This work would not have been possible without the support of our collaborators – Dr.Tatyana Zhukov (MOFFITT), Dr.Luc Daemen (LANSCE, Los Alamos National Lab) and Dr. Rob Elliman (ANU, Canberra). Last but not the least; I would like to thank present and former members of the BioMEMS and Microsystems group (Dr. Niranjan Ramgir, Dr.Rakesh Joshi, Dr.Senthil Sambandam, Dr.Shyam Aravamudhan, Subramanian, Puneet, Anne Shearrow, Kevin, Rudran, Dorielle Sun Ke, Carl and Johnny) and RF Microsystems group (Dr.Saravana Natarajan and Srinath) for their timely support. Finally, I can not thank enough for the constant support and encouragement from my wife Vidhya Lakshmi.

Note to Reader

The original of this document contains color that is necessary for understanding the data. The original dissertation is on file with the USF library in Tampa, Florida. All the figures have been reproduced with permission from the appropriate publishers.

Table of Contents

List of Tables

List of Figures

Nanomanufacturing of Silica Nanowires: Synthesis, Characterization and Applications

Praveen Kumar Sekhar

ABSTRACT

In this research, selective and bottom-up manufacturing of silica nanowires on silicon (Si) and its applications has been investigated. Localized synthesis of these nanowires on Si was achieved by metal thin film catalysis and metal ion implantation based seeding approach. The growth mechanism of the nanowires followed a vapor-liquid-solid (VLS) mechanism. Mass manufacturing aspects such as growth rate, re-usability of the substrate and experimental growth model were also investigated. Further, silica nanowires were explored as surface enhanced Raman (SER) substrate and immunoassay templates towards optical and electrochemical detection of cancer biomarkers respectively. Investigating their use in photonic applications, optically active silica nanowires were synthesized by erbium implantation after nanowire growth and implantation of erbium as a metal catalyst in Si to seed the nanowires.

Ion implantation of Pd in Si and subsequent annealing in Ar at 1100^0 C for 60 mins in an open tube furnace resulted in silica nanowires of diameters ranging from 15 to 90 nm. Similarly, Pt was sputtered on to Si and further annealed to obtain silica nanowires of diameters ranging from 50 to 500 nm. Transmission electron microscopy studies revealed the amorphous nature of the wires. In addition, nano-sized Pd catalyst was found along the body of the nanowires seeded by Pd implantation into Si. After functionalization of the wires with 3 - AminoPropylTriMethoxySilane (APTMS), the Pd decorated silica nanowires served as an SER substrate exhibiting a sensitivity of 10^7 towards the detection of interleukin-10 (IL-10, a cancer biomarker) with higher spatial resolution. Voltammetric detection of IL-10 involved silica nanowires synthesized by Pd thin film catalysis on Si as an immunoassay template. Using the electrochemical scheme, the presence of IL-10 was detected down to 1fg/mL in ideal pure solution and 1 pg/mL in clinically relevant samples.

Time resolved photoluminescence (PL) results from the Er doped silica nanowires indicate a sharp emission around 1.54 μm representative of the $I_{13/2}$ to $I_{15/2}$ transition in Erbium. Also, a five-fold increase in the PL intensity and 30% augment in luminescence life time have been observed in nanowires when compared to fused silica sample prepared under similar conditions.

The experimental results indicate the potential of silica nanowires in a wide variety of applications such as the development of orthogonal biosensors, fabrication of metallic nanowires, and environmental sensing probes.

Chapter 1

Introduction and Background

In this research, selective and bottom-up manufacturing of silica nanowires on silicon has been investigated. Also, the biosensing and photonic applications of silica nanowires have been explored.

In this chapter, the motivation, goal and objectives of this dissertation have been mentioned. After specifying the research tasks, the salient features observed at nanoscale has been summarized with a view to understand the rationale of this research. Further the various nanocomponents are listed with an insight on the nanowire configuration. Then, a brief introduction to silica nanowires is presented. Finally, the chapter concludes with the organization of the dissertation.

1.1 Motivations

Nanotechnology is poised to induce a paradigm shift in the electronic, chemical, biomedical, sensor and various other industries. Though product commercialization seems to be a challenge [1], prototype testing and proof-of-concept principles have shown the versatility of nanoscience in many applications. The use of nanoscience and related techniques [2] enables superior performance of the device, increased sensitivity levels, faster sensor response and high density synthesis lending to cost-effective manufacturing. The aforementioned properties stems from the fact that nanostructures facilitate unique material properties. Also, a small variation in their dimensions would lead to significant changes in physical, optical and electrical properties resulting in new class of materials and devices. In addition, their large surface-to-volume ratio in combination with their low dimensions makes them ideal candidates to probe events at sub-molecular and atomic scale. One of the areas of nanotechnology is the synthesis of nanomaterials. Different materials, processes and their combinations have been used to manufacture diverse nanostructures [3].

This research has focused on the synthesis of SiO_x nanostructures. Silicon and oxygen are the two most abundant elements in the earths' crust. Their combination as bulk silica has been used in wide variety of MEMS and CMOS applications [4, 5]. Also, the surface of silica can react with various compounds such as amine, carboxyl, or thiol groups to make it functional for bio-sensing applications [6]. The ease with which the silica surface can be modified physically and chemically has resulted in wide variety of applications, specifically in biosensing and bioanalysis [7]. Few reports exist on the synthesis of silica nanowires and their applications in comparison to the vast scientific literature on various form of bulk silica [8]. In this context, this research concentrates on bottom-up manufacturing of silica nanowires with emphasis on their optical and biosensing applications.

1.2 Goal

The goal of this research was to explore a combination of engineered techniques for bottom-up and controlled synthesis (nanomanufacturing) of silica nanowires for diverse applications. As nanowires are building block of any nanosystem, the ability to synthesize them at a desired location in a controlled manner, is of great importance. The central focus of this research was to address the need for selective and bottom-up nucleation of silica nanowires on silicon through detailed investigations on growth methodologies targeting high yield synthesis. Exploring the real-time applications would be an integral research thrust in addition to their bottom-up growth.

1.3 Objectives

There exist different nucleation mechanisms for manufacturing SiO_2 nanowires [9]. Bottom– up synthesis of these nanowires mediated by vapor liquid solid (VLS) mechanism lends to mass manufacturing aspects and creation of hybrid nanosystems (metal-dielectric) via VLS imparts the multi-functional attribute to these dielectric nanostructures [10]. The intellectual merit of such a growth model has been undermined by a lack of engineered techniques to manufacture site-specific nanostructures with good reproducibility. The objective of this research was to investigate simple, reliable and reproducible engineered techniques for selective and bottom-up manufacturing of silica nanowires on silicon.

The objectives were accomplished by:-

(a) Studying in detail the bottom-up, VLS-based growth of silica nanowires on Si with comprehensive understanding of its nucleation mechanism,

(b) Characterization of these engineered nanowires along with their surface modification schemes (doping and chemical functionalization), and

(c) Exploring the potential of silica nanowires for real-time applications

Figure 1.1 illustrates the objective of the current research.

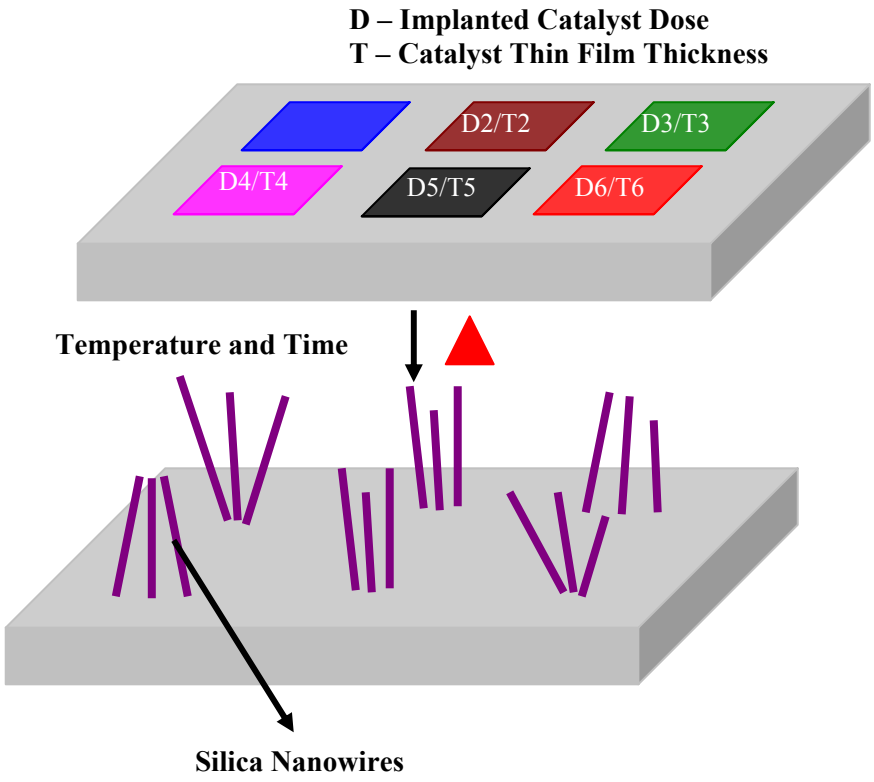

Figure 1.1 Bottom-Up Synthesis of Silica Nanowires

1.4 Research Tasks

The research objectives were achieved by investigating the metal catalysis for selective and controlled nucleation of silica nanowires on Si involving detailed investigation on the early growth stage of the wires, and the feasibility of mass manufacturing. Also, the study of nanowire growth variables governing the structure and morphology of the nanowires were performed. Characterization of silica nanowires using scanning and transmission electron microscopy and X-Ray diffraction to extract information on the surface profile, morphology and texture of the wires respectively were an integral part of the research tasks. Infra-red and Raman spectroscopy were carried out with a view to identify the structural functionality of the wires. Further, the potential applications of silica nanowires were investigated. Surface functionalization of the wires with silane chemistry led to bio-diagnostics while doping them with optically active rare earth materials resulted in Er sensitization.

1.5 Significance of the Current Research

(a) Characterization

The structure and morphology of the nanowires from "early nucleation" to "full growth" stage was used to identify the size and shape anisotropy. The surface inspection at lower magnification was used to estimate the average diameter, number density, and aspect ratio of the nanowires (which govern the physical, optical and material properties). An assessment at higher magnification was essential to identify heterostructures. Along with microscopic details, structural verification using IR and Raman spectroscopy provided supplemental information on the functionality.

(b) Doping and Functionalization - Surface Modification

Ion beam doping methods and chemical functionalization transforms engineered silica nanowires into active structures. The small lateral dimension of nanowires combined with their large surface-to-volume fraction was expected to impede the dopant (element, gas or compound) penetration within one wavelength of the surface. As a consequence, the evanescent field from these emitting centers would extend beyond the nanowire surface and could interact with adsorbed atoms or molecules, or indeed with the surrounding ambient. Such surface modifications were noticed to have a direct influence on sensing and photonic applications.

1.6 Salient Features at Nanoscale

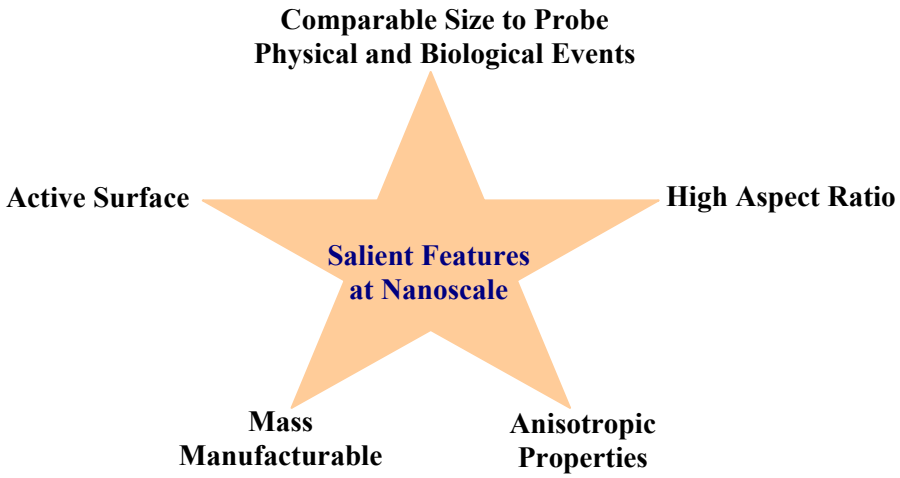

Figure 1.2 Salient Features at Nanoscale Dimensions

Figure 1.2 highlights the salient features at nanoscale dimensions. They are as follows: -

(a) Comparable Size

The dimensions of nanostructures are comparable to the size of biomolecule (such as proteins, Vander Waals' force, pharmokinetics, surface dynamics, and diffusion and transport mechanisms. Such an attribute makes them as sensitive probes to unravel atomistic and molecular events with great accuracy.

(b) High Surface to Volume ratio

Ratio of the surface area to total volume is a direct measure of reactivity for any system/material. When volume is too large relative to surface area, diffusion cannot occur at sufficiently high rates as molecules/particles take time to reach the active surface. An increased surface area to volume ratio means increased exposure to the environment, which in turn translates as a sensitive surface to minor surface perturbations. In addition, high surface area to volume ratio provides the required acceleration to negotiate thermodynamic barriers thereby minimizing free energy. Also, nanostructures possess high surface to volume ratio facilitating faster diffusion mechanism.

(c) Anisotropic Configuration and Tunability

One and two-dimensional nanostructures are generally high aspect ratio arrangements with size [11] and directionality (along various axes) dependent [12] material properties. For example, the deflection or absorbance of incident light, mechanical property like Youngs' Modulus or magnetic property like hysteresis would change with orientation.

(d) Active Surface

The diminutive sizes of nanoscale materials enable the entry of foreign materials through adsorption and diffusion, favor specific chemical interaction, and induce physisorption [13] by acting as templates. Collectively coining the above-mentioned features as 'Doping and Functionalization', nanostructures present an active surface for implementing various applications.

(e) Mass Manufacturing

The advancements in semiconductor manufacturing in combination with precision metrology have enabled high-density synthesis of nanostructures at a faster rate to achieve the real promise of developing and manufacturing new nanomaterials, devices, and products in a cost-effective manner.

1.7 Applications

Nanotechnology has been employed in a plethora of applications in wide variety of disciplines ranging from clinical products to automotive industries to food packaging and space explorations [14]. Presting et al. [15] has reported the nanotechnology developments for automotive applications. In the automotive trade, the use of nanoscience and technology ranges from the light-weight construction of power trains, energy conversion, pollution sensing and reduction, interior cooling, wear reduction, driving dynamics, and surveillance control, recycle potential and much more. Figure 1.3 lists the diverse application of nanotechnology.

Ranking (Score)	Applications of Nanotechnology	Examples	Comparison with the MDGs
1 (766)[a]	Energy storage, production, and conversion	Novel hydrogen storage systems based on carbon nanotubes and other lightweight nanomaterials Photovoltaic cells and organic light-emitting devices based on quantum dots Carbon nanotubes in composite film coatings for solar cells Nanocatalysts for hydrogen generation Hybrid protein-polymer biomimetic membranes	VII
2 (706)	Agricultural productivity enhancement	Nanoporous zeolites for slow-release and efficient dosage of water and fertilizers for plants, and of nutrients and drugs for livestock Nanocapsules for herbicide delivery Nanosensors for soil quality and for plant health monitoring Nanomagnets for removal of soil contaminants	I, IV, V, VII
3 (682)	Water treatment and remediation	Nanomembranes for water purification, desalination, and detoxification Nanosensors for the detection of contaminants and pathogens Nanoporous zeolites, nanoporous polymers, and attapulgite clays for water purification Magnetic nanoparticles for water treatment and remediation TiO_2 nanoparticles for the catalytic degradation of water pollutants	I, IV, V, VII
4 (606)	Disease diagnosis and screening	Nanoliter systems (Lab-on-a-chip) Nanosensor arrays based on carbon nanotubes Quantum dots for disease diagnosis Magnetic nanoparticles as nanosensors Antibody-dendrimer conjugates for diagnosis of HIV-1 and cancer Nanowire and nanobelt nanosensors for disease diagnosis Nanoparticles as medical image enhancers	IV, V, VI
5 (558)	Drug delivery systems	Nanocapsules, liposomes, dendrimers, buckyballs, nanobiomagnets, and attapulgite clays for slow and sustained drug release systems	IV, V, VI
6 (472)	Food processing and storage	Nanocomposites for plastic film coatings used in food packaging Antimicrobial nanoemulsions for applications in decontamination of food equipment, packaging, or food Nanotechnology-based antigen detecting biosensors for identification of pathogen contamination	I, IV, V
7 (410)	Air pollution and remediation	TiO_2 nanoparticle-based photocatalytic degradation of air pollutants in self-cleaning systems Nanocatalysts for more efficient, cheaper, and better-controlled catalytic converters Nanosensors for detection of toxic materials and leaks Gas separation nanodevices	IV, V, VII
8 (366)	Construction	Nanomolecular structures to make asphalt and concrete more robust to water seepage Heat-resistant nanomaterials to block ultraviolet and infrared radiation Nanomaterials for cheaper and durable housing, surfaces, coatings, glues, concrete, and heat and light exclusion Self-cleaning surfaces (e.g., windows, mirrors, toilets) with bioactive coatings	VII
9 (321)	Health monitoring	Nanotubes and nanoparticles for glucose, CO_2, and cholesterol sensors and for in-situ monitoring of homeostasis	IV, V, VI
10 (258)	Vector and pest detection and control	Nanosensors for pest detection Nanoparticles for new pesticides, insecticides, and insect repellents	IV, V, VI

[a] The maximum total score an application could receive was 819.

DOI: 10.1371/journal.pmed.0020097.t001

Figure 1.3 Various Applications of Nanotechnology

(Reproduced with Permission, [16])

1.8 Nanocomponents

Based on the structure and morphology of the nanostructures, the nanocomponents could be broadly classified as:-

1.8.1 Nanoparticles

Particles or substance of zero dimensions whose size is less than 100 nm are classified as nanoparticles. The percentage of atoms at their surface is very high compared to bulk materials leading to unexpected yet interesting properties. For example, ferroelectric nanoparticles could switch their magnetization at room temperature or show hysteresis making them useless for memory storage [17]. Figure 1.4 [18] is a scanning electron micrograph (SEM) image of Au nanoshells of 100 nm in diameter.

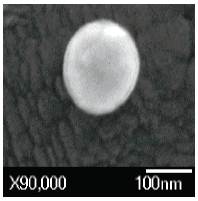

Figure 1.4 SEM Image of an Au Nanoshell
(Reproduced with Permission, [18])

1.8.2 Nanowires / Nanorods

Nanowires are structures with lateral size in nanoscale dimensions and unconstrained longitudinal geometry. They are the preferred nanocomponents over others due to the better electron transport capabilities aided by the quantum confinement [19]. The atomic energy levels in nanowires are different from the traditional continuum of energy levels or bands found in bulk materials. Figure 1.5 [20] shows ZnO nanowires on alumina substrate.

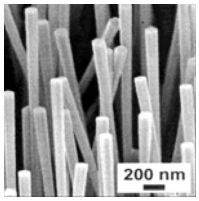

Figure 1.5 SEM Image of the ZnO Nanowires on Alumina Substrate
(Reproduced with Permission, [20])

1.8.3 Nanotubes

A variant of nanowires which are characterized by hollow cylindrical shape structure similar to a co-axial arrangement. Figure 1.6 [21] is a transmission electron microscopy (TEM) image of silica nanotubes.

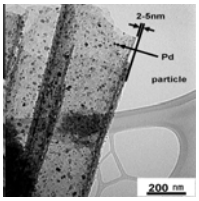

Figure 1.6 TEM Image of Pd Doped Silica Nanotubes
(Reproduced with Permission, [21])

1.8.4 Nano – Thin Films

If the thin film is of thickness less than 10 nm and subsequent grain size of the deposited material does not exceed 10 nm, it is referred to as a nanothin film. Figure 1.7 [22] show scanning electron micrograph of a nanocrystalline diamond thin film.

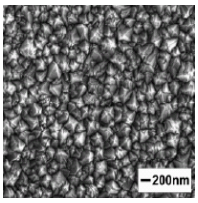

Figure 1.7 SEM Micrograph of the Nanocrystalline Diamond Thin Film
(Reproduced with Permission, [22])

1.8.5 Applications of Nanocomponents

Each nanocomponent has several applications in different sectors. For example, Mirkin et al. summarized the following the applications of nanoparticles in medicine [23]:-

(a) Smart metallic and semiconducting nanoparticles for cancer therapy and imaging
(b) Targeted magnetic nanoparticles for brain tumor imaging and therapy
(c) Porous nanoparticles for drug delivery
(d) Enzyme-sensitive nanoparticle coatings for screening tumor
(e) Polymer nanoparticles and quantum dots for siRNA delivery
(f) Next-generation magnetic nanoparticles for multimodal, non-invasive tumor imaging
(g) Low-toxicity nanocrystal quantum dots for biomedical imaging
(h) Bio-barcodes to detect ovarian cancer markers
(i) A new class of drugs that will inhibit or reduce metastasis
(j) Bioactivated nanoprobes for molecular imaging of cancer

1.9 Nanowires: Introduction

Among the several nanocomponents, nanowires have been preferred for many functional applications due to their efficient transport of electrons [24], structural anisotropy and the possibility of quantum confinement.

1.10 Nanowires: Classification

Based on the electrical conductivity of the nanowires, they are broadly classified as metallic, semiconducting and insulating. Some of the reported configurations of metallic nanowires are that of Au, Ag, Ni, Pd and Co, while Si, ZnO, SnO_2, and GaN forms the repertoire of semiconducting nanowires. SiO_2 nanowires form the part of insulating nanowires. Table 1.1 lists the applications of semiconducting nanowires.

Table 1.1 Applications of the Semiconducting Nanowires

Nanowire Composition	Applications
Si	(a) Anode material for lithium ion batteries [25] (b) Biosensors [26] (c) Field Effect Transistors [27] (d) Photovoltaics [28] (e) Thermoelectric Material [29]
ZnO	(a) Gas Sensor [30] (b) Laser Source [31] (c) Chemical and Biological Sensors [32] (d) Material for Energy Harvesting [33]
C	(a) Reinforcements for Sports Equipment, concrete and combat jackets [34] (b) Photovoltaics [35] (c) Energy Efficient Displays [36]
III-IV Semiconducting Materials	(a) Solar Cell Materials [37]

1.11 Silica Nanowires

Bulk Si has been used in wide variety of applications stemming from the fact that they can be doped to alter the resistivity and optical properties. However, the luminescence efficiency of Si is low. However, silica as an insulating medium has been exploited to guide electromagnetic waves due to its low refractive index.

Also, bulk silica has been used in a plethora of applications [38] such as:-

(a) An insulating medium in CMOS circuits,

(b) Barrier to prevent interfacial reactions in high temperature processing,

(c) Dielectric matrices/medium for synthesis of new materials as well as plasmonic applications,

(d) Masking material for high energy processes while offering a chemically compatible surface for etching applications, and

(e) Cell culture medium and biocompatible surface for developing in-vitro and in-vivo biosensors

Silica nanostructures have been manufactured in a variety of distinct topological forms (e.g. nanopores, nanospheres, nanowires, nanotubes, nanosprings etc….) giving rise to applications in optics, biosensing/clinical diagnostics, and catalysis and developing composites [39].

In general, silica nanostructures are known to possess characteristic structural properties (e.g., two-membered SiO_2 rings [40], non-bridging oxygen (NBO) defects [41]) quite unlike those of the bulk, which is often reflected in their physical/chemical properties. Recently, for example, silica nanowires and nanotubes have been shown to be intense blue/visible light emitters [42], which have been linked to structurally non-stoichiometric defect centers.

Recently, Mazurs' group [43] fabricated long freestanding silica nanowires using 'Taper Drawing' process with diameters down to 50 nm that show atomic-level surface smoothness and excellent diameter uniformity. The length of the wires was estimated to be in tens of millimeters, giving them an aspect ratio larger than 50,000. It was shown that light can be launched along these wires by optical evanescent coupling. The wires enable single-mode operation and have very low optical losses within the visible to near-infrared spectral range. Also, mechanical tests show that the wires have tensile strength in excess of 5 GPa. The wires were also resilient and flexible, easily bending into microscopic loops.

In contrast, silica nanotubes (SNTs) have proven to be a multifunctional nanostructure for biomedical applications such as drug delivery and bioseparation. He et al. [44] described the synthesis of well-controlled shape-coded SNTs and their biosensing applications.

It is mentioned that the shape coded SNTs can be easily identified by their different shapes (codes) using a conventional optical microscope. Because of the low density and high surface area of the hollow tubular structure compared to those of the spherical and rod structures, SNTs can be suspended and are stable in solution.

1.11.1 Active Silica Nanowires

Silica nanowires have become multi-functional in nature due to the viability in surface modification procedures such as doping and functionalization. Optical applications evolve from doping silica nanowires [45].

Their dominance in biosensing is due to the chemical treatment with silane [46]. Such a surface modification scheme is referred to as 'functionalization' which would be discussed in the forthcoming sections.

1.11.2 Doping

Doping is a simple route to modulate the surface properties of materials to attach specific functionalities for variety of applications. Semiconductor industry has relied on diffusion and ion implantation as techniques to incorporate defects or dopants into bulk medium. Both the mechanisms have the potential to alter the physical, electrical, optical and mechanical properties of materials. While diffusion is a high temperature thermal process where in the impurities either converted into vapor or as a melt to enter host, implantation involves bombardment of ions with high energy and velocity to embed into the host. Table 1.2 highlights the salient features of both the techniques listed with their advantages and disadvantages.

Table 1.2 Comparison of Ion Implantation and Doping Processes

Ion Implantation	**Diffusion**
Advantages	Advantages
(a) Accurate Dose and Depth Control (b) Several dopants may be added simultaneously (c) Room Temperature Process (d) Ease in selective placement of dopants beneath a mask (e) Minimal lateral spread of dopants beneath the mask	(a) Relatively Low Cost (b) Simple Equipment
Disadvantages	Disadvantages
(a) High Capital Costs (b) Channeling may occur and distort the doping profile (c) Radiation Damage – Annealing Preferred	(a) Limited choice of ions and dopants (b) High Temperature Process (c) High Lateral Diffusion (d) 4. Diffusion sensitive to dislocations and grain boundaries

Doping is critical in creating functional or active nanostructures. One of the promising applications of doping in silica based structures has been in optical communication with the inclusion of Er as the impurity [47]. Erbium is of particular interest because of its intra-4f transition with a wavelength around 1.54 μm that coincides with the low-loss window of standard optical telecommunications silica fiber. When incorporated in a trivalent state (Er^{3+}) in a solid host, these ions exhibit relatively sharp optical transitions corresponding to the intra-4f states [48]. As mentioned earlier, using implantation, the dopant profile could be accurately tuned on nano/micron depth scale critical to the development of optical waveguides, and other integrated optical structures. Doping of silica based nanostructures with erbium would be an interesting set of engineered modifications that could revolutionize optical communication.

1.11.3 Functionalization

Attaching functional surface through chemical treatments for a specific intent is referred to as functionalization. Generally, this concept has been applied to nanostructures for developing ultra-sensitive biosensors. The bioscreening process primarily involves the detection of antigens and antibodies. Antibodies [49] are proteins found in blood used by the immune system to identify and neutralize foreign objects such as bacterias and viruses. The general structure of all antibodies is very similar except for a small region at the tip of the protein which is extremely variable and posses a unique morphology. This region is known as the hypervariable. Each of these variants can bind to a different target, known as an antigen (generally a protein that prompts the generation of antibodies and initiates an immune response). The binding mechanism is very similar to the 'Lock and Key' principle. Such antibody-antigen combination has enabled a comprehensive library and subsequent protocols for pathogen detection. Nanostructures aid in improving the binding and areal density of the capture sites there by enhancing the detection sensitivity with minimal sample volume.

An organic group which has often been used for functionalization is 3-aminopropyl moiety. It is a primary amine that can immobilize catalytically active transition metal ions. In addition, the nucleophilic primary amine can also be used as linker between the silica surface and any organic species with a leaving group for a nucleophilic substitution reaction or serve as a solid base catalyst. The 3-aminopropyltrimethoxy silane functionalized materials or in short "APTMS" functionalized silica surface had showed a very high stability, according to earlier reports [50]. Figure 1.8 highlights the silica-amine functionalization scheme. Hence, silica based structures are candidate material for biosensing applications. Furthermore, nanoscale features of silica would enable unprecedented levels of sensitivity.

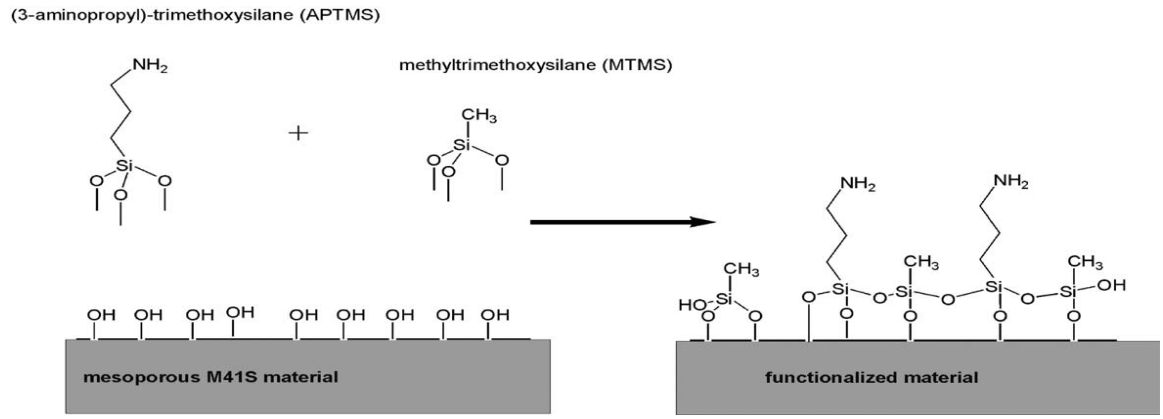

Figure 1.8 Silica – APTMS/MTMS Functionalization Scheme
(Reproduced with Permission, [37])

1.12 Dissertation Structure

In this thesis, selective and bottom-up growth of silica nanowires on silicon has been envisioned using nanoengineered techniques.

Chapter 2 reviews the nucleation techniques in synthesizing nanowires and in particular, the VLS mechanism. The kinetics, salient features, advantages and challenges of this bottom-up approach has been discussed in detail. Finally, the current state of the art in growing silica nanowires has been mentioned.

Chapter 3 lists the experimental materials and methods used in this research investigation which includes the description and basic principles of ion implantation, spectroscopic characterization methods, texture analysis by x-ray diffraction (XRD) and morphological inspection by scanning and transmission electron microscopy methods.

Chapter 4 engages in the discussion of the experimental results by the author. The publications focus on the selective growth of silica nanowires on Si followed by the manufacturing aspects of silica nanowire. Then the use of metal decorated silica nanowires as a SER (surface enhanced Raman) substrate has been discussed. Further , silica nanowires as an efficient immunoassay template and superior Er sensitizer has been demonstrated.

Chapter 5 details on the future work and the subsequent research thrusts on the growth of vertically aligned silica nanowires of uniform geometry, low temperature synthesis on non-Si substrate along with the discussion of nano-bio interface studies using silica nanowires.

1.13 Summary

This chapter presented the motivation, goal, objectives and significance of the current research. An overview of nanoscience with details on its evolution, salient features and applications was also mentioned. Further, nanostructures of various morphologies have been discussed. Then, nanowires of different materials with potential applications have been reported.

1.14 References

[1] L.Mazzola, "Commercializing Nanotechnology", Nature Biotechnology 21 (2003), 1137

[2] E.Hood, "Nanotechnology: Looking as we Leap", Environmental Health Perspective 112 (2004), A740

[3] Z. W.Pan, Z. R.Dai, and Z.L.Wang, "Nanobelts of Semiconducting Oxides", Science 291 (2001), 1947

[4] J.Buhler, F-P.Steiner and H.Baltes,"Silicon dioxide Sacrificial Layer Etching in Surface Micromachining", Journal of Micromechanics and Microengineering, 7 (1997), R1

[5] P.K.Roy and I.C.Kizilyalli, "Stacked High-ε Gate Dielectric for Gigascale Integration of Metal–Oxide–Semiconductor technologies", Applied Physics Letters 72 (1998), 2835

[6] W.Tan, K.Wang, X.He, X.J.Zhao, T.Drake, L.Wang and R.P.Bagwe, "Bionanotechnology based on Silica Nanoparticles", Medicinal Research Reviews 24(2004), 621

[7] M.Etienne and A.Walcarius, "Analytical Investigation of the Chemical Reactivity and Stability of Aminopropyl-Grafted Silica in Aqueous Medium", Talanta, 59 (2003), 1173

[8] W. Tan, K. Wang, X. He, X.J. Zhao, T. Drake, L. Wang, and R.P. Bagwe, "Bionanotechnology based on silica nanoparticles", Medicinal Research Reviews 24 (2004), 621

[9] S.T. Lee, N. Wang and C.S. Lee, "Semiconductor nanowires: synthesis, structure and properties", Materials Science and Engineering A 286 (2000), 16

[10] S.M. Prokes, O.J. Glembocki, R.W. Rendell, and M.G. Ancona, "Enhanced plasmon coupling in crossed dielectric/metal nanowire composite geometries and applications to surface-enhanced Raman spectroscopy", Applied Physics Letters 90 (2007), 093105

[11] R.E. Miller and V.B. Shenoy, "Size-dependent elastic properties of nanosized structural elements", Nanotechnology 11 (2000), 139

[12] A.J.Kulkarni, M.Zhou, and F.J.Ke, “Orientation and Size Dependence of the Elastic Properties of Zinc Oxide Nanobelts”, Nanotechnology16 (2005), 2749
[13] Y.X.Yang, R.K.Singh, and P.A.Webley, “Hydrogen Adsorption in Transition Metal Carbon Nanostructures”, Adsorption 14 (2008), 265
[14] www.caer.uky.edu/factsheets/cfc_UGnanowires.pdf
[15] H.Presting and U.Konig, “Future nanotechnology developments for automotive applications”, Materials Science and Engineering C 23(2003), 737
[16] Fabio Salamanca-Buentello, Deepa L. Persad, Erin B. Court, Douglas K. Martin, Abdallah S. Daar, and Peter A. Singer, “Nanotechnology and the Developing World”, PloS Medicine 2 (2005), 0383
[17] I. Apostolova and J.M. Wesselinowa, “Magnetic control of ferroelectric properties in multiferroic BiFeO3 nanoparticles”, Solid State Communications 147 (2008), 94
[18] C.L.Nehl, N.K.Grady, G.P.Goodrich, F.Tam, N.J. Halas, and J.H. Hafner, “Scattering Spectra of Single Gold Nanoshells”, Nano Letters 4(2004), 2355
[19] http://news-info.wustl.edu/tips/page/normal/420.html
[20] S. C.Lyu, Y.Zhang, C. J.Lee, H.Ruh, and H. J.Lee, “Low-Temperature Growth of ZnO Nanowire Array by a Simple Physical Vapor-Deposition Method”, Chemistry of Materials 15 (2003), 3294
[21] J.H.Jung, J.A. Rim, S.J.Lee, S.J.Cho, S.Y.Kim, J.K.Kang, Y.M.Kim and Y.J.Kim, “Pd Doped Double-Walled Silica Nanotubes as Hydrogen Storage Material at Room Temperature”, Journal of Physical Chemistry C 111 (2007), 2679
[22] W.Yang, S.E.Baker, C-S.Lee, J.N.Russell, L.Shang, B.Sun, and R.J.Hamers, “Electrically Addressable Biomolecular Functionalization of Conductive Nanocrystalline Diamond Thin Films”, Chemistry of Materials 17 (2005), 938
[23] J-M.Nam, C.S.Thaxton, and C.A.Mirkin, “Nanoparticle-Based Bio-Bar Codes for the Ultrasensitive Detection of Proteins”, Science 301 (2003), 1884
[24] J.Hu, T.W.Odom and C.M.Lieber, “Chemistry and Physics in One Dimension: Synthesis and Properties of Nanowires and Nanotubes”, Accounts of Chemical Research 32 (1999), 435
[25] K-H. Lee, “Synthesis of Si Nanowires for an Anode Material of Li Batteries”, Pentagon Reports, Report Number: A057474, Contract Number: FA48690610092
[26] Y.Cui, Q.Wei, H.Park, and C.M. Lieber, “Nanowire Nanosensors for Highly Sensitive and Selective Detection of Biological and Chemical Species”, Science 293 (2001), 1289

[27] Y.Cui, Z.Zhong,D.Wang,W.U.Wang, and C.M. Lieber, “High Performance Silicon Nanowire Field Effect Transistors”, Nano Letters 3 (2003) 149
[28] A.Boukai, Y.Bunimovich, J.Tahir-Kheli, J-K.Yu, W.A.Goddard and J.R.Heath, “Silicon nanowires as Efficient Thermoelectric Materials”, Nature 451 (2008), 168
[29] K.Peng, Y. Xu , Y.Wu , Y.Yan , S.T.Lee , and J.Zhu , “Aligned single-crystalline Si nanowire arrays for photovoltaic applications”, Small. 1 (2005), 1062
[30] Y.W. Heo, D.P. Norton, L.C. Tien, Y. Kwon, B.S. Kang, F. Ren, S.J. Pearton, and J.R. LaRoche, “ZnO nanowire growth and devices”, Materials Science and Engineering R 47 (2004), 1
[31] J.C.Johnson, H.Yan, R.D.Schaller, L.H.Haber, R.J.Saykally and P.Yang, “Single Nanowire Lasers”, Journal of Physical Chemistry B: Letters 105 (2001), 11387
[32] J.S.Kim, W.Park, C-H.Lee and G-C.Yi, “ZnO Nanorod Biosensor for Highly Sensitive Detection of Specific Protein Binding”, Journal of the Korean Physical Society 49 (2006), 1635
[33] Z.L.Wang and J.Song, “Piezoelectric Nanogenerators Based on Zinc Oxide Nanowire Arrays”, Science 312 (2006), 242
[34] T.W. Ebbesen, “Carbon Nanotubes”, Annu. Rev. Mater. Sci. 24 (1994), 235
[35] J.U. Lee, “Photovoltaic Effect in Ideal Carbon Nanotube Diodes”, Applied Physics Letters 87 (2005), 073101
[36] R.H.Baughman, A.A.Zakhidov and W.A.de Heer, “Carbon Nanotubes – Route towards Applications, Science 297 (2002), 787
[37] H. A Nilsson, T.Duty, S.Abay, C.Wilson, J. B.Wagner, C.Thelander, P.Delsing and L. Samuelson, “A Radio Frequency Single-Electron Transistor Based on an InAs/InP Heterostructure Nanowire”, Nano Letters 8(2008), 872
[38] http://www.azom.com/details.asp?ArticleID=1114
[39] http://www.unisci.com/stories/20021/0306025.htm
[40] C.Xu, X-F.Zhang, L.Chen and J.Cao, “Effect of polar groups on Raman spectrum of one dimension SiO_2 nanowires”, Journal of Molecular Structure: Theochem 851 (2008), 35
[41] A.S. Zyubin, Yu.D. Glinka, A.M. Mebel, S.H. Lin, L.P. Hwang and Y.T. Chen, “Red and near-infrared photoluminescence from silica-based nanoscale materials: Experimental investigation and quantum-chemical modeling”, J. Chem. Phys. 116 (2002), 281
[42] D. P. Yu, Q. L. Hang, Y. Ding, H. Z. Zhang, Z. G. Bai, J. J. Wang, Y. H. Zou, W. Qian, G. C. Xiong, and S. Q. Feng, “Amorphous silica nanowires: Intensive blue light emitters”, Applied Physics Letters 73 (1998), 3076

[43] L.Tong R.R. Gattass, J.B. Ashcom, S.He, J.Lou, M.Shen, I.Maxwell and E.Mazur, "Subwavelength-diameter silica wires for low-loss optical wave guiding", Nature (2003) 426, 816
[44] B.He, S.J.Son, and S.B.Lee, "Shape-Coded Silica Nanotubes for Biosensing", Langmuir 22 (2006), 8263
[45] http://mazur-www.harvard.edu/research/detailspage.php?rowid=11
[46] M.V. Emon, "Immunoassay and Other Bioanalytical Techniques", CRC Press (2007)
[47] P.C. Becker, N.A. Olsson, and J.R. Simpson, "Erbium-doped Fiber Amplifiers: Fundamentals and Technology", Academic Press (1991)
[48] A. Taguchi and K. Takahei, "Erbium in Si: Estimation of energy transfer rate and trap depth from temperature dependence of intra-4*f*-shell luminescence", J. Appl. Phys. 83 (1998), 2800
[49] http://www.biology.arizona.edu/IMMUNOLOGY/tutorials/antibody/structure.html
[50] M.Luechinger, R.Prins, and G.D.Pirngruber, "Functionalization of silica surfaces with mixtures of 3-aminopropyl and methyl groups", Microporous and Mesoporous Materials 85 (2005) 111

Chapter 2

Review of Nucleation Techniques

Understanding the growth mechanisms of nanowires is vital for their high density synthesis. Also, the growth mechanism dictates the structure and morphology of the nanostructures. In this context, this chapter gives a brief introduction on the nucleation techniques for nanowire growth followed by the review on the VLS mechanism. Further, the current state of the art for silica nanowire growth has been mentioned.

2.1 Nucleation Techniques: Top Down and Bottom Up

There exist two generic methods for the growth of nanostructures namely 'Top-Down (TD)' and 'Bottom-Up (BU)' approach. TD is a fabrication method which includes machining and etching techniques. Subtractive processes remove the material to scale them down to nanoscale regime. Templated method and electrodeposition falls in the category of TD approaches in the formation of nanowires. Whereas, BU approach is an additive process which builds on material from an atomic scale (molecule by molecule or atom by atom) to evolve one dimensional nanostructures. Bottom-up approaches include vapor phase growth, solution grown mechanism, oxide assisted growth, carbo-thermal reduction technique and self-assembly process.

2.1.1 Top Down: Templated Method

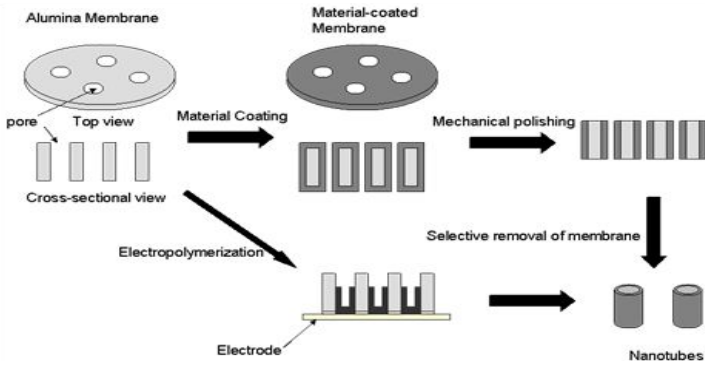

Figure 2.1 Schematic of the Template Synthesis Procedure
(Reproduced with Permission, [1])

Figure 2.1 schematically illustrates the templated synthesis methodology. The 'template' is a fundamental structure within which a network forms. Removal of templates leaves a filled cavity with morphology and structural details of those related to the template. Various pre-defined structures such as polymer membranes, anodic alumina and porous silicon of fixed geometry have been used as templates. Once the template is fabricated, nanowires of desired geometry (diameter dictated by the pore size and length determined by the pore length) are derived. Electrochemical methods, electroless techniques, chemical vapor deposition (CVD), sol-gel and chemical polymerization based deposition mechanism are used to fill the pores. The porous part or the scaffold is selectively removed using appropriate etching chemistry leaving behind the nanowires. The template method is convenient and simple. Nanowires of different compounds can be easily produced harnessing the properties pertaining to specific applications. The main drawbacks of this method are the inability to produce single crystalline wires and limited geometries (i.e. fixed diameter and length).

The template method is convenient and simple. Nanowires of different compounds can be easily produced harnessing the properties pertaining to specific applications. The main drawbacks of this method are the inability to produce single crystalline wires and limited geometries (i.e. fixed diameter and length).

2.1.2 Top Down: Electrodeposition Method

A wide range of materials can be deposited by electrodeposition, including metals, alloys, metal oxides, semiconductors, and conducting polymers. Electrochemical deposition is performed by using the electroplating solution as the electrolyte. When an electrical potential is applied between the electrodes, deposition takes place at the working electrode similar to galvanization. Figure 2 [2] illustrates the templated assisted electrodeposition process.

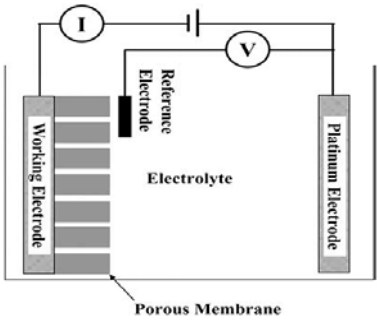

Figure 2.2 Templated Assisted Electrodeposition Process
(Reproduced with Permission, [2])

Another version is known as Step-Edge Decoration on HOPG (Highly Ordered Pyrolytic Graphite) substrate [3, 4].

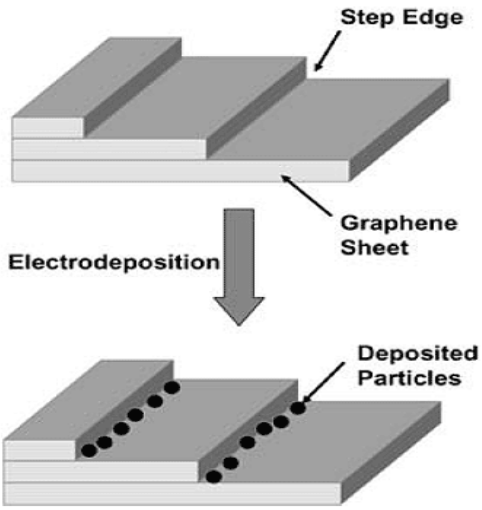

Figure 2.3 Step Edge Decoration Method to Grow Nanowires
(Reproduced with Permission, [3], [4])

Nanowire growth by electrochemical step edge decoration method has been traditionally accomplished on highly oriented pyrolytic graphite surfaces (figure 2.3) by applying three voltage pulses in succession: an oxidizing “activation” pulse of large amplitude, reducing “nucleation” pulse, and small amplitude reducing “growth” pulse.

The activation pulse potential helps to oxidize step edges on the graphite surface prior to deposition. The nanowire growth is primarily influenced by a time-independent deposition current, and consequently, the nanowire radius is proportional to the square root of the deposition time.

2.2 Bottom-Up Techniques

2.2.1 Self-Assembly Process

Self-assembly process is a viable route for manufacturing nanostructures. It is defined as the creation of material from its constituent components in a spontaneous natural manner, i.e. by an interaction between the components or by a specific rearrangement of them that proceeds naturally without any special external impetus. One of the well known approaches in the self-assembly is bio-templating which leverages the use of macromolecular scaffolds for hierarchical organization of molecules and materials. DNA and RNAs' serve as scaffolds (figure 2.4) for the assembly of materials and hierarchical organization of macromolecules such as metallic and semiconductor nanocrystals. Self-assembling nanostructures composed of DNA molecules offer great potential for bottom-up nanofabrication of materials and objects with ever smaller features.

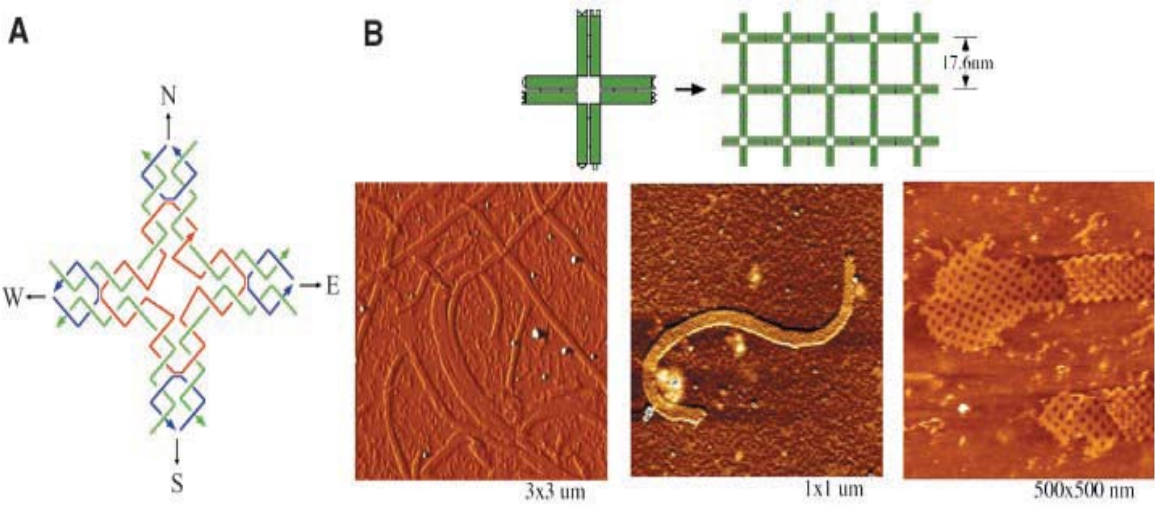

Figure 2.4 DNA Templated Self-Assembly of Conducting Nanowires
(Reproduced with Permission, [5])

Potential applications of DNA self-assembly and scaffolding include nanoelectronics, biosensors, and programmable/autonomous molecular machines. Recently, DNA has been used in the construction of periodically patterned structures [5], nanomechanical devices, and molecular computing systems. DNA has also been employed, with appropriate attachment chemistries, to direct the assembly of other functional molecules.

2.2.2 Solution Grown Method

In this method, molecular capping agents (which control the kinetics of crystal growth by allowing selective nucleation on certain facets) along with suitable seed materials are dispersed in a solvent (a suitable chemical compound comprising material of interest) medium. The solvent is then heated and pressurized until it becomes a supercritical fluid. When the concentration of the solvent exceeds solubility limit , the seed ejects the elemental compound in the solvent as nanowires. This forms the basis of solution grown nanowires. A variant of such a phenonemenon yet classified under the solution grown division is Langmuir-Blodgett ('LB') technique. LB method [6] uses an air-water interface to obtain a monolayer towards building the nanostructure. Amphiphilic molecules that have both polar (water-soluble) and non-polar (water-insoluble) moieties) having hydrophilic and hydrophobic chains dissolve into conventional organic solvents and disperse along the air-water interface. The monolayer with a thickness at atomic scale can form a variety of molecular-assembly structures such as gas, liquid, and solid like short and long-range orders through the control of surface pressure. Increase in the pressure enhances the magnitude of intermolecular interactions between the molecules. The chemical designs of hydrophilicity and hydrophobicity of the component molecules are important to obtain stable monolayer at the air-water interface. These monolayer add seamlessly to form the supra structure. Figure 2.5 schematically illustrates the "LB" technique.

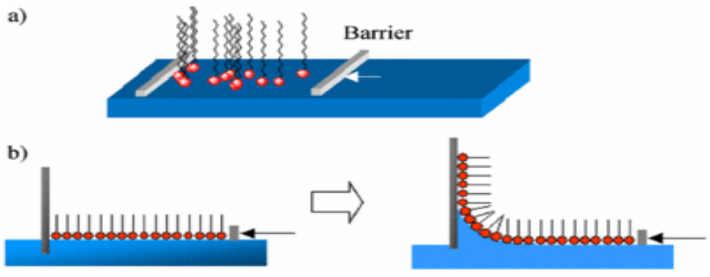

Figure 2.5 Schematic Illustrating the LB Method
(Reproduced with Permission, [6])

Solution grown techniques enable sequential assembly of homogenous nanostructures which are defect free. This approach requires very controlled process environments.

2.2.3 Carbothermal Reduction Technique

In this method, elevated temperatures are used which causes activated carbon to behave as a catalyst thus reducing metal oxides/nitrides/carbides to their corresponding oxide nanowires with release of carbon-monoxide. For example, carbon in mixture with an oxide produces sub-oxidic vapor species which reacts with C, O_2, N_2 or NH_3 to produce the desired nanowires. Thus, heating a mixture of Ga_2O_3 and carbon in N_2 or NH_3 produces GaN nanowires. Carbothermal reactions generally [7] involve the following steps:

Metal oxide +C = Metal sub-oxide + CO .....(2.1)

Metal sub-oxide + O2 = Metal Oxide Nanowires.....(2.2)

Metal sub-oxide + NH_3 = Metal nitride nanowires + CO + H_2.....(2.3)

Metal sub-oxide + N_2 = Metal nitride nanowires + CO .....(2.4)

Metal sub-oxide + C = Metal carbide nanowires + CO .....(2.5)

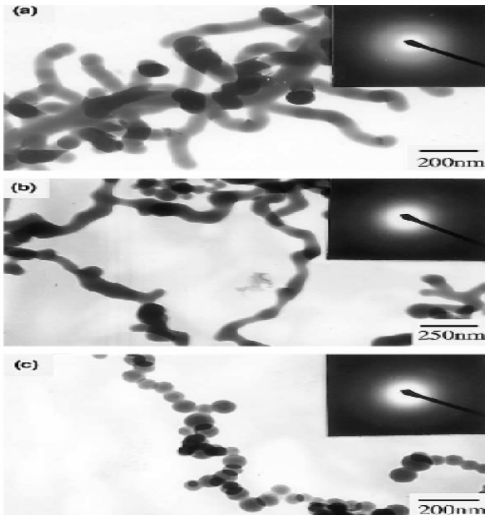

Figure 2.6 TEM Micrograph of Amorphous Silica Nanowires Indicating a Carbon Rich Tip (Reproduced with Permission, [7])

Figure 2.6 illustrates the growth of silica nanowires via carbothermal technique. A versatile method to produce a variety of nanowire of different materials; however requires careful control of temperature and proper disposal of the bye-product.

2.2.4 Oxide Assisted Growth Mechanism

Metal catalysts are not required for the synthesis of nanowires by this method. Stoichiometric or non- stoichiometric silicon oxide (Si_xO_y) in its vapor form induces nanowire growth. For example, the growth of Si nanowires [8] was promoted by SiO_2 derived from Si powder targets or SiO_2 thin films. The following equation best describes the growth process:

$$Si_x O \rightarrow Si_{x-1} + SiO(x > 1) \quad \text{.....(2.6)}$$

$$2SiO \rightarrow Si + SiO_2 \quad \text{.....(2.7)}$$

These decompositions result in the precipitation of Si nanoclusters, which act as the nuclei of the silicon nanowires covered by shells of silicon oxide.

2.2.5 Vapor Phase Techniques

2.2.5.1 Vapor Liquid Solid (VLS) Mechanism

Typically, nanowires or one-dimensional nanostructures can be fabricated by promoting the crystallization of solid state structures along one direction. This can be achieved either by the growth of intrinsically anisotropic crystal structure or the use of templates with one-dimensional morphologies directing the formation of one-dimensional nanostructures or the introduction of a liquid/solid interface thereby reducing the symmetry of a seed or by self-assembly of zero dimensional nanostructures.

The VLS method was first discovered by Wagner and Ellis in 1964 [9]. In the VLS method, the nanowire is grown in a desired orientation when a metal catalyst reacts with the 'nanowire material' in its gaseous phase at high temperatures. This method is based on the eutectic solidification of a metal and semiconductor. The catalyst also known as a second phase material is used to confine the crystal growth onto a specific orientation. The catalyst alloys itself with the growth material. This acts as a trap to the growth species which results in the precipitation at the growth surface in a single direction.

The VLS mechanism mainly depends on 4 steps:

(a) The mass transport of whisker growth species in the vapor phase to the vapor liquid phase,
(b) The chemical reaction on the vapor-liquid interface,
(c) The dissolution and diffusion through the liquid alloy phase, and
(d) The precipitation on the solid liquid interface

Common conditions for VLS growth are as follows:

(a) The catalyst must form a liquid solution with the crystalline material to be grown at the deposition temperature
(b) The distribution coefficient of the catalyst must be less than unity at the deposition temperature
(c) The equilibrium vapor pressure of the catalyst over the liquid droplet must be very small
(d) The catalyst or impurity must be inert chemically
(e) The interfacial energy (i.e.) the wetting characteristics plays a very important role. For a given volume of liquid droplet, a small wetting angle results in a large growth area, leading to a large diameter of nanowires
(f) For a compound nanowire growth, one of the constituents can serve as the catalyst, and
(g) For controlled unidirectional growth, the solid-liquid interface must be well defined crystallographically

The growth of nanowires from the vapor phase techniques requires that the starting reactants be a gas phase species. There are many techniques to prepare precursors into gas phases like laser ablation, CVD, MBE (Molecular Beam Epitaxy) and sputtering. A typical VLS growth is as depicted in the figure 2.7 wherein the growth species is evaporated in the presence of a catalyst which then diffuses into a liquid droplet. The liquids' surface has a large accommodation coefficient, so it is a preferred site for deposition. Saturated growth species in the droplet diffuse and precipitate at the interface between the substrate and liquid thus growing into a nanowire.

The VLS growth method is not restricted by the type of substrate materials and catalysts, thus enabling the nanowires to be either single crystalline, polycrystalline or amorphous.

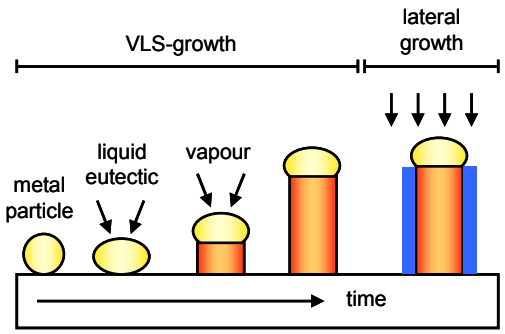

Figure 2.7 Schematic of the VLS Mechanism for Nanowire Growth

The high accommodation coefficient of the liquid surface is one of the most important and salient features of using it as a catalyst. Another crucial reason that for the liquid alloy can serve as a catalyst is that chemical reactions occur more readily on its surface than in the vapor phase. The liquid alloy phase reduces the activation energy at the liquid-solid interface and enhances the growth rate appreciably.

In general, a proper catalyst plays a key role in the VLS process. It forms a liquid droplet as a preferred site to adsorb the vapor pieces of the source materials. The desired one dimensional (1D) nanostructure precipitates, nucleates, and grows from the saturated liquid droplet. It has been well accepted that the diameters of the 1D nanostructure can be controlled by the catalyst droplets. Finally, the 1D nanostructure grown by the VLS process is typically capped by catalyst nanoparticles, which are remarkable morphological features of the mechanism. The selected catalysts in the VLS process should meet two demands. First, the catalyst should form the liquid eutectic alloy with a 1D nanostructure material under the growth temperature. Second, the catalyst should be more stable than the components of the desired 1D nanostructure. This sustains the continuous growth as long as the vapor species are available. The following sub-sections details about the VLS kinetics, minimum radius criterion, orientation, radial and axial VLS growth and self-catalytic VLS mechanism.

They are as follows:-

(a) VLS Kinetics

Typically a catalytic agent is coated onto a growth substrate and is placed in a vacuum furnace of high temperature. Vapor atoms of the nanowire material are passed through it. The lowest temperature and pressure are chosen such that they cause the catalyst to form alloyed eutectic phase seeds with the lowest concentration of the growth species (GS). This causes the tip of the seed to be semi-molten. The semi-molten structure of the tip has a soft lattice and loose interatomic configurations to allow adsorption of the GS vapor

If there is a lateral temperature gradient, or a sudden change of temperature, it leads to random breakup of the catalyst droplets. Also if there is an oversupply of the GS, it leads to oscillation of surface energies which enables multiple nucleations. Lastly, the gas of the GS can cause hydrodynamic stress on the droplet thus causing droplet breakup. The temperature and pressure are very crucial for the VLS mechanism to succeed. The growth of the nanowires will proceed only when the concentration of the GS is above the equilibrium solubility. Although the evaporation of the catalyst does not change the composition of the saturated liquid composition, it reduces the total volume of the liquid droplet. Unless more catalyst is supplied, the volume of the liquid droplet reduces and growth will stop when all the catalyst is evaporated.

(b) Minimum Radius Criterion in VLS Mechanism

The size of the nanowire determines its physical properties. The diameter is directly related to the size of the liquid droplet which in turn depends on the size of the nanocluster. Narrow wires are realized through monodispersed metal clusters. The clusters can be preformed using many techniques. A very popular method is the thin-film approach. Generally a thin film of gold is deposited as the solvent/initiator for the nanowire growth. Upon heating, these gold thin films will self-aggregate into a high density of Au clusters. Therefore diameter of the wire depends on the thickness of the catalyst film deposited. However there is a minimum critical radius below which the nanowire growth is impossible. The r_{min} [10] is given by:-

$$r_{\min} = 2\alpha V_L / RT \ln \sigma \quad \text{.....(2.8)}$$

Where,

σ – Liquid-Vapor Interface Energy

V_L – Molar Volume of a Droplet

α – Sticking Coefficient

(c) Orientation Dependence in VLS Mechanism

The orientation of the nanowires depends on the substrate texture and the diameter of wire [11]. Moreover, it also depends on the nanowire composition as materials prefer to orient in a direction minimizing their enthalpy of formation.

(d) Radial and Axial Growth

Radial and axial growth can be made possible by changing the reactant species in the middle of the synthesis. The vapor decomposition adsorption would still continue at the surface of the liquid catalyst. Crystalline growth of the new material with the width being determined by the depletion of the precious material and thermodynamic considerations would also continue. If the new species does not decompose at the catalysts' surface but at the surface of the previous material, then a shell consisting of the new material will grow over the original nanowires surface. To control this one needs to control the interfacial kinetics. A diagram illustrating it is as shown in figure 2.8 [12].

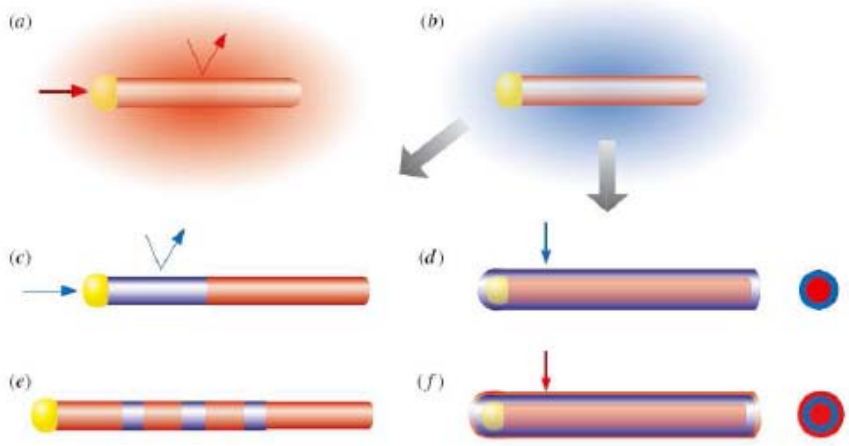

Figure 2.8 Schematic of the Radial and Axial VLS Growth
(Reproduced with Permission, [12])

(e) Self catalytic VLS Mechanism

When nanowires are made up of more than one type of element with complex stoichiometries, one of these elements must behave as a catalyst. Such growth techniques are called self catalytic VLS techniques. An example would be GaN nanowires [13].

The decomposition of GaN solid leads to the formation of Ga liquid nanoparticles. The vapor species would comprise of atomic nitrogen and diatomic or polymeric GaN which redissolves into the liquid Ga nanoparticles and initiates VLS growth. The major advantage of self catalytic VLS growth is that it can not be contaminated by unwanted metals unlike VLS growth methods.

2.2.5.2 Solid Liquid Solid (SLS) Mechanism

In this method, precursors are injected (solid) along with metal catalyst (solid) into a hot solvent (liquid) in free air. The solvent is quenched simultaneously forming nanorods. The characteristics of the nanowire are similar to that of VLS grown except for the wide tunablility in achieving the desired orientation and morphology of the wires.

2.2.5.3 Vapor Solid (VS) Mechanism

The fundamental concept behind synthesis of nanowire is to minimize the surface energy as it grows. Here the one dimensional structure is formed in the absence of a catalyst. The gas phase precursors directly react with the solid substrate to form the wires. It is easily differentiated from VLS by the absence of metal particle at the tip of the nanowire. The characteristics of these wires are very similar to that of the VLS growth.

2.2.5.4 Comparison Between VLS and VS Mechanisms

The VS method does away with the catalyst. The nanowire is grown from the gas phase directly to the solid phase through reverse sublimation. VS methods typically need a defect induced growth mechanism. Here, one dimensional growth is attained by the preferential reaction or binding of the gas phase along specific crystal facets. Screw dislocations seem to have higher accommodation coefficients compared to other defects thus allowing enhanced reactivity and growth. A major limitation of VLS growth is that one cannot synthesize metal nanowires due to the metal component in the catalyst.

2.3 Silica Nanowires: A Review of Growth Investigations

Silica nanowires have been synthesized using the discussed growth methodologies. The vapor phase approach has been traditionally used for high-density growth or application requiring mass manufacturing. A comprehensive review on the synthesis methodologies of silica nanowires has been presented in appendix section.

Figure 2.9 and 2.10 gives a brief review on the various growth techniques adopted and distinct morphologies of silica nanowires respectively. A comprehensive literature growth on silica nanowires is listed in table A.1 in appendix A [14-23].

Substrate	Catalyst Preparation	Growth Conditions (C, min ,Ambient)		Geometry Dia, Length (nm, µm)		Mechanism	Reference [2-11]
Si	NiO Powder	1000 - 1100 50-100	NH_3	50-100	mm	Solid-Liquid Solid	Park, B, Surf.Rev.Lett 2003
Colloidal Particles	TEOS, Ethanol, HCl, H_2O	80 30		1000	-	Solution Grown	S-S Choi J.Mat.Sci Lett 2003
Silica	Si/Si Powder	1400 12	N_2	80	100	Vapor Solid	Z.L.Wang, Adv Mat 2000
Pellets	SiO_2, $FeNO_3.9H_2O$, Active C Ball Mill	1350 180	Ar	60-110	>100 µm	VLS + Carbothermal	X.C. Wu Che.Phy.Lett 2001
Si	Sn + SiO	1320 420	Ar/H_2	230	mm	VLS + OAG	H.Wang Angew.Chet (2005)

Figure 2.9 Review on the Various Techniques in Synthesizing Silica Nanowires

Substrate	Catalyst Preparation	Growth Conditions (C, min ,Ambient)			Geometry Dia, Length (nm, μm)		Morphology	Reference
Glass, Si,Al_2O_3	Spu -Au, 15-90nm	350-1000		Ar	72	-	Spring	Wang L Nanotech. 2006
		30						
Si (111)	Ga, Ni Power $Ni(NO_3)_2.H_2O$	950		Ar/NH_3	30	20	Jelly Fish, Core-Shell	Cai, X.M. JAP 2005
		30						
Si	Ga Molten	700-950		NH_3	50	>30	Self-assembled Cone	Luo, S Small 2006
		10-60						
Silica	Si, C and Co	1500	60	Ar	20-120	10-250	Flower	Zhu,Y.Q J.Mat.Chem 1998
Alumina	Si Powder, SiO_2, PbO, C	1200		Ar/O_2	710	-	Various Morphology	J.Zhang Jnl.Cryst.Growth, 2001
		90						

Figure 2.10 Distinct Morphologies of Silica Nanowires via VLS Mechanism

Reviewing the growth methodologies, there is a lack of systematic investigation on the bottom-up growth of silica nanowires on Si. The precise mechanism by which silica nanowires grow remains uncertain and the dominant mechanism likely depends on the precise experimental conditions employed for their synthesis.

2.4 Summary

In this chapter, the nanowire growth methodologies have been reviewed. In particular, the VLS mechanism has been discussed in detail. Then, the past literature on silica nanowire growth has been highlighted. The next chapter details on the experimental results and conclusion of the various research activities performed.

.

2.5 References

[1] http://mrsec.umd.edu/images/Seed_TemplateSynthesis.jpg

[2] D. Bera, S.C. Kuiry, and S. Seal, "Synthesis of Nanostructured Materials Using Template-Assisted Electrodeposition", JOM 56 (2004), 49

[3] M.P. Zach, J.T. Newberg, L. Sierra, J.C. Hemminger, and R.M. Penner," Chemical Vapor Deposition of Silica Micro- and Nanoribbons Using Step-Edge Localized Water", J. Phys. Chem. B 107 (2003), 5373

[4] E. C. Walter, B. J. Murray, F. Favier, G. Kaltenpoth, M. Grunze, and R. M. Penner, "Noble and Coinage Metal Nanowires by Electrochemical Step Edge Decoration", J. Phys. Chem. B 106 (2002), 11407

[5] H.Yan, S-H.Park, G.Finkelstein, J.H. Reif, and T.H. LaBean, "DNA-Templated Self-Assembly of Protein Arrays and Highly Conductive Nanowires", Science 301 (2003), 1882

[6] A.Ullman, "An Introduction to Ultra-Thin Organic Thin Films: From Langmuir Blodgett – Self Assembly, Academic Press (1991)

[7] X.C Wu, W.H.Song, K.Y.Wang, T.HU, B.Zhao, Y.P.Sun and J.J.Du, "Preparation and Photoluminescence Properties of Amorphous Silica Nanowires", Chemical Physics Letters 336 (2000), 53

[8] C.N.R. Rao, F.L.Deepak, G.Gundiah and A.Govindaraj, "Inorganic Nanowires", Progress in Solid State Chemistry 31 (2003), 5

[9] R.S.Wagner and W.C.Ellis, "Vapor Liquid Solid Mechanism of Singe Crystalline Growth", Appl.Phys.Lett 4 (1964), 89

[10] T.Y.Tan, N.Li and U.Gosele, "Is there a thermodynamic size limit of nanowires grown by the vapor liquid process?", Appl.Phys.Lett 8 (2003), 1199

[11] C.X.Wang, M.Hirano, and H.Hosono, "Origin of Diameter-Dependent Growth Direction of Silicon Nanowires", Nano Letter 6 (2006), 1552

[12]L.J.Lauhon, M.S.Gudiksen, and C.M.Lieber, "Semiconductor Heterostructures", Phil Trans.Soc.:A 362 (2004), 1247

[13] Y.Q.Chen, J.Jiang, B.Wang, and J.G.Hou, "Synthesis of tin-doped indium oxide nanowires by self-catalytic VLS growth", Nanotechnology 37 (2004), 3319

[14] B.T.Park and K.Yong, "Characterization of Silicon Oxide Nanowires Directly Grown From NiO/Si", Surface Review and Letters 11 (2004), 179

[15] S-S. Choi, S, G.Lee, S.Soon, S.H.Kim, and Y. L.Joo, "Silica nanofibers from electrospinning/sol-gel process", Journal of Materials Science Letters 22 (2003), 891

[16] Z.L.Wang, R. P. Gao, James L. Gole, and John D. Stout, “Silica Nanotubes and Nanofiber Arrays”, Adv. Mater. 12 (2000), 24
[17] X.C. Wu, W.H. Song, K.Y. Wang, T. Hu, B. Zhao, Y.P. Sun and J.J. Du, “Preparation and photoluminescence properties of amorphous silica nanowires”, Chemical Physics Letters 336 (2001), 53
[18] H.Wang, X. Zhang, X.Meng, S.Zhou, S.Wu, W.Shi, and S. Lee, “Bulk Preparation of Si-SiOx Hierarchical Structures: High-Density Radially Oriented Amorphous Silica Nanowires on a Single-Crystal Silicon Nanocore”, Angew.Chem.Int 117 (2005), 7094
[19] L.Wang, D. Major, P Paga, D Zhang, M G Norton and D N McIlroy, “High yield synthesis and lithography of silica-based nanospring mats”, Nanotechnology 17 (2006), 298
[20] X. M. Cai, A. B. Djurišić, and M. H. Xie, “Growth of SiOx nanowire bunches cocatalyzed with Ga and Ni”, Journal of Applied Physics 98 (2005), 074313
[21] S.Luo, W.Zhou, W.Chu, J.Shen, Z. Zhang, L.Liu, D. Liu, Yanjuan Xiang, Wenjun Ma, and Sishen Xie, “Batchwise Growth of Silica Cone Patterns via Self-Assembly of Aligned Nanowires”, Small 3 (2007), 444
[22] Y.Q. Zhu, N. Grobert, H.Terrones, J.P. Hare, H.W. Kroto, W.K.Hsu, M.Terrones and David R. M. Walton, “3D Silicon oxide nanostructures: from nanoflowers to radiolarian”, J. Mater. Chem 8 (1998), 1859
[23] J.Zhang, F.Jiang, Y.Yang, and J. Li, “Molten Pb as a catalyst for large scale growth of highly aligned silicon oxide nanowires”, Journal of Crystal Growth 307 (2007), 76

Chapter 3

Experimental Methods and Techniques

This chapter gives an overview of the various experimental techniques used in this research to study and characterize the selective growth of silica nanowires. The first part of this chapter discusses the theoretical aspects of ion beam based modification of materials. Further, ion implantation (a subset of the ion beam methods) technique used for nanowire catalysis is discussed. This section is immediately followed by a brief discussion on the microscopic tools and techniques to observe the structure and morphology of the nanowires. The second part of the chapter discusses the basic principles of the spectroscopic characterization techniques reported in this dissertation.

3.1 Ion Beam Based Modification of Materials

An ion beam is defined as a point in 3-dimesnional space, of a certain kinetic energy, charge state and molecular weight. The beam might be continuous or pulsed depending on the requirement of the application. A beam can be extracted from an ion source followed by the selection of a particular molecular species and charge state by magnetic analysis. Further, acceleration of the selected species at the desired energy defines the location (depth) of the ions within the substrate/target. The flux of the species moves in a planned trajectory towards the target and is highly directional. A beam can be tailored to have multiple species with multiple energies and charge states. The use of ion beams for materials modification can be dated back to the 1950s [1] where it was first studied to densify and reduce the bandgap of semiconductors.

At present, many applications of ion beam have been engineered. Ion beam can be used to deposit thin films, expose fresh interfaces by removal of surface layers through high energy bombardment (sputtering), modify the phases of interfaces, dope trace elements into structures, impart specific chemical functionalities to a surface, and alter material properties. In general, ion induced processes enable interfaces with specific wettability, hardness, wear resistance, optical parameters, electronic properties and biocompatability.

Current microelectronics/CMOS manufacturing industries have employed ion induced process such as reactive ion etching, sub-100 nm photolithography and doping of semiconductors utilizing the different energy of the ions. A specific terminology has arisen to define approximate ion energy ranges: ion kinetic energies < 1 eV are known as thermal, 1–500 eV are hyperthermal, 0.5–10 keV are low energy, 10– 500 keV are medium energy and > 0.5 MeV are high energy. Figure 3.1 [2] schematically illustrates the ion beam related surface processes for varying ion kinetic energies.

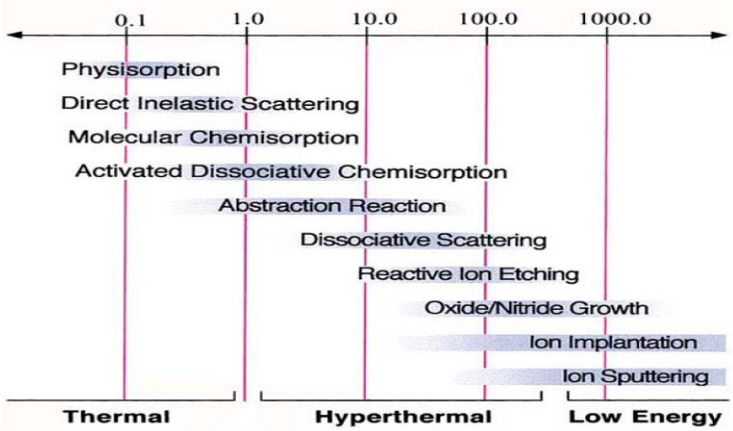

Figure 3.1 Fundamental Molecule/Surface Processes
(Reproduced with Permission, [2])

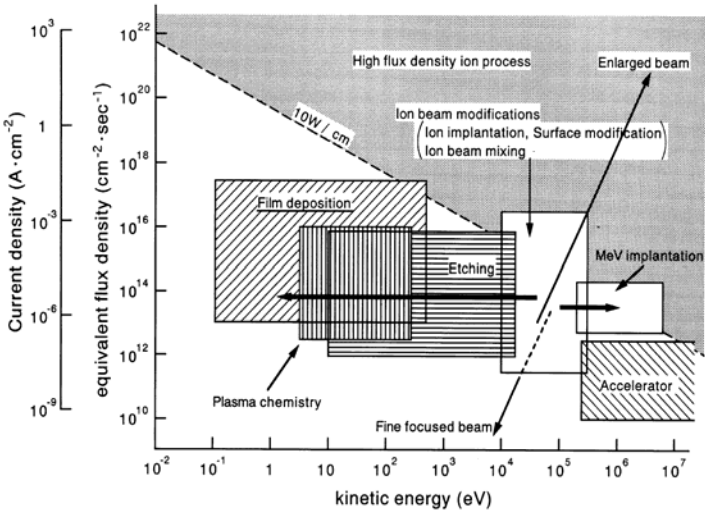

Figure 3.2 Ion Beam Processes as a Function of Kinetic Energy and Flux Density
(Reproduced with Permission, [3])

Further, figure 3.2 [3] shows a graphical plot of the ion beam processes as a function of equivalent flux density of the ions. As the ion energy increases into the medium and high energy range, the ion–surface interaction moves from a nuclear to primarily electronic in nature. A variety of charge transfer processes occur for ion–surface collisions across the full range of incident ion energies making it viable for many semiconductor applications. Among the ion beam processes, ion implantation has been used in this research for metal seeding induced nanowire growth.

3.1.1 Ion Implantation

Ion implantation is a low-temperature technique for the introduction of impurities (dopants) into semiconductors, and is preferred over diffusion. It is a process of introducing energetic and charged particles into a substrate. Implantation of ions into a target may alter the physical or chemical properties of the host via damage induced by the energy loss of the incident ions. In this surface modification technique, ions are extracted and accelerated towards the target. Before penetrating the host, the charged ions are separated according their mass to charge ratio. Then the desired species is directed at the target. The foreign atoms enter the crystal lattice, collide with the host atoms, lose energy and finally come to rest at some depth within the substrate. The average penetration depth is determined by the species, substrate material and the initial energy of the ions. This depth has some distribution as the collisions with the target atoms are random.

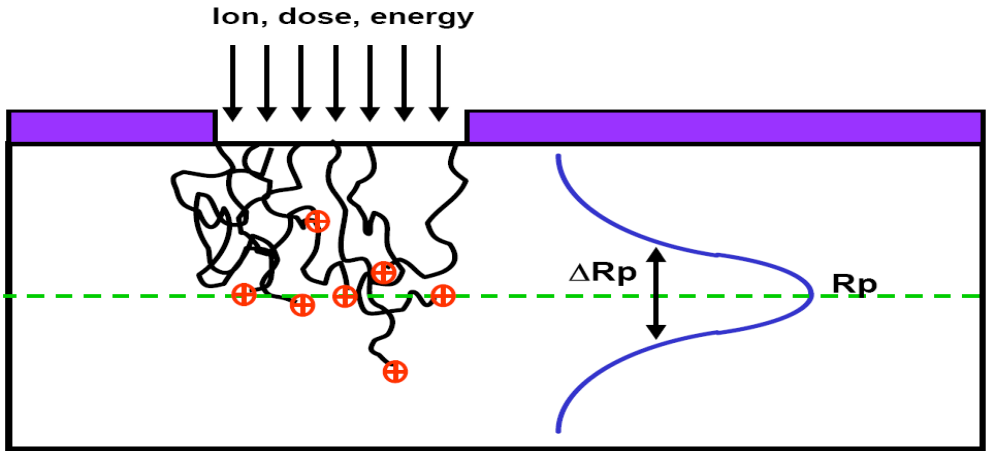

Figure 3.3 Random Interactions with Target Atoms in the Ion Implant Process (Reproduced with Permission, [4])

As each ion penetrates the target, it undergoes a series of collisions with the host atoms until it finally stops at some depth. The ion trajectories are random and can be predicted employing statistical means. The average total path length is called the range "R" which includes both lateral and vertical motions. Estimated depth of the implanted ions is referred to as the projected range Rp. Figure 3.3 [4] schematically illustrates the range and the projected range concept. The distribution of the implanted ions about the depth can be approximated as a Gaussian distribution with a standard deviation (ΔRp). The ion concentration n(x) at depth "x" can be formulated as:

$$n(x) = n_0 \exp(-(x - Rp)^2 / 2\sigma p^2) \quad \text{.....(3.1)}$$

Where,

n_0 – Peak Concentration,

σp – Standard Deviation

If the total implanted dose is denoted as "ψ", then the peak concentration is given by:

$$n_0 = 0.4\ \psi / \sigma p \quad \text{.....(3.2)}$$

Implantation energies range from few keVs to several MeV, resulting in the implanted depths from less than 10 nm to tens of μm. As mentioned in earlier sections, the ion dose (concentration) varies from 10^{11} to 10^{22} ions/cm^2 for implantation process. A critical parameter in the choice of ion species and the target is the stopping power.

3.1.1.1 Stopping Power

Energetic ions moving through a solid medium lose energy through ionization of electrons and elastic collisions with target nuclei. These events are considered as independent processes, so that the linear rate of energy loss is given by the sum (figure 3.4, [5]) of two contributions:

$$dE / dx = S_n(E) + S_e(E) \quad \text{.....(3.3)}$$

Where,

dE/dx – Rate of Energy Loss for the amount of distance traveled

$S_n(E)$ – Energy Loss due to Nuclear Stopping

$S_e(E)$ – Energy Loss due to Electronic Stopping

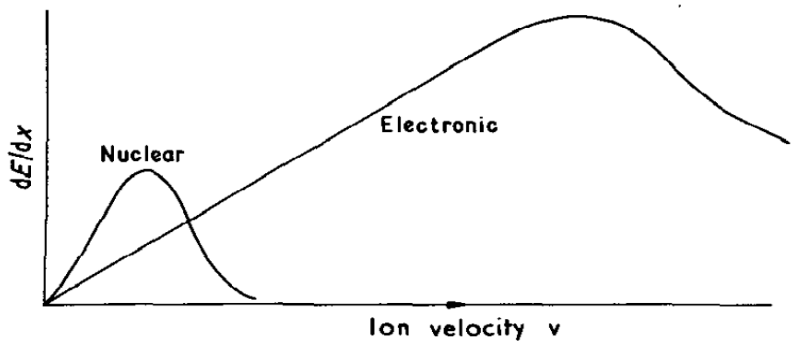

Figure 3.4 Nuclear (or Elastic) and Electronic (or Inelastic) Contributions Energy Rate:, dE/dx, as a Function of the Velocity for an Ion Moving in a Solid (Reproduced with Permission, [5])

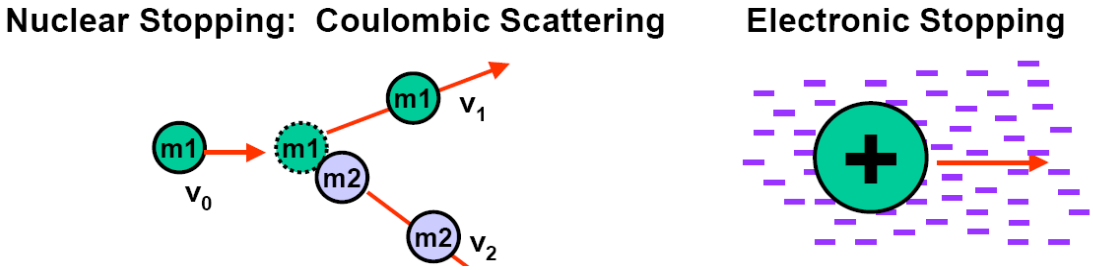

Figure 3.5 Energy Loss of the Ion Species Entering a Target: Nuclear and Electronic Stopping (Reproduced with Permission, [6])

3.1.1.2 Nuclear Stopping

Energy loss per distance traveled depending on the nuclear charge and atomic masses (figure 3.4, [6]) of both incident ion and target atom. Energy loss due to interaction with atomic nuclei is basically a decreasing function of energy. At high kinetic energy (ion velocity), there is a very short interaction time for any absorption of energy by target atoms. The expression for nuclear stopping is given by:

$$S_n(E) = (dE/dx)_n \quad \text{.....(3.4)}$$

$$dE/dx_n = S_n = (N\pi^2 e^2 a Z_1 Z_2 M_1 M_2)/2(M_1 + M_2) \quad \text{.....(3.5)}$$

Where,

N – Atomic Density,

a– 1.4×10^{-2} nm,

1, 2 refers to the ion,

Z – Atomic Number,

M – Mass Number

3.1.1.3 Electronic Stopping

Ion interacts with the electron in the target material and the electrons offers resistance to ion flow similar to a viscous drag force that is proportional to the ion velocity. A simplified expression for the stopping power is given by:

$$S_e(E) = (dE/dx)_e = k_e E^{0.5} \quad \text{.....(3.6)}$$

Where,

k_e – Constant = $(10^7 \text{ eV})^{0.5}$/cm

E – Incident Energy

Electronic stopping dominates in the case light ions traveling with high energies where as nuclear stopping is dominated by heavy ions traveling with lower energies. Both the stopping phenonemenon results in the damage of the host lattice. An impurity atom finding itself next to such a defect position may hop into it and sufficient thermal activation can produce of avalanche of damage. These displaced atoms may possess large fractions of the incident energy, and they in turn cause cascades of secondary displacements of nearby atoms to form a chain of disorder along the ion path. When the displaced atoms per unit volume approach the atomic density of the semiconductor, the material becomes amorphous. Detailed information on the various concepts of the implantation process can be found from textbooks authored by Williams and Poate [7].

3.1.1.4 Ion Source: MEVVA Type

The MEVVA (Metal Vapor Vacuum Arc) ion source is a high current device which can readily produce ion beam currents of several hundred milliamperes on target. Extraction potential up to 50 kV is used to implant metallic elements. Ion beams of most metallic elements either individually or in combination can be generated with a MEVVA source.

In the MEVVA source (figure 3.6), an arc is established between the cathode (the metal to be implanted) and the anode. A basic characteristic of this type of discharge is the formation of "cathode spots", which are minute regions of intense current flux (many mA/cm^2 over a spot diameter of the order of μm) on the cathode surface, at which the desired material is vaporized and ionized. Thus the cathode spots act as small regions of plasma generation from the solid surface. An external bias sustains the main arc. Plasma is generated between the cathode and anode. When high extraction voltage is applied at the extraction electrode, ions in the plasma are attracted by the high electric field and fly out the extraction area creating a high current ion beam.

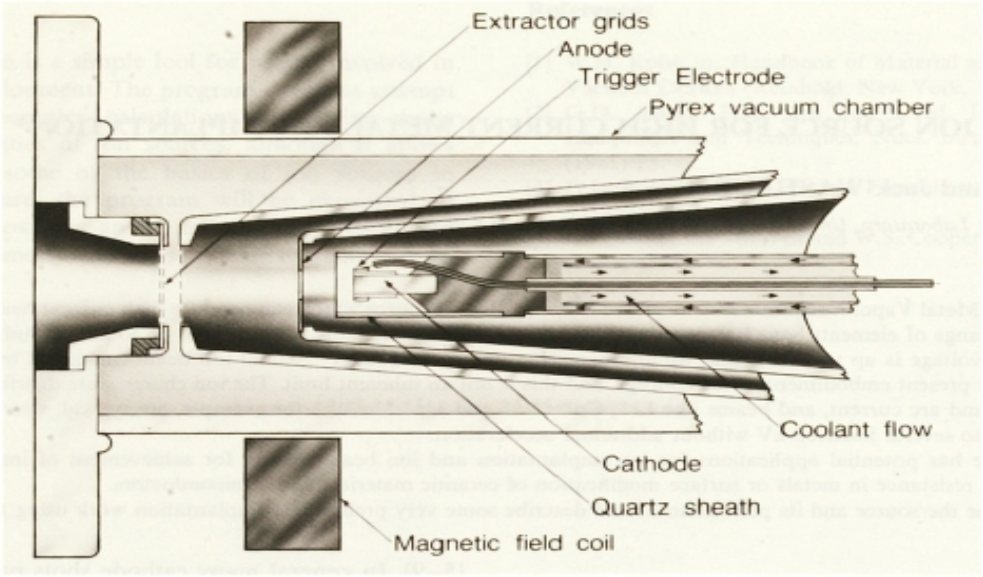

Figure 3.6 Schematic Showing a Cross Sectional View of the MEVVA II Ion Source (Reproduced with Permission, [8])

MEVVA [8] based implantations are very economical as there is no need for the same level of cleanliness and state-of-the-art equipment. This method has a high throughput of non-mass analyzed metal ions, and therefore, it has more potential for industrial non-electronic applications. The inherent limitation of the MEVVA source is the production of ion beam with multiple charge states (for example Au^+, Au^{2+} and Au^{3+}). Alternatively, the beam produced by a SNICS (Source of Negative Ions by Cs Sputtering) source is devoid of multiple charge states obtained from mass and charge filtered by an energy analyzing magnet.

3.1.1.5 SNICS Source

Negative ions are formed by the attachment of an electron to an atom or a molecule. The process is exothermic, while the positive ion formation is an endothermic reaction. The binding energy of a negative ion is called electron affinity.

A stable negative ion exists if the electron affinity is a positive quantity. Several processes can lead to the formation of negative ions. Electron impact in a dense gas, charge exchange with neutral atoms or molecules, charge exchange with surface atoms during absorption/desorption. If an ion beam passes through a vapor of atoms which have low ionization potentials, a substantial fraction of the incident ions can capture electrons to form negative ions. This forms the basis of negative ion generation in the SNICS source.

In the SNICS source type [9], the species to be ionized is obtained by sputtering a solid target containing the desired material with energetic ions that can be introduced into the chamber. The Cs^+ ions sputter away the cathode material. Cesium is contained into a reservoir which is heated up to 170^0 C to produce Cs vapors which are introduced into the source through a small tube. An ionizer, heated up to 1200^0 C through a 22 A current flow is used to produce Cs^+ ions which are accelerated by 7 kV voltage towards the cathode and hence produce the sputtering of the cathode material (Cathodes are usually made by small copper cylinders with a central hole which is filled with the material to be sputtered or implanted). Negative ions sputtered from the cathode are extracted by a 20 kV voltage and later further accelerated by 0-80 kV potential with a pre-acceleration stage prior to the injection into the accelerating tube.

The beam of negative ions is focused by an Einzel lens and accelerated by a source bias into a 90^0 analyzer magnet, with a path radius, R, for mass filtering. The magnetic field (B) is set such that, the magnetic force acting on the accelerated ions is set equal to the centrifugal force on the desired ions as they are deflected through a radius (R). The strength of the magnetic field (B) required for the selection of the desired mass (m) will be:

$$B = \frac{1}{R}\sqrt{\frac{2mV_i}{qZ}} \quad \text{.....(3.7)}$$

Where, V_i is the potential difference through which the ions are accelerated, q is the electronic charge and Z is the ion charge state.

Finally, the beam is electrostatically scanned across the target in the *x, y* directions (raster scanned) until the required implant fluence (Q) is achieved. The implant fluence can be expressed as an integral over time (t):

$$Q = \frac{1}{qAZ}\int_0^t idt \quad \text{.....(3.8)}$$

Where, i is the beam current and A is the implanted area (determined by the tantalum aperture at the entrance of the target chamber). The photograph of the 175 kV high energy ion implanter is shown in figure 3.7.

Figure 3.7 Schematic of the High Energy Implanter at Australian National University, Canberra

3.1.1.6 Advantages of Ion Implantation

(a) Very precise control of the dose

(b) Independent control of impurity depth and dose

(c) Very fast (One 6" wafer can take as little as 6 seconds for a moderate dose)

(d) Complex profiles can be achieved by multi-energy implants.

(e) Wide Dynamic Range of Dose

(f) Wide selection of masking materials

3.1.1.7 Limitations of Ion Implantation

(a) Very deep and very shallow profiles are difficult

(b) Not all the damage can be corrected by annealing

(c) Typically has higher impurity content than does diffusion

(d) Often uses extremely toxic gas sources such as arsine (AsH_3), and phosphine (PH_3)

(e) Expensive

3.2 Characterization Techniques

The techniques used to observe and characterize the growth of silica nanowires on Si are broadly classified into:-

(a) Surface morphology analysis using scanning electron microscopy (SEM) in secondary (SE) and back scattering mode (BSE),

(b) Microstructural characterization using transmission electron microscopy (TEM),

(c) Compositional analysis using energy dispersive spectroscopy (EDS),

(d) Phase identification via X-ray Diffraction (XRD) and selected area diffraction patterns (SAED),

(e) Optical characterization using fluorescence and photoluminescence (PL) and

(f) Structural functionalities using Infra-red and Raman spectroscopy.

3.2.1 Scanning Electron Microscopy

An electron microscope is a type of microscope that uses electrons to illuminate the sample. Electron microscopes have much greater resolving power and can obtain higher magnifications than a light microscope. They can magnify specimens up to 2 million times, while the best light microscopes are limited to magnifications of 2000 times. Such a multi-fold enhancement in the resolution is due to the smaller wavelength of the electrons. For example, the wavelength of electron induced by a 10 kV machine would be around 0.0123 nm whereas the visible wavelength of light ranges from 400-700 nm. Before proceeding in detail, the interaction of electrons with the surface of the sample needs to be understood.

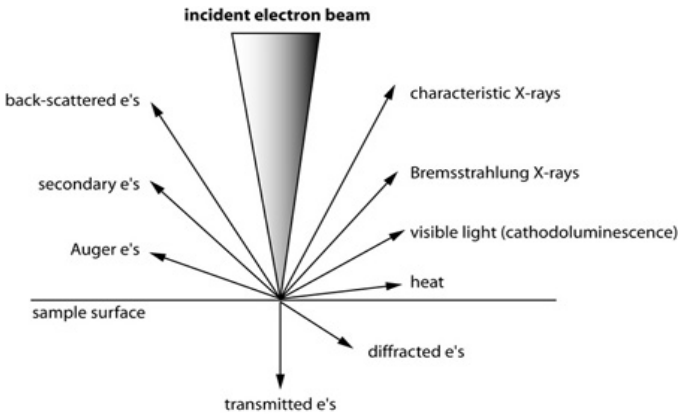

Figure 3.8 Interactions of Electrons with the Sample
[Courtesy: Geochemical Instrumentation and Analysis, Science Education Research Center, Carleton College]

When electrons bombard on to a surface, a number of interactions (figure 3.8) arises with the atoms of the target sample. Accelerated electrons can either pass through the sample without interaction, or undergo elastic scattering or inelastic scattering.

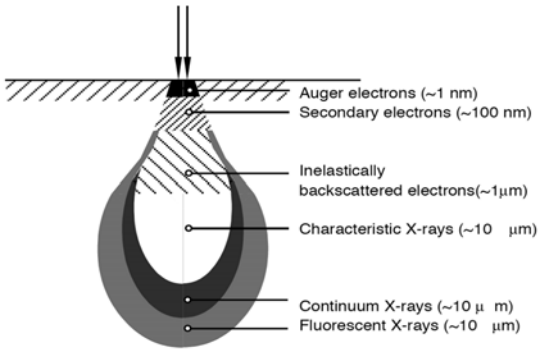

Figure 3.9 Electron Interactions with Specimen: Scattering Events as a Function of Depth
[Courtesy: Geochemical Instrumentation and Analysis, Science Education Research Center, Carleton College]

Typical signals include secondary electrons (SE), back scattered electrons (BSE), visible light, Auger electrons and characteristic X-rays arising from different depths (figure 3.9) in the sample.

Secondary emission is produced by inelastic interactions of high energy electrons with valence electrons of atoms in the specimen. After undergoing additional scattering events while traveling through the specimen, some of these ejected electrons emerge from the surface of the specimen. The secondary electrons emerge with energies less than 50 eV.

Further, larger atoms (with a greater atomic number, Z) have a higher probability of producing an elastic collision because of their greater cross-sectional area. Consequently, the number of backscattered electrons (from a higher depth) reaching the detector is proportional to the mean atomic number of the sample. Thus, a "brighter" BSE intensity correlates with greater average Z in the sample, and "dark" areas have lower average Z. BSE images are very helpful for obtaining high-resolution compositional maps of a sample thus enabling the differentiation of heavy and light elements/compounds and metal/dielectric nature of the sample. The solid state detectors for collecting the secondary and back scattered electrons are placed on the side and in line with the electron gun respectively. Along with BSE image, the elemental and chemical composition is verified using energy dispersive spectroscopy.

3.2.2 Energy Dispersive Spectroscopy

When a high energy electron beam hits the sample surface, an electron in the ground state can get excited to a higher energy level. Subsequently, an electron from an outer, higher-energy shell then fills the hole, and the difference in energy between the higher-energy shell and the lower energy shell is released in the form of an X-ray. As the energy of the X-rays is characteristic of the difference in energy between the two shells, and of the atomic structure of the element form which they were emitted, this allows the elemental composition of the specimen to be measured. In general, energy dispersive spectroscopy is abbreviated as EDS.

3.2.3 X-Ray Diffraction

Phase identification in addition to elemental composition of materials can be deduced by X-ray diffraction. X-rays primarily interact with electrons in atoms. When x-ray photons collide with electrons, some photons from the incident beam will be deflected away from the incident direction. Diffracted waves from different atoms can interfere with each other and the resultant intensity distribution is strongly modulated by this interaction.

If the atoms are arranged in a periodic fashion, as in crystals, the diffracted waves will consist of sharp interference maxima (peaks) with the same symmetry as in the distribution of atoms. This interference is constructive when the phase shift is a multiple of 2π. This condition can be expressed by Braggs' Law:

$$n\lambda = 2d\sin\theta \quad \text{.....(3.9)}$$

Where,

n – An integer by the order,

λ – Wavelength of the X-rays,

d – Spacing between the atomic lattice, and

θ – Angle between the incident ray and the scattering planes

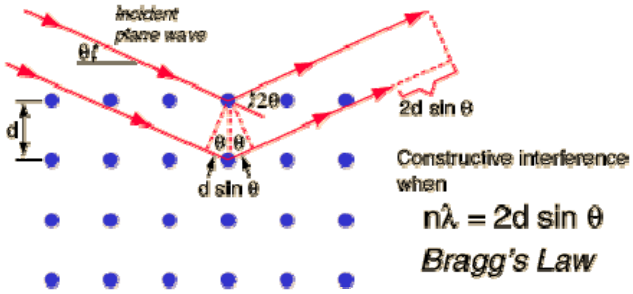

Figure 3.10 Schematic Showing the Principle of Braggs' Law

[Courtesy: Princeton University]

Measuring the diffraction pattern therefore allows us to deduce the distribution of atoms in a material. The analysis in the X-ray diffraction technique works on the basis of Braggs' Law (figure 3.10). Though X-ray diffraction allows identifying the phase a sample on a whole, intricate details such as the phase change at interfaces cannot be observed. In such cases, a TEM analysis has been preferred.

3.2.4 Transmission Electron Microscopy

Transmission electron microscopy (TEM) is a very high resolution imaging technique used to determine the structural details of materials at an atomic or molecular scale. This technique necessitates very thin sections of specimen to be observed as the detector captures the transmitted electrons unlike SEM principles. In TEM, a thin specimen is irradiated with an accelerated electron beam of uniform current density.

Electrons illuminate the specimen through a two or three stage condenser lens system. The focused image of the surface is magnified with a three or four stage lens system and viewed on a fluorescent screen. Materials/specimen for TEM inspection must be thin enough to transmit sufficient electrons for a clear projection on the phosphor screen or photographic film to give an interpretable image. Based on de Broglies' ideas of wave-particle duality, the electron momentum *p* is related to its wavelength through Plancks' constant. Thus,

$$\lambda = \frac{h}{p} \quad \text{.....(3.10)}$$

Since the electrons are accelerated in a TEM (typically above 100 kV), the relativistic effects can not be ignored; thus,

$$\lambda = \frac{h}{\sqrt{2m_o eV(1+\frac{eV}{2m_o c^2})}} \quad \text{.....(3.11)}$$

Where, "m_o" is the mass of an electron at rest, "eV" is the kinetic energy of an electron when accelerated through a potential difference "V", "h" is Plancks' constant and "c" is the speed of light in vacuum. For example, at an accelerating voltage of 200 kV, the relativistic wavelength of an electron is 0.0251 Å enabling a magnification order of a million.

The two basic operating modes of a TEM are the imaging and diffraction modes. The conical ray diagrams of the two modes are shown in figure 3.11. In the image mode the intermediate lens is focused on the image plane of the objective lens whereas in the diffraction mode the intermediate lens is focused on the back focal plane of the objective lens, forming the diffraction pattern of the sample. The objective aperture inserted in the back focal plane of the objective lens controls the contrast and resolution by selecting transmitted and/or diffracted electrons that contribute to the image.

The two imaging modes of the TEM are the bright field (BF) and dark field (DF) sections. A BF image is formed by transmitted electrons whereas a DF image is formed by diffracted electrons. Conventional TEM studies of crystalline materials often use the diffraction contrast mechanism (which is the variation of intensity of electron diffraction across the sample) to produce either of the images. BF and DF images are in general complementary in nature.

Features of the sample that are seen as dark in a BF image are seen as bright in a DF image, and vice versa. For the work presented in this thesis, the imaging mode was used to obtain information about the gold nanocluster shape and size.

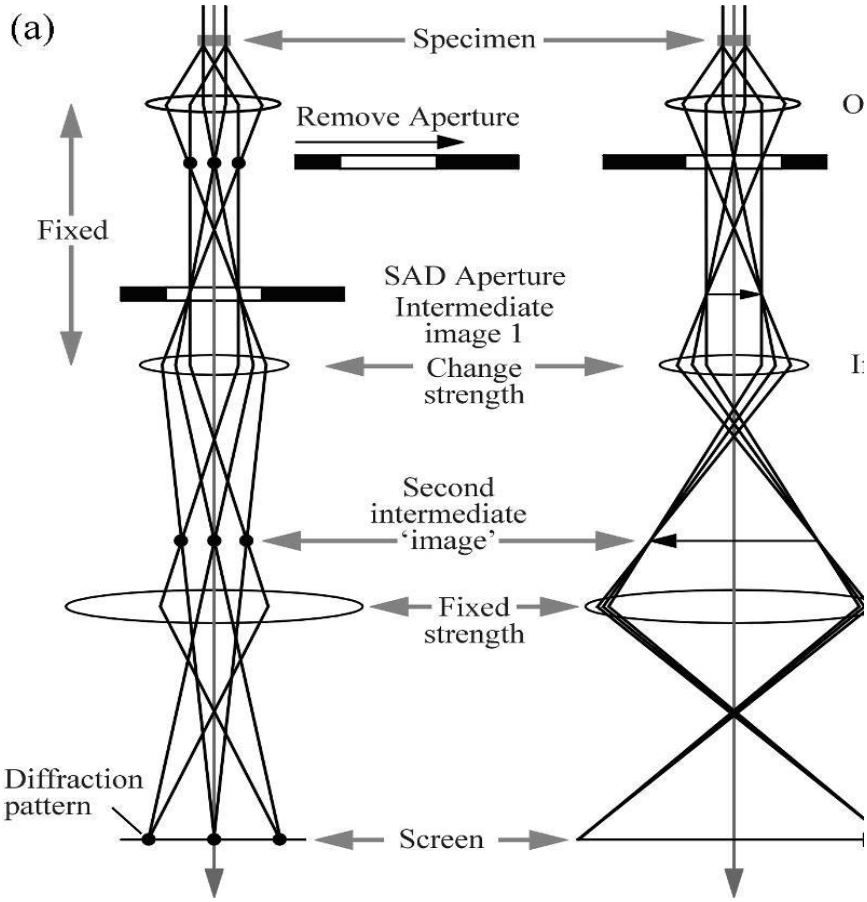

Figure 3.11 Conical Ray Diagrams of the Two Basic Modes of TEM Operation
a) Diffraction mode and b) Imaging mode
(Reproduced with Permission, [10])

In diffraction mode, a selected area aperture is often used to obtain a diffraction pattern from a selected area of the sample and to limit the intensity of the electrons reaching the viewing screen. This process is termed selected area diffraction (SAED). The diffraction patterns can be used to identify the diffracting material in much as the same way as X-ray diffraction.

The relation between the inter-planar spacing of a material and the electron diffraction pattern is given by:

$$Rd = \lambda L \quad \text{.....(3.12)}$$

Where, "R" is the distance from the primary beam (non-diffracted) to the diffraction ring, "λ" is the wavelengths of electrons, and "L" is the camera length. For the work reported in this thesis, the diffraction mode was used to identify the phase of the nanowires and observe the reminiscence of the catalyst, if any. For a more thorough explanation of the basic modes of TEM and their principles the reader is referred the to texts by Williams and Carter [10] .

3.2.5 Infra Red Spectroscopy

Infrared (IR) spectroscopy is one of the most common optical techniques used by organic and inorganic chemists. The IR absorbance spectrum is used to identify the chemical functionality in the sample as various structural moieties absorb different IR frequencies. IR spectroscopy is a unique and important tool for structural elucidation and compound identification. The theory of IR absorption is described in the next section.

3.2.5.1 Theory

Each atom has three degrees of freedom, corresponding to motions along any of the three cartesian coordinate axes (x, y, and z). A polyatomic molecule of "n" atoms has "3n" total degrees of freedom. However, 3 degrees of freedom are required to describe translation, the motion of the entire molecule through space. Additionally, 3 degrees of freedom correspond to rotation of the entire molecule. Therefore, the remaining "3n – 6" degrees of freedom are true, fundamental vibrations for nonlinear molecules. Alternatively, linear molecules possess "3n – 5" fundamental vibrational modes because only 2 degrees of freedom are sufficient to describe rotation. At temperatures above absolute zero, all the atoms in molecules are in continuous vibration with respect to each other. When the frequency of a specific vibration is equal to the frequency of the IR radiation directed on the molecule, the molecule absorbs the radiation.

Among the 3n – 6 or 3n – 5 fundamental vibrations, those that produce a net change in the dipole moment may result in an IR activity and those that give polarizability changes may give rise to Raman activity.

Naturally, some vibrations can be both IR and Raman active. The total number of observed absorption bands is generally different from the total number of fundamental vibrations. It is reduced because some modes are not IR active and a single frequency can cause more than one mode of motion to occur. Conversely, additional bands are generated by the following:-

(a) appearance of overtones (integral multiples of the fundamental absorption frequencies)
(b) combinations of fundamental frequencies
(c) differences of fundamental frequencies
(d) coupling interactions of two fundamental absorption frequencies, and
(e) coupling interactions between fundamental vibrations and overtones

A possible list of vibrations is illustrated in the schematic (figure 3.12) below. The two major types of molecular vibrations are referred to as the stretching and bending modes. Infrared radiation is absorbed and the associated energy is converted into these types of motions. The absorption involves discrete, quantized energy levels. However, the individual vibrational motion is usually accompanied by other rotational motions. These combinations lead to the absorption bands. At present, Fourier Transformed Infra Red spectroscopy has been preferred.

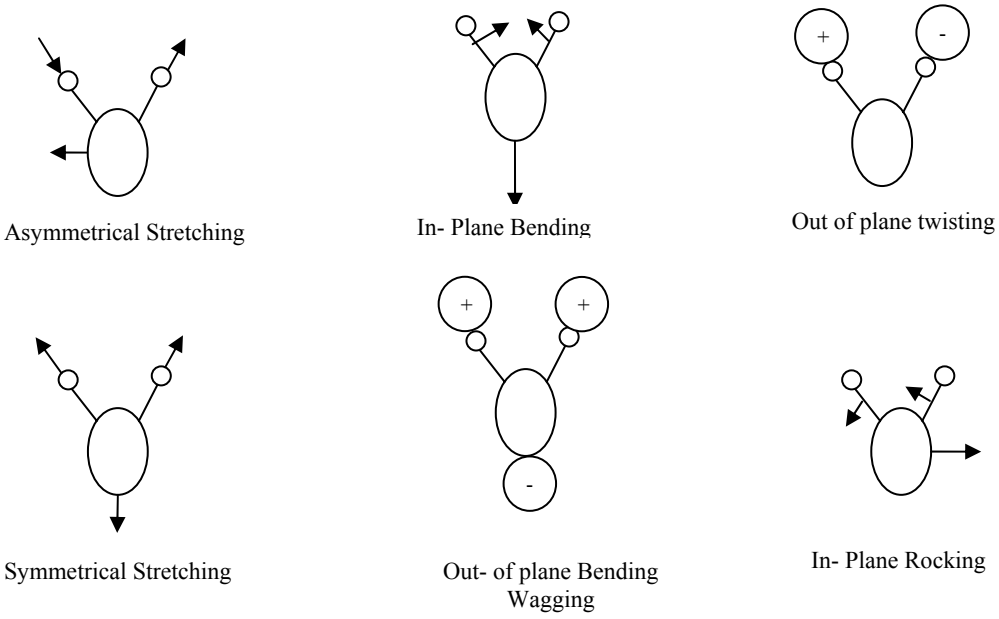

Figure 3.12 Possible Lists of Atomic Vibrations

3.2.5.2 Fourier Transform Infra Red Spectroscopy (FTIR)

Fourier transform spectrometers have recently replaced dispersive instruments for most applications due to their superior speed and sensitivity. They have greatly extended the capabilities of infrared spectroscopy and have been applied to many areas that are very difficult or nearly impossible to analyze by dispersive instruments.

Because instead of viewing each component frequency sequentially, as in a dispersive IR spectrometer, all frequencies are examined simultaneously in Fourier transform infrared (FTIR) spectroscopy.

In the current research, the molecular dipole moment induced infrared characteristics verifying the chemical affinity of these nanocomposites in the assay were obtained over a range of frequencies (400 to 3000 cm^{-1}) with a resolution of 0.4 cm^{-1}. The sample was inspected under the Perkin-Elmer FTIR spectrometer for the complementary infrared absorption using a sealed and desiccated optical module.

3.2.5.3 Applications of IR and FTIR Spectroscopy

(a) Determination of functional groups in organic materials
(b) Determination of the molecular composition of surfaces
(c) Identification of chromatographic effluents
(d) Quantitative determination of compounds in mixtures
(e) Determination of molecular orientation (polymers and solutions)
(f) Identification of reaction components and its kinetics
(g) Detection of molecular impurities or additives present in amounts of 1% and in some cases as low as 0.01%
(h) Analysis of formulations such as insecticides and copolymers

3.2.5.4 Limitations of IR Spectroscopy

(a) Availability of minimal elemental information
(b) Background solvent or solid matrix must be relatively transparent in the spectral region of interest
(c) Molecule must be active in the IR region
(d) When exposed to IR radiation, a minimum of one vibrational motion must alter the net dipole moment of the molecule in order for absorption to be observed

3.2.6 Raman Spectroscopy

Raman spectroscopy is a molecular vibration technique that depends on inelastic scattering of monochromatic light, usually from a laser (in the visible, near infrared, or near ultraviolet range) by atomic interactions.

The laser light interacts with phonons resulting in the energy of the laser photons being shifted up or down. Consequently, the shift in energy gives information about the phonon modes in the system. Wavelengths close to the laser line, due to elastic Rayleigh scattering, are filtered out while the rest of the collected light is dispersed onto a detector. Spontaneous Raman scattering is typically very weak and is difficult to resolve from the intense Rayleigh scattered laser light.

The Raman signature is observed when light impinges upon a molecule and interacts with the electron cloud of the bonds as the incident photon excites one of the electrons into a virtual state. If a molecule gets excited from the ground state to a virtual energy state, and then relaxes back into a vibrational excited state, it emanates Stokes Raman scattering. On the other hand, if the molecule was already in an elevated vibrational energy state, the Raman signature is then referred to as anti-Stokes Raman scattering. Following the conservation of energy and momentum,

$$E_{scattered} = E_{Source} \pm h\Omega \quad \text{.....(3.13)}$$

the energy of scattered event is given by eq 3.13 for Stokes (-) and Anti-Stokes (+) respectively, with "Ω" being the frequency of the particular phonon mode.

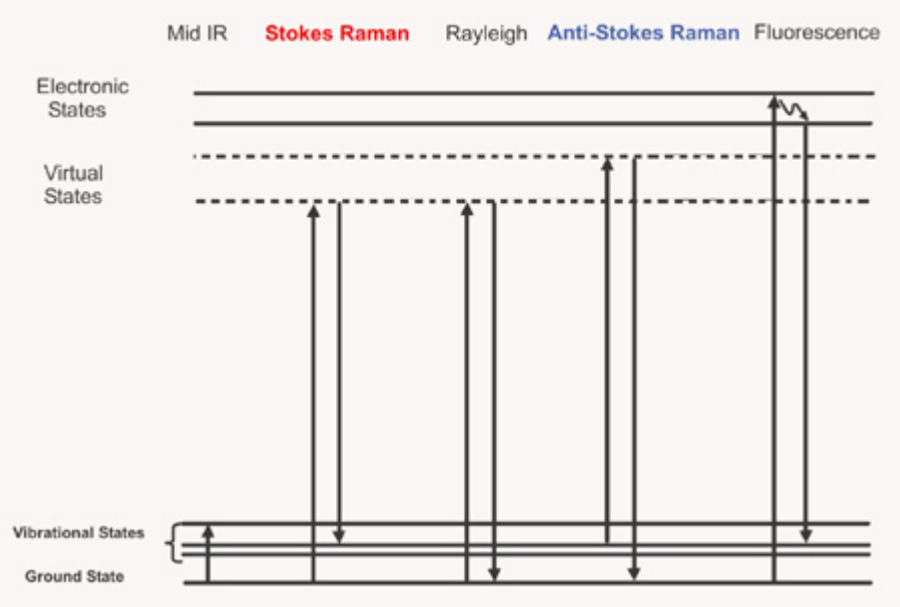

Figure 3.13 Jablonski Diagram of Energy States
[Courtesy: Jobin Vyon Raman Division]

Figure 3.13 shows the Jablonski diagram of energy levels indicating the elastic scattering of a molecule. The energy of the inelastically scattered light is measured with respect to the laser energy.

The amount of deformation the electron cloud undergoes with respect to the vibrational co-ordinate dictates the magnitude of the Raman effect. Thus, the degree of change in polarizability will determine the Raman scattering intensity, whereas the Raman shift is determined by the vibrational level that is involved. Raman scattering is a weak interaction, and typically less than one in a million of the incoming photons exchanges energy with the phonons in bulk materials. However, Raman scattering is a well established tool for materials characterization (structure, bonding and composition), through the measurement of vibrational properties.

Due to phonon confinement, the Raman spectra of nanoparticles and nanostructured materials are substantially different from the spectra of the corresponding bulk, and provide useful information relative to the size and the dynamical behavior of the building blocks.

In-situ measurements permit the investigation of phenomena such as cluster deposition, film growth, thermal and chemical stability of nanostructures. Further, the low energy region of Raman scattering is extremely sensitive to the mean nanoparticle diameter, to the width of the particle size distribution and to the particle-matrix interface conditions. The distinct peaks that emerge in the very low-frequency region of scattering are due to acoustic phonon modes. Such low frequency Raman peaks have been observed in several nanocomposite systems where dielectric, semiconductor or metallic particles were embedded into diverse solid matrices. The Raman effect is very weak, which leads to low sensitivity, making it difficult to measure low concentrations of a substance.

3.2.6.1 Raman Vs FTIR

Infrared (IR) and Raman spectroscopy are complementary techniques that provide information on molecular structure. Different chemical bonds absorb at various infrared wavelengths depending on the atoms connected, the surrounding molecules, and the type of vibrations of the atoms. On contrary, in Raman spectroscopy, the sample is radiated with monochromatic visible or UV light from a laser. This brings the vibrational energy levels in the molecule to a short-lived, high energy collision state, which returns to a lower energy state by emission of a photon. Normally the photon has a lower frequency than the laser light and the difference in frequency (given in reciprocal centimeters) between the frequency of the laser and that of the scattered photon is called the Raman shift. The Raman shift corresponds to the frequency of the fundamental IR absorbance band.

3.2.6.2 Surface Enhanced Raman Spectroscopy (SERS)

SERS is a very powerful, non-invasive, label free molecular probing technique based on unique vibrational spectroscopic signature (optical ‘fingerprinting’) capable of distinguishing almost any chemical and biologically relevant analytes. The weak Raman signals are enhanced in a SER configuration which depends on the substrate architecture. SER signal is based on a plasmonic phenomenon whereby specific molecules at or near a nanoscale roughed metal surface surrounded by a dielectric medium undergo a dramatic increase in the intensity via localized electromagnetic enhancement providing a structural ‘fingerprint’ of the biomolecule event under investigation. The electromagnetic enhancement, mainly lightning-rod effect, plays an essential role in the SERS of transition metals, and that the charge-transfer effect is also operative in some specific metal–molecule systems.

3.2.7 Photoluminescence

Photoluminescence (PL) is the spontaneous emission of light from a material under optical excitation. When light of sufficient energy is incident on a material, photons are absorbed and electronic excitations are created. Eventually, these excitations relax and the electrons return to the ground state. If radiative relaxation occurs; the emitted light is called PL. PL [11] depends on the nature of the optical excitation. The excitation energy selects the initial photoexcited state and governs the penetration depth of the incident light. Also, the choice of excitation is critical in any PL measurement as the excitation energy and intensity will have profound effects on the PL signal. Because the absorption of most materials depends on energy, the penetration depth of the incident light will depend on the excitation wavelength. Hence, different excitation energies probe different regions of the sample. Since lasers are monochromatic, intense, and readily focused, they are the instruments of choice for photoluminescence excitation (PLE).

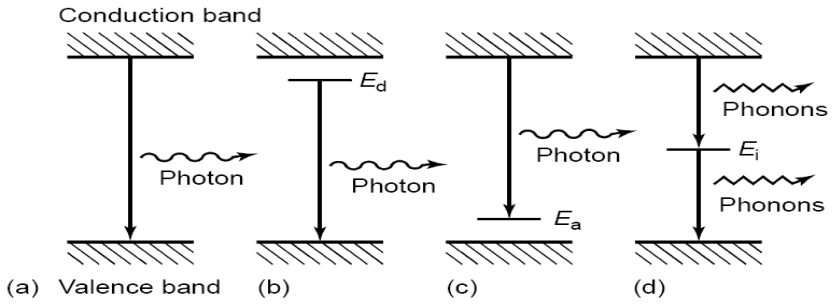

Figure 3.14 Principle of Photoluminescence
(a–c) Radiative recombination paths: (a) band-to-band; (b) donor to valence band; (c) conduction band to acceptor; (d) Nonradiative recombination via an intermediate state
(Reproduced with Permission, [11])

The PL spectrum can be analyzed to yield a wealth of information about the photoexcited material. The PL spectrum provides the transition energies, which can be used to determine electronic energy levels. The PL intensity gives a measure of the relative rates of radiative and nonradiative recombination. Variation of the PL intensity with external parameters like temperature and applied voltage can be used to characterize further the underlying electronic states and bands.

Moreover, features of the emission spectrum can be used to identify surface, interface, and impurity levels and to gauge alloy disorder and interface roughness. The intensity of the PL signal provides information on the quality of surfaces and interfaces. In addition, time-resolved PL can be very fast, making it useful for characterizing the most rapid processes in a material. The fundamental limitation of PL analysis is its reliance on radiative events. Materials with poor radiative efficiency are difficult to study via ordinary PL. Similarly, identification of impurity and defect states depends on their optical activity. Although PL is a very sensitive probe of radiative levels, one must rely on secondary evidence to study states that couple weakly with light.

3.3 Experimental Methods in Current Research

Prime grade Si (100) wafers of 2" diameter are used as a substrate for Pd ion implantation performed with a MEVVA (metal vapor vacuum arc) ion implanter. The lowest possible extraction voltage to produce a stable ion beam in the implanter (of 10 kV) was chosen to ensure maximum surface concentration of implanted Pd. Since the MEVVA ion source produces ions with multiple charge states, the energy of the ions emanating from the source depends on the charge state. For the Pd ion implantation, the energy was estimated to be 19 keV using a mean charge state of 1.9. A metal (Aluminum) mask with 14 equi-spaced circular holes each of 4 mm diameters was used in contact with the substrate held at room temperature to produce identical and well separated zones of ion implanted regions. Dose was varied from $5x10^{12}$ to $3x10^{16}$ Pd ions/cm^2. On the other hand, palladium was DC sputtered onto Si at a working pressure of 10 mTorr in the case metal thin film catalysis induced nanowire growth.

After the placement of metal catalyst, the furnace (MB 71 4" MBT Furnace, Thermco Products, CA) was ramped up to the desired temperature in the presence of Ar ambient. This minimized any interference from unwanted gaseous impurities and established a homogenous temperature gradient along the length of the tube. Care was taken to place the sample horizontally on a quartz boat with the implanted side facing up to ensure adequate contact with the carrier gas (Ar) flowing at 30 cm^3/min.

Morphological characterization of the wires was carried out using Hitachi SEM S800, S4800 SEM) fitted with an EDS detector. High resolution structural studies were carried out using transmission electron microscopy (FEI Tecnai F30 TEM) with SAED and EDS capabilities.

Surface functionalization of these nanowires was done using the chemical treatment with APTMS. Molecular dipole moment induced infra-red (IR) characteristics verifying the chemical affinity of these nanocomposites in the assay was obtained over a range of frequency (400 to 3000 cm^{-1}) with a resolution of 0.4 cm^{-1}. The sample was inspected under the Perkin Elmer FTIR spectrometer (after every routine of Raman) for the complimentary infrared absorption using a sealed and desiccated optical module. As a complementary technique, MicroRaman (ReniShaw^{TM}) spectroscopy was done using 514.5 nm Ar laser excitation at 24.6 mW averaged over two cycles of 10 sec exposure.

To synthesize optically active silica nanowire, ion-implantation of Er was carried out with 110 keV ErO^- SNICS source to fluences in the range from $5x10^{14}$ to $1x10^{16}$ $ions.cm^{-2}$. Investigating their optical activity, photoluminescence (PL) measurements of the Er emission were performed at room temperature using the 488 nm line of an argon ion laser as the excitation source.

The luminescence emission was analyzed with a Triax 320 spectrometer equipped with a high-sensitivity liquid-nitrogen cooled germanium detector. The excitation laser was mechanically chopped at 15 Hz and standard lock-in techniques employed to collect the spectra. For time-resolved PL measurements, the output of the detector was connected directly to a digital storage oscilloscope and the response averaged over 128 cycles. The time response of the system is estimated to be less than 0.5 ms.

3.4 Summary

This chapter provided a brief introduction to ion beam based modification of materials with a review on basic concepts of ion implantation. Then, the various microscopic techniques for nanowire characterization employed in this work have been discussed. Further, spectroscopic methods including IR, Raman and PL have also been mentioned. Then, the experimental methods and techniques used in the current research were mentioned. The following chapter discusses the results and discussion of the various experiments performed in this research that involves selective growth, manufacturing aspects, characterization and sensing applications of silica nanowires.

3.5 References

[1] R. Ohl, “Properties of Ionic Bombarded Silicon”, J. Bell Syst.Tech 31 (1952), 104

[2] D.C Jacobs., “The Role of Internal Energy and Approach Geometry in Molecule/Surface Reactive Scattering”, J. Phys. Condensed. Matter 7 (1995), 1023

[3] T. Takagi, “Ion Beam Modification of Solids: Towards Intelligent Materials”, Materials Science and Engineering A 253 (1998), 30

[4] J.F. Ziegler, “Ion Implantation: Science and Technology”, Academic Press Hardcover (1998)

[5] G. Dearnaley, “Ion Implantation”, Annual Review of Materials Science 4 (1974), 93

[6] M. Natasi and J.W. Mayer, “Ion Implantation and Synthesis of Materials”, Springer Series, (2006)

[7] J.S. Willams, and J.M. Poate, “Ion Implantation and Beam Processing”, Academic Press Inc (1984)

[8] I.G. Brown, “Vacuum Ion Sources”, Review of Scientific Instruments 65 (1994), 3061

[9] E.Rimini, “Ion Implantation: Basics to Device Fabrication”, Springer International Series (1994)

[10] D.B. Williams and B.C. Carter, “Transmission Electron Microscopy: A textbook for Materials”, Science, Plenum Press (2004)

[11] T.H. Gfroerer, "Photoluminescence in Analysis of Surfaces and Interfaces", Encyclopedia of Analytical chemistry (2000), 9209

Chapter 4

Results and Discussion

In this chapter, the experimental results and the associated discussions on manufacturing, characterization and applications of silica nanowires are presented. The first section details on the selective synthesis of silica nanowires on silicon using ion implantation based seeding approach and metal thin film catalysis. Next, the manufacturing aspects of these nanowires such as the growth model, growth rate, re-usability of the catalyst and high density synthesis are discussed. The latter part of this chapter deals with surface modification of silica nanowires and subsequent applications. Biosensing applications of these nanowires including its use as Surface Enhanced Raman (SER) substrate and as an immunoassay template have been presented. Further, the synthesis of optically active silica nanowires has been discussed along with its role as an effective erbium sensitizer. Finally, silica nanowires as reinforcement agent in a polymer matrix have been demonstrated.

4.1 Selective Synthesis of Silica Nanowires on Si Using Ion Implantation Based Seeding Approach

As nanowires will be a critical interconnect element of any nanosytem, the ability to produce them at a desired location, in a controlled manner, is of great importance. As mentioned earlier, silica nanowires are subject of intense research due to its wide variety of applications. Of the several methods used to produce nanowires, the VLS mechanism proposed by Wagner and Ellis in 1964 for silicon whisker growth has proved to be very reliable for developing silica nanowires. A recent simulation study [2] indicates the feasibility of forming catalyst nanoclusters in silicon using ion implantation. In this letter, ion implantation [1] as a new method for formation of catalyzing seed nanoclusters at or below the surface of the substrate and growing nanowires has been reported. It would have several advantages over the conventional methods. Some of the unique advantages being their sizes and distribution can be accurately controlled by varying the ion dose, energy, and dose rate. Also, the placement of catalyst being an integral part of the substrate lattice lends for an impurity free nanowire growth.

4.1.1 Experimental

In this research, prime grade Si (100) wafers of 2" diameter were used as substrates for Pd ion implantation performed with a MEVVA (metal vapor vacuum arc) ion implanter. The lowest possible extraction voltage to produce a stable ion beam in the implanter (of 10 kV) was chosen to ensure maximum surface concentration of implanted Pd. Since the MEVVA ion source produces ions with multiple charge states, the energy of the ions emanating from the source depends on the charge state. For the Pd ion implantation, the energy was estimated to be 19 keV using a mean charge state of 1.9. Circular shadow mask (Al) was used to define identical and well separated zones of ion implanted regions. Dose was varied from $5x10^{12}$ to $3x10^{16}$ Pd ions/cm^2. The sample was introduced into the furnace around 1100^0 C and heated for the desired time (7 – 60 mins) followed by cooling to room temperature.

4.1.2 Results and Discussion

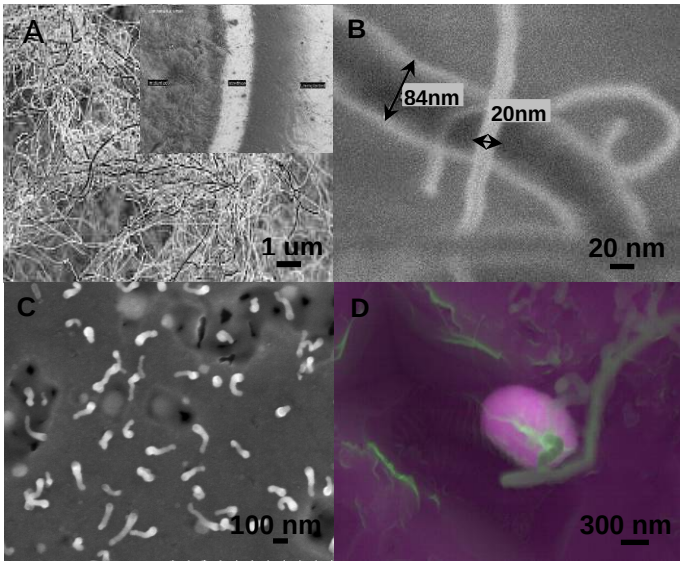

Figure 4.1 Selective Growth of Nanowires at a Constant Pd Ion Dose of $3x10^{16}$ ions/cm^2 After Heating at 1100^0C for 60 and 7 mins

(A) Dense wire growth after 60 min; inset – Selective growth on implanted regions

(B) Variation in morphology of wires in (A), (C) Early stage of nanowire growth (after 7 min) and (D) Composite of backscattered and scanning electron image highlights the elemental contrast between seed and wire.

(Reproduced with Permission, [1])

After heating at 1100 ^{0}C for 60 minutes, the ion implanted region showed a dense growth of rather long and interwoven nanowires as shown in figure 4.1A. The inset shows the unimplanted area at the same magnification confirming the absence of nanowires due to unavailability of Pd seeds. Also, figure 4.1A demonstrates the selective nucleation of nanowires on the implanted region. The interface region is very narrow and sharp indicating the ability to directly locate nanowires on the implanted areas. The nanowires grow with diameters ranging from about 15 to 90 nm, as for example seen in figure 4.1B.

The length of the nanowires was observed to vary up to about 50 μm corresponding to an aspect ratio of up to 3000. The morphology of the nanowires depends on the growth time as evident from figure 4.1C (after 7 min) captured at the early stage of the growth with nanowires emanating from their parent seeds. Figure 4.1D is a composite constructed from an overlay of two SEM micrographs recorded in backscattered mode (pink color) and secondary mode (green color). The pink areas therefore show atomic number contrast. The pink oval seed is confirmed to be rich in Pd by spot EDS measurements on and away from it. Figure 4.1D therefore captures the "birth" of a silica nanowire (green color) growing from a Pd rich seed (looking like an oval shaped "egg").

A much thinner nanowire can also be seen to emerge from the same seed. Properties of the nanowires were studied in detail as follows: The composition was measured with EDS (at low electron energy of 5 kV to ensure that majority of x-rays come from nanowires and not from Si substrate) and compared with that of a control sample of quartz analyzed under identical EDS conditions (figure 4.2A). Thus the composition was found to be close to SiO_2 with a slight deficiency of oxygen. The phase identification was done by XRD on the same sample (figure 4.2B), which did not show the peak observed in quartz sample indicating that the nanowires are amorphous.

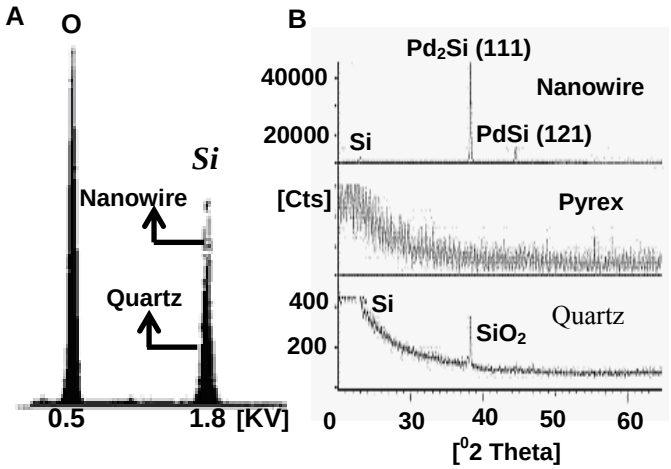

Figure 4.2 Elemental Composition and Texture Analysis of the Synthesized Nanowires (A) Comparison of EDS spectra on quartz with EDS on nanowire sample revealing SiO_x ($x<2$) stoichiometry and (B) XRD showing their amorphous nature. (Reproduced with Permission, [1])

The temperature is found to be a critical factor for the growth of nanowires. At a lower temperature of 1010 ^{0}C for the same growth time of 60 mins, we observe only a very early stage of nucleation and growth, similar to that in figure 4.1C. At still lower temperature of 910 ^{0}C (figure 4.3A), no growth of nanowires is observed. Pd ion dose was also found to be another factor critical for nucleation of Pd rich seeds and nanowires. By a comparison with results in figure 4.3B and figure.4.2C, it is clear that the nanowires are mixed with particles/seeds of the two PdSi phases.

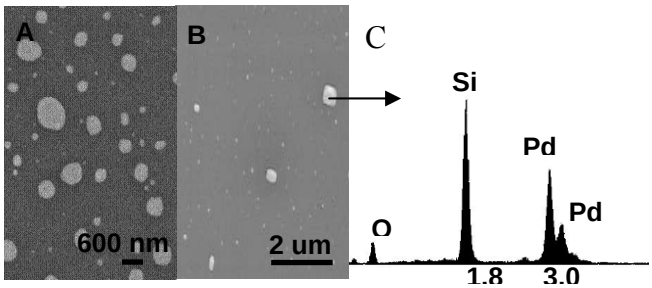

Figure 4.3 Conditions of No Nanowire Growth at a Constant Pd Dose of 3 x10^{16}/cm^2
(A) 910 °C, Ar flow—absence of nucleation, (B) 1100^0 C, no Ar flow—formation of large whitish islands and (C) Spot EDS confirming the presence of palladium silicides on the large islands.
(Reproduced with Permission, [1])

As the dose was reduced from 3E16/cm^2 (figure 4.4A) to 1E16/cm^2 (figure 4.4B), coiled nanowires of reduced density were seen. The density of the wires was estimated by counting the wires in five 4µm x 4µm (high dose), 7 µm X 7 µm regions (low dose) of the SEM and averaging them. The observation show an estimated 2E8 wires /cm^2 in sample implanted with a dose of 3E16/cm^2 (figure 4.4A) and 1E8 wires /cm^2 in sample implanted with at a dose of 1E16/cm^2 (figure 4.4B). These observations confirm that implantation does is a critical factor in determining the density of the nanowires.

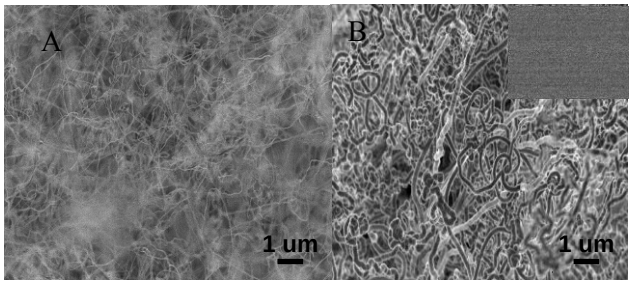

Figure 4.4 Effect of Implanted Dose on the Growth of Nanowires Heated at 1100^0C for 60 mins
(A) 3x10^{16} ions/cm^2—high density thinner nanowires and (B) 1x10^{16} ions/cm^2—thicker coiled nanowires of reduced density, inset: 5x10^{12} ions/cm^2—absence of nanowires.
(Reproduced with Permission, [1])

However at a dose of 5E12 ions/cm^2, no growth of nanowires (inset in figure 4.4B) or Pd rich seeds was observed. Moreover, the flow of Ar gas was found to be critical in producing growth of silica nanowires. In another experiment at 1100^0 C, the Ar gas was shut off after the furnace temperature reached 1100 ^{0}C, and then the sample was introduced into the furnace and kept there for 60 minutes; after which the furnace was allowed to cool down to room temperature and the sample was taken out for further study by SEM and XRD. The SEM results showed islands of bright appearance (figure 4.3B). Larger islands with rectangular morphology were confirmed to be consisting of Pd_2Si composition by performing a spot EDS on them (figure 4.3C). The composition of smaller islands could not be determined accurately because their size was much smaller compared to the excitation volume for the EDS. They appear to be the Si rich PdSi phase. Away from islands, no Pd was found. There were no nanowires on this sample. XRD obtained from this sample shows the presence of Pd_2Si and PdSi phases. The absence of silica nanowires proves the role of Ar as a carrier gas in transporting Si vapor to the reaction site resulting in the whisker growth by a VLS mechanism.

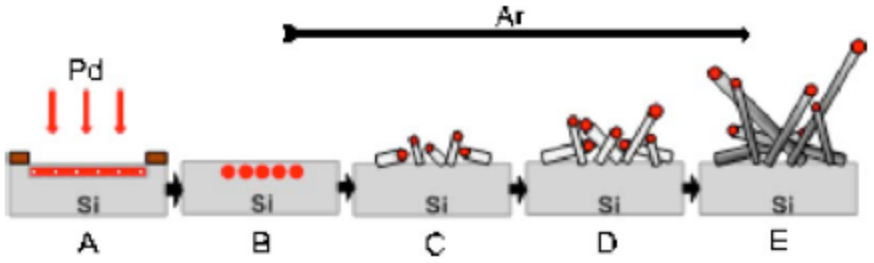

Figure 4.5 Schematic of the Proposed Physical Model Explaining Ion Implantation Based Seeding Approach

(A) Implanted Pd on Si (100) through a mask, (B) formation of PdSi cluster, and (C–E) VLS growth of silica nanowires.

(Reproduced with Permission, [1])

The physical model to explain our observations is proposed (figure 4.5) to be as follows: the ion dose needs to be high enough to produce nanoclusters of Pd within the silicon matrix amorphised by ion damage. As the implanted sample is heated in Ar atmosphere, the interdiffusion at the Pd-Si interface produces two phases of PdSi and Pd_2Si which eventually become liquid as the melting point of the silicides is approached at 972 ^{0}C or 1331 ^{0}C respectively [3]. Since the maximum temperature used in our study is 1100 ^{0}C, only liquid drops of PdSi phase are formed.

These liquid drops may now coalesce to form larger sized liquid drops and migrate towards the surface of the solid Si substrate. The amorphised surface layer of silicon would also crystallize concurrently. When these liquid drops are exposed to the Si vapor being swept across by the carrier gas (Ar), the VLS model of whisker growth comes to play and Si nanowires begin to grow.

Some nanoclusters, especially those on which nanowire growth has not yet started, agglomerate by diffusion/Oswald ripening processes, become bigger in size and nucleate wires. The growth process proceeds continuously by diffusion and precipitation of silicon atoms across the liquid–nanowire interface. Since small amount of oxygen is inevitably present in the ambient as impurity, these thin silicon nanowires may oxidize rapidly from outside and eventually get fully oxidized. The observed oxygen deficit (figure 4.2A) from the stoichiometric SiO_2 may be consistent with some unoxidised silicon around the centre of the nanowires.

The occurrence of selective VLS growth of nanowires only on the Pd ion implanted regions has been validated by our careful selection of ion dose, growth temperatures and Ar gas flow. The VLS growth can stop when either of the following conditions are met – no more vapors of Si arrive (figure 4.3B) or the temperature drops below the melting point of the material of the liquid drop (figure 4.3A), or the implanted ion dose is below that required for Pd cluster formation (the case of our sample implanted with 5E12 ions/cm^2). However, the origin of the observed morphology of silica nanowires is unclear. The nanowires are produced with a variety of diameters and have much larger lengths forming a network of entangled structures (figure 4.1A). Since our model is based on VLS growth of Si nanowires followed by their oxidation, one can expect the dominant growth direction to be (110) on a (100) substrate surface [4] so that the nanowires would point out at +/- 45 ^{0} with respect to surface plane. However, the SEM views of the early stage of growth (figure 4.1C) do not show such large angles. They appear to be coming out almost along the surface at much smaller angles. This observation appears to be in agreement with recent reports of diameter dependent growth directions of epitaxial Si nanowires grown on Si (100) substrates using Au as liquid catalyst facilitating VLS growth [5]. It was found that Si nanowires grown epitaxially on Si (100) via the VLS growth mechanism change their growth direction from <111> to <110> at a cross over diameter of approximately 20 nm.

A model has been proposed [6] for the explanation of this phenomenon. Based on this model, we can hypothesize that most of our nanowires with diameters greater than 20 nm grow along <211> or <111> or a mixture of these growth directions and therefore lie close to the substrate plane (within about +/-18 ^{0}). As the diameter of the nanowires changes, so does the growth direction leading to the observed entanglement of the nanowires. A similar change with decreasing diameter of the nanowires from <111> to <110> direction has also been observed for non-epitaxial Si nanowires [7].

4.1.3 Conclusions

In summary, a new method for selective growth of silica nanowires on silicon wafers has been proposed by using ion implantation through a mask. This process has been demonstrated by use of Pd ions implanted into Si (100) to form nanoclusters of Pd to act as catalyst silicide seeds for nanowires growth in a quartz furnace with Ar as carrier gas. The vapor-liquid-solid (VLS) model of nanowires formation has been shown to be valid for this process by a set of careful growth conditions. Since ion implantation is compatible with the standard top-down CMOS process, this method holds a great potential for facilitating directed bottom-up growth of nanowires on silicon wafers. It may also provide an opportunity to combine the top-down and bottom-up technologies for creation of robust nanoscale devices. It may therefore open doorway to a large number of applications in wide areas of new technologies such as on-chip optoelectronics, biosensors, micro-antennae and metallic nano-tubes.

4.2 Selective Synthesis of Silica Nanowires on Silicon Catalysed by Pt Thin Film

Selective growth of amorphous silica nanowires on a silicon wafer [8] deposited with Pt thin film is reported in this section. The motivation was to circumvent the need for ion implantation as a tool for the placement of the catalyst. Also, the ability to produce stable nanowires at desired locations in a controlled manner on planar substrates is of critical importance for fabricating nanodevices such as nanoFETs, nanotransistors and microphotonic nanosytems. In this context, this research has focused on the selective growth of silica nanowires in silicon using Pt thin film through a mask. This synthesis approach for localization offers several advantages such as the tunable size and distribution of the parent nanoclusters and a cost-effective solution for growing large-scale arrayable nanowires

4.2.1 Experimental

Prime grade 2" n-type silicon wafers were used as substrates for subsequent Pt deposition. Target Pt thickness of 2 nm, 3 nm, 5 nm, 10 nm and 100 nm was sputtered onto Si substrate. The temperature of heating is chosen based on the Pt-Si phase diagram. High purity Ar was chosen as carrier gas and was set to 30 sccm through out the course of the experiment. Initially the furnace was flushed with Ar to minimize interference from gaseous impurities. Then the sample is introduced into the furnace and ramped up to 1200^0 C. Once the furnace reaches 1200^0 C, the heating process is timed. It is heated for 1 hr and then cooled down to room temperature.

4.2.2 Results and Discussion

After heating at 1200^0 C for an hour, regions deposited with Pt (20 nm) showed dense growth of interwoven nanowires. Figure 4.6A demonstrates selective growth of nanowires clearly identifying the nucleation area and regions devoid of nanowire due to absence of Pt film. A higher magnification SEM micrograph taken in the growth region (Figure 4.6B) illustrates nanowires of varying morphology. The nanowires grow at an average diameter of 200-500 nm (Figure 4.6C) with lengths varying from 20 to 75 μm giving rise to high aspect ratio nanostructures for biological applications. Morphology of these nanowires depends on growth time as evident from figure. Figure 4.6D is a schematic capture of birth of several nanowires from their parent seed.

The composition of these nucleated nanostructures from low energy EDS was found to be SiO_2 closely matching with the EDS spectra of a control sample of quartz analyzed under similar test conditions. Phase identification through XRD revealed the amorphous (as compared to a quartz sample) nature of the wires along with the formation of PtSi, which acts as a seed catalyzing the nanowire growth. This is in congruent to compound outlined in Pt-Si phase diagram under similar experimental conditions.

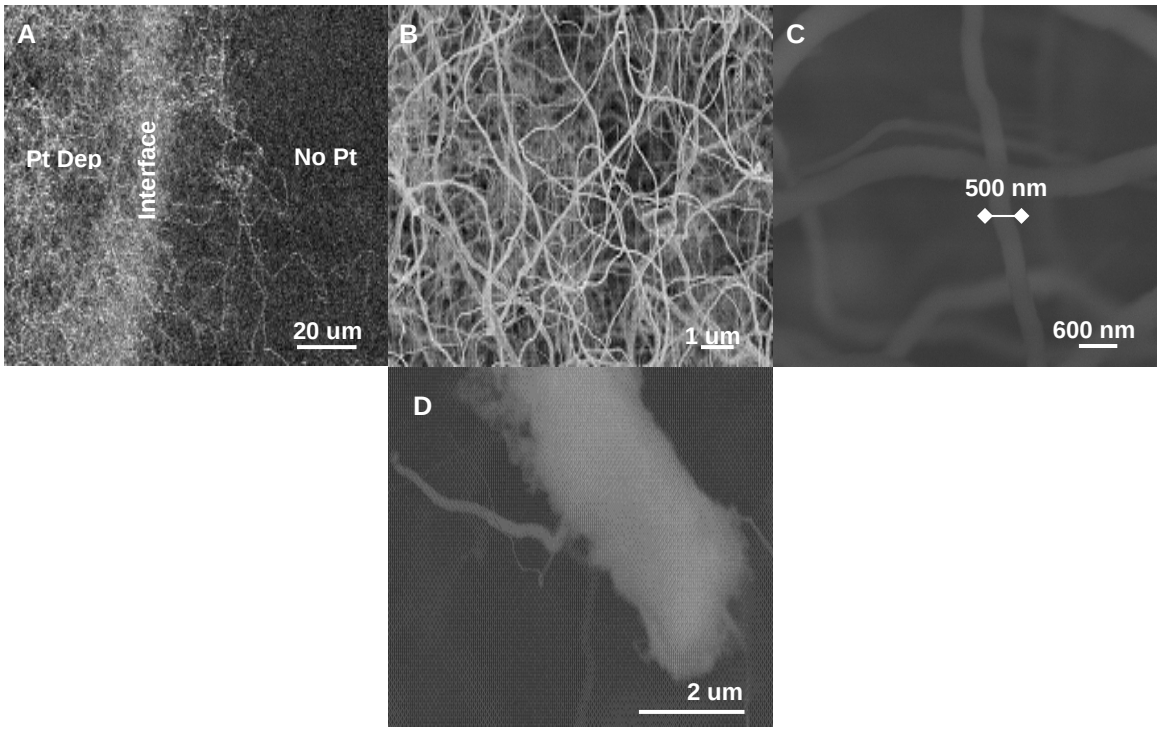

Figure 4.6 Selective Growth of Nanowires after Heating at 1200°C for 60 mins for a Pt Thickness of 2 nm

(A) Localized growth of nanowires (B) Higher magnification image in area of nanowire growth indicating the varied morphology of nanowires (C) Size of nanowires – diameter ranging from 50-500nm and (D) Early stage of nanowire growth captured after heating at 1200^0C for 15 mins (Reproduced with Permission, [8])

The TEM micrograph (figure 4.7A) confirms the amorphous nature of the interwoven oxide nanowires. Observed variation in nanowire morphology is attributed to the non-homogenous seed size and time dependent ripening of the parent seed.

Figure 4.7B is a TEM image of a nanowire terminated with a metal particle differentiated by the dark contrast seen along its body validating the VLS growth model.

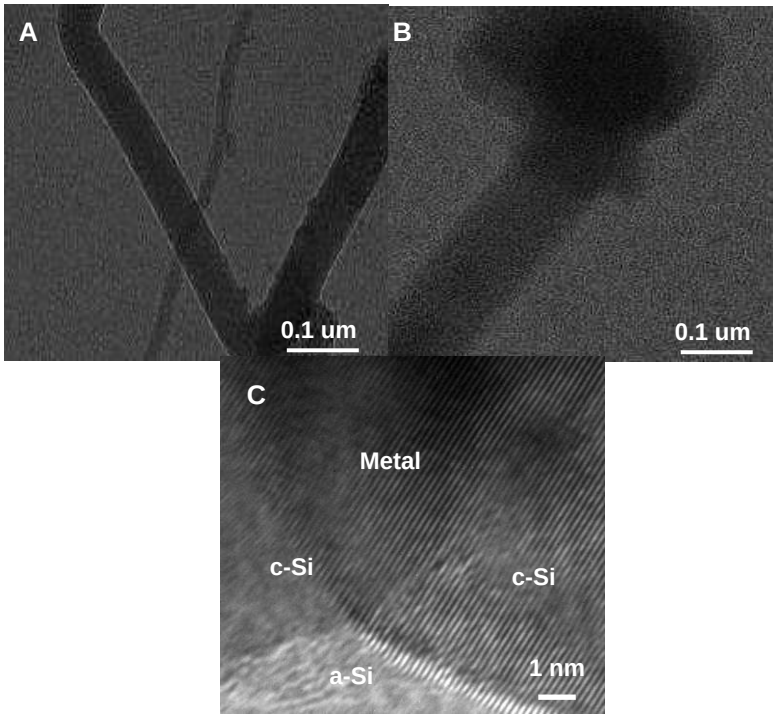

Figure 4.7 TEM Image of Silica Nanowires Synthesized at 1200°C for 60 mins for a Pt Thickness of 2 nm

(A) Multiple amorphous nanowires arising from the same seed, (B) Metal particle (Pt) seen at the tip of the nanowire highlighted by the dark contrast and (C) HRTEM image identifying crystalline Si (c-Si) near the tip of the overlapping nanowires surrounded by amorphous (a-Si) region

(Reproduced with Permission, [8])

In addition, the HRTEM image captured near the tip of the overlapping nanowires (figure 4.7C) revealed the presence of crystalline Si (c-Si), confirming the initiation of Si wires and the observed stoichiometry. It is postulated that large-sized metal catalyst transported to the tip of the nanowires acts as a shadow mask, preventing oxidation at the neck of these nano-entities.

The thickness of platinum layer was found to be a critical factor affecting nanowire growth. As the thickness was increased to 3 nm, (keeping other experimental conditions constant), the number density of the nanowires reduced. Further reduction in number density was observed when scaled up to 5 nm. At a thickness of 10 nm, silicide nanoclusters were formed indicating the absence of nanowire nucleation. When the deposited platinum thickness was around 100 nm, micron sized clusters were seen.

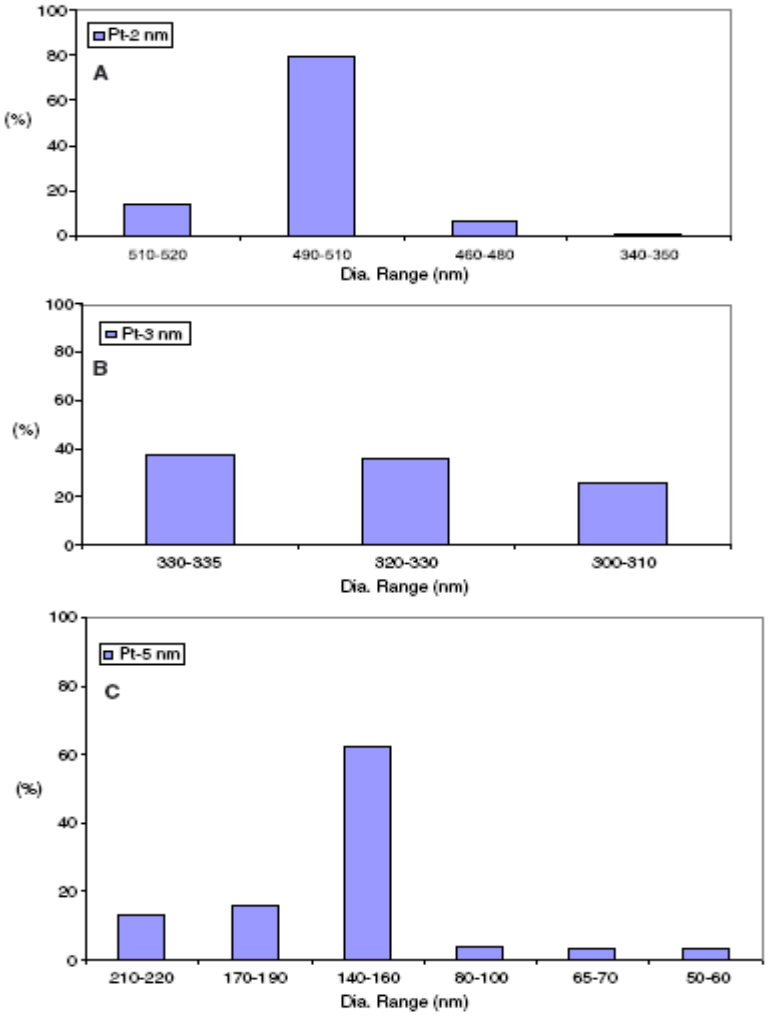

Figure 4.8 Percentage Histogram Indicating the Statistical Nature of the Growth Process with Varying Diameters for Different Pt Thicknesses

(A) Pt—2 nm: ensemble average diameter = 500 nm, $\sigma = 6.7$; (B) Pt—3 nm: ensemble average diameter = 319 nm, $\sigma = 9.1$; and (C) Pt—5 nm: ensemble average diameter = 146 nm, $\sigma = 7.4$. (Reproduced with Permission, [8])

Figure 4.8 illustrates the statistical nature of the growth process through a frequency histogram. All the nanowire samples with different Pt thicknesses were heated to 1200^0 C for 1 h. For a Pt thickness of 2 nm, the ensemble diameter average was found to be 500 nm with a standard deviation (σ) of 6.7 over the 79% range. A uniform distribution with an average wire diameter of 319 nm (σ = 9.1) was observed for the 3 nm Pt sample. As the platinum thickness increased to 5 nm, the nucleated nanowires exhibited a wide range of (60– 220 nm) diameter variation explained by the Oswald ripening process. The average diameter was found to be 146 nm (σ = 7.4) over the 62% range.

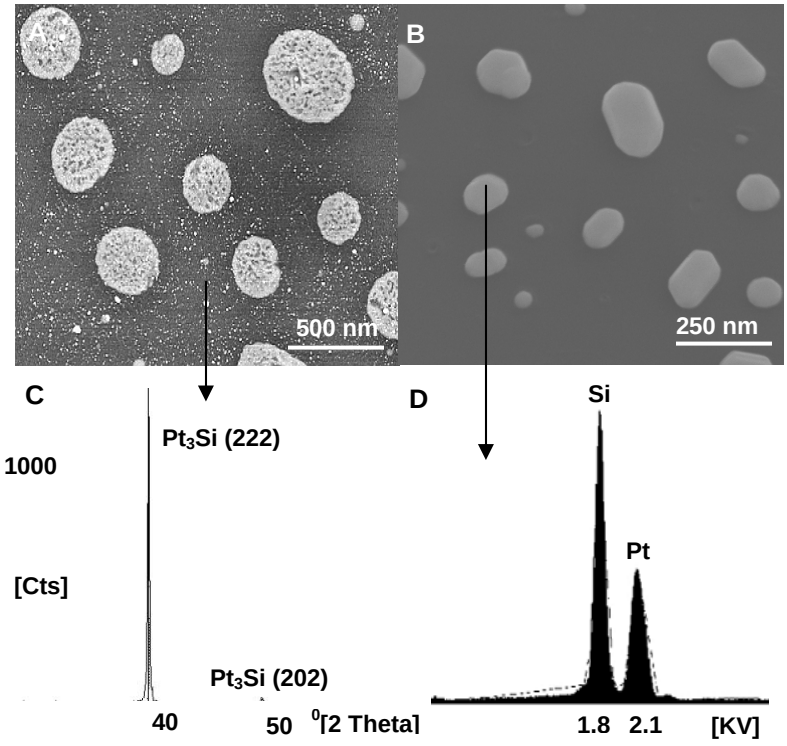

Figure 4.9 Conditions of No Nanowire Growth for Samples Deposited with 2 nm Pt Thickness (A) 950°C, 1hr – XRD indicating the formation of Pt_3Si and (B) 1200°C, 1hr, No Ambient – EDX spectra revealing PtSi atomic stoichiometry of seeds
(Reproduced with Permission, [8])

The heating temperature was also found to be a critical factor influencing nanowire growth. At a lower growth temperature of 950^0 C for 1hr (figure 4.9A), spherical islands appeared surrounded by nanoclusters.

These islands were identified as Pt_3Si particles through XRD. Testing the role of ambient in nanowire growth, the flow of Ar was intentionally shut off while ramping up the furnace to 1200^0 C. When the sample was analyzed in a SEM, rectangular islands of bright appearance (figure 4.9B) were observed. Larger islands were confirmed to be PdSi by composition through an EDS on them. Smaller islands could not be resolved elementally due to limitation on the excitation volume for the EDS. The absence of silica nanowires proves the role of Ar as a carrier gas in transporting Si vapor to the reaction site resulting in the whisker growth by a VLS mechanism.

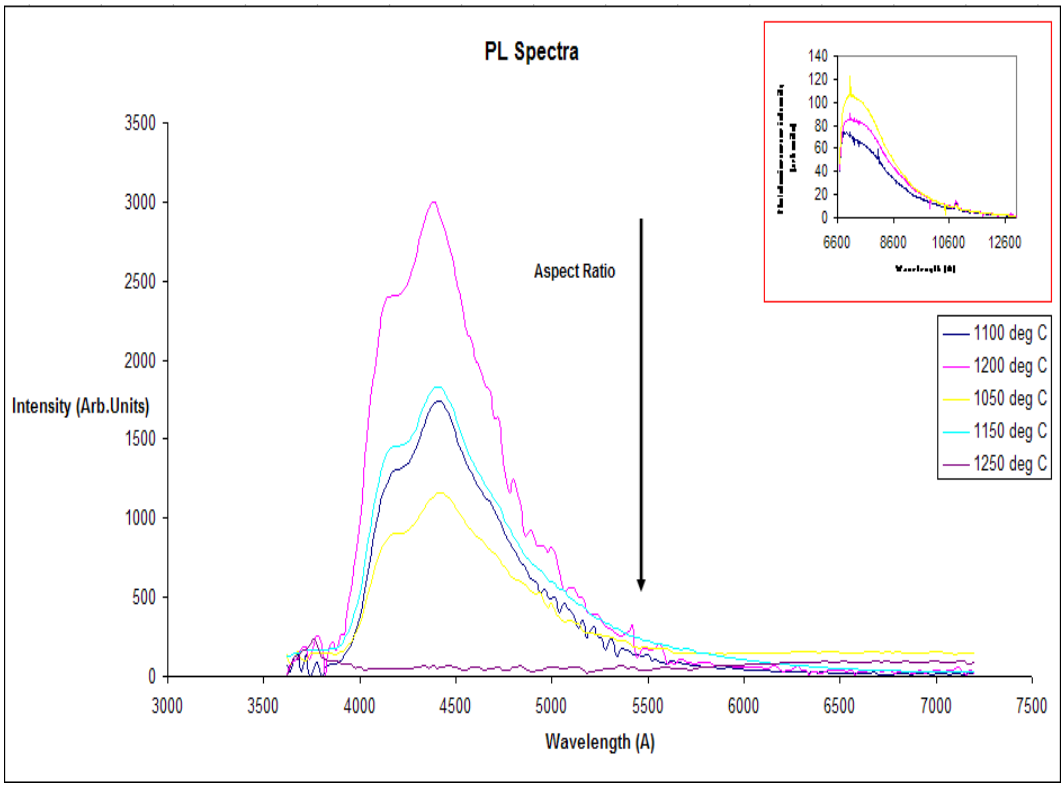

Figure 4.10 Room Temperature Photoluminescence Spectra of Silica Nanowires as a Function of Growth Temperature

Blue Light Emission at 430 nm, Inset: PL observed at higher wavelengths.

(Reproduced with Permission)

Investigating the optical activity of nanowires, two photoluminescent peaks (380 nm and 450 nm) are observed (figure 4.10) the blue light emission under 7.9 eV excitation. It is apparent that considerable amount of oxygen is involved in the growth of these nanowires. The oxygen may have come from the residual gas in the reaction chamber.

Defect centers, arising from insufficient oxygen supply, during nanowire formation are postulated to be cause for the observed photoluminescence.

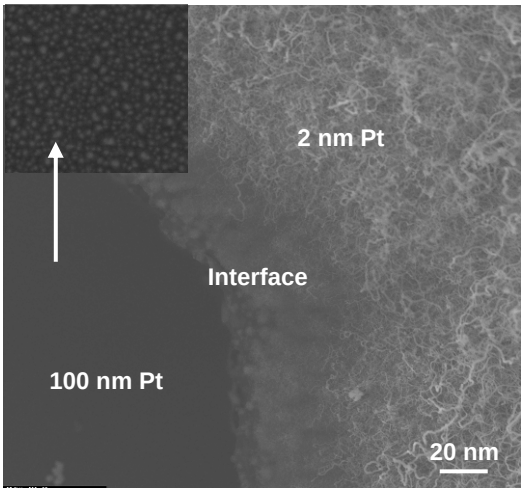

Figure 4.11 Sample Coated with Differential Pt Thicknesses Heated at 1200^0C for 1 hr (Reproduced with Permission, [8])

Exploiting this selectivity of nanowire growth to platinum film thickness, a Si substrate with differential Pt coating (differential thickness achieved through repeated application of shadow mask) resulted in the nucleation of nanowires (figure 4.11) while simultaneously forming optically conducting silicide in a single furnace treatment. This would facilitate a low loss hybrid nanointerconnect scheme in silicon for future integrated optical systems.

4.2.3 Conclusions

Selective growth of silica nanowires on silicon catalyzed by Pt thin film is demonstrated. Platinum silicide acts as the seed facilitating the bottom – up nucleation of the oxide nanowires. The nano scale optical wires nucleate following a VLS model validated through a careful set of growth conditions. This approach represents a simple, flexible and cost-effective solution for synthesizing large scale silica nanowires for wide variety of future applications that include functional microphotonics, high density optical nanointerconnects, high resolution optical heads and nanoantennae. In particular, simultaneous formation of an optically conducting silicide along with localized growth of nanowire holds great potential for realizing hybrid optical interconnect scheme for future integrated optical systems.

4.3 Manufacturing Aspects of Silica Nanowires

Scalable nanoscale manufacturing methods are required to harness the benefits of nanotechnology for a variety of applications. Cheap and large scale production of nanosensors and nanoscale devices require mass manufacturing of their fundamental building block (eg. nanocomponents). In this context, this research sub-section deals on the manufacturing aspects of silica nanowires. Understanding the fundamental nucleation and growth mechanism of nanowires is vital to their high density synthesis. Also, many applications require varying growth requirements and nanowire morphologies. Though, the nanowire growth was shown to follow VLS model, the precise mechanism by with silica nanowires grows remains uncertain and the dominant mechanism likely depends on the precise experimental conditions employed for their synthesis.

4.3.1 Experimental

In this work [9], the growth mechanism would be explored in detail along with the estimation of growth rate and the necessary conditions for nanowire growth catalyzed by metal thin film. Also, the re-usability of the silicon substrate for further nucleation would be evaluated after nanowire growth. The growth model for synthesizing nanowires was verified by a combination of experiments such as:-

(a) Annealing the implanted or metal thin film silicon wafer in the absence of vapor,

(b) Removing the nanowires in HF to inspect the substrate after growth, and

(c) Vary the Ar flow rate and

(d) Exploring growth using a time sequence (10- 45 min) study

Further, the growth rate was estimated using the weight differential of nanowires with varying heating time. A generic time and temperature model has been proposed.

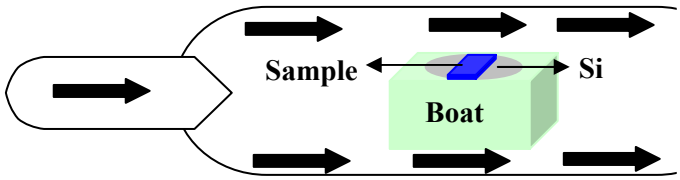

Figure 4.12 Schematic of the Furnace and Experimental Set-up

4.3.2 Results and Discussion

Figure 4.12 is a schematic representation of the open tube furnace. In the case of nanowire synthesis by metal thin film catalysis, a blank Si is kept on top of a quartz boat. A small piece of the Pd coated Si wafer is placed on top of the blank Si wafer. On the other hand, wires seeded by metal implantation based approach do not require a blank or base silicon wafer. The purpose of the base or blank Si wafer was to provide the Si vapor. Initially, the furnace was ramped up to 1100^0 C.

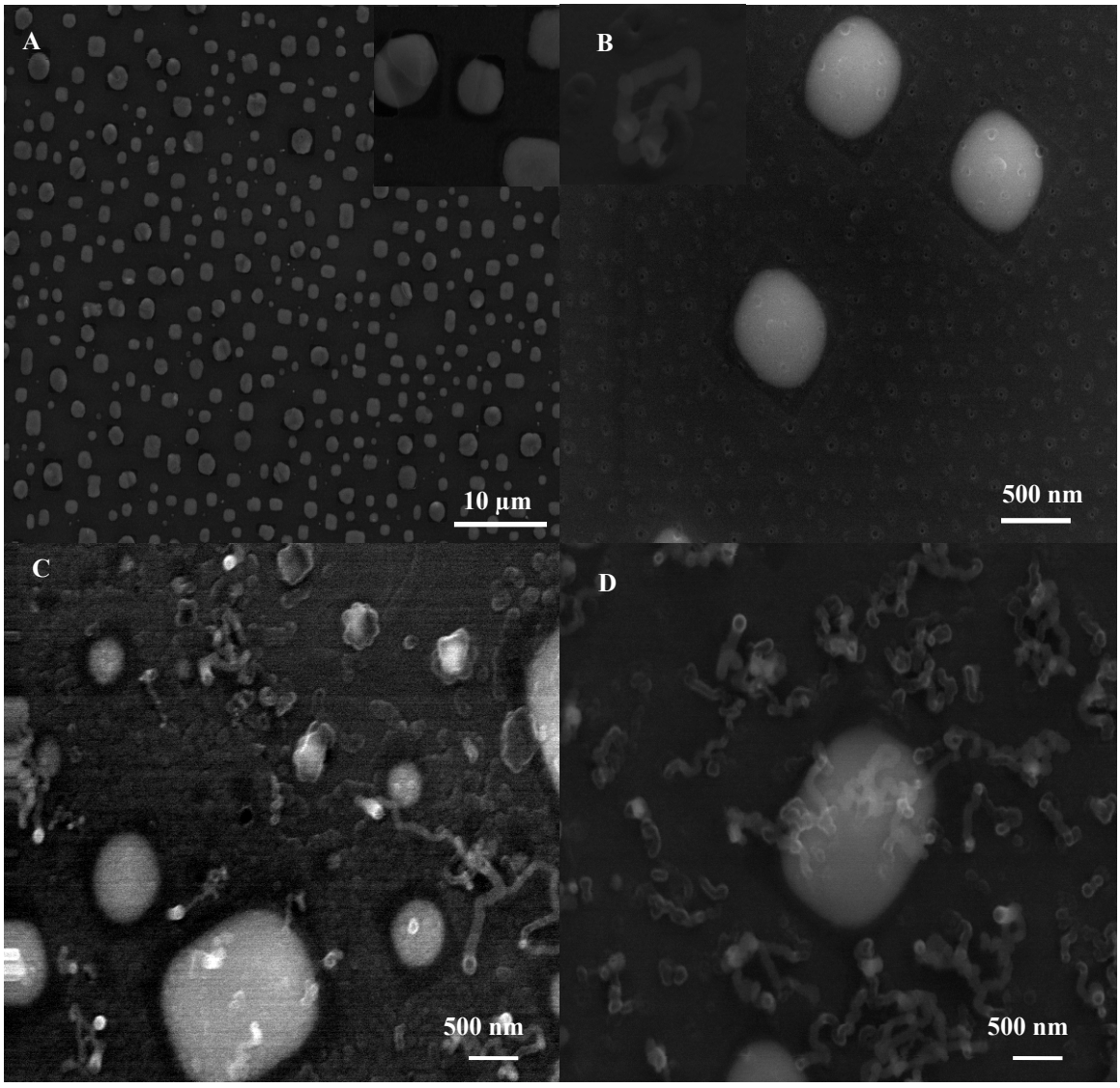

Figure 4.13 SEM Micrograph Illustrating the Morphology of the Pd Coated Si Wafer Heated at 1100^0C

(A) 10 mins, (B) 15 mins, (C) 20 mins and (D) 30 mins

Figure 4.13A shows nanoclusters of various shapes and sizes. An EDS inspection (figure 4.14 A) on one of the nanoclusters indicates the presence of Pd, Si and O.

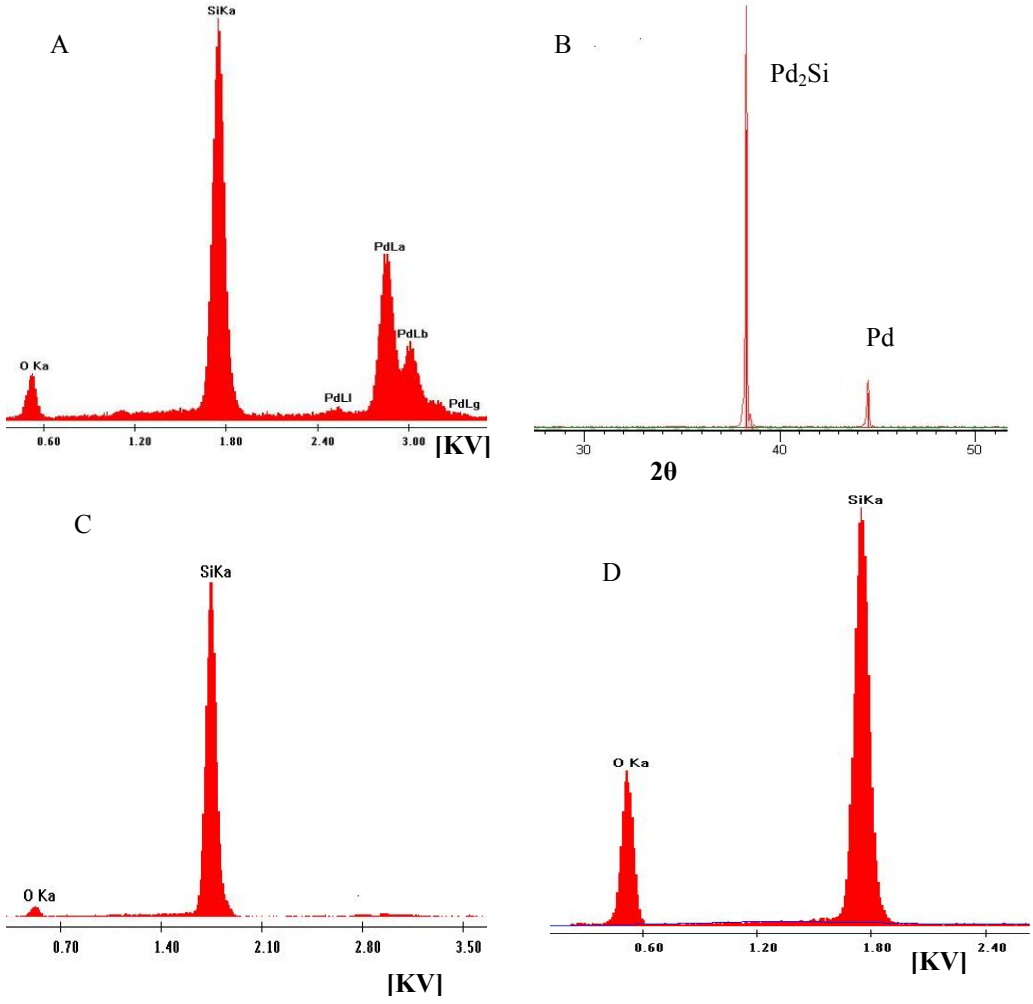

Figure 4.14 EDS Spectra and XRD Characterization of Pd Coated Si Samples Heated at 1100^0 C for Varying Time

(A) EDS on the Pd nanocluster shown in figure 2A, (B) XRD on the Pd nanocluster shown in figure 2A, (C) EDS spectra of the Thin Oxide Layer in figure 2A and (D) EDS Spectra on the Bunch of Nanowires

Further, the XRD (figure 4.14 B) results indicate the presence of crystalline Pd as well as the formation of palladium silicide with stoichiometry indicating the deficiency in Si. Also, a small layer (figure 4.13 A inset) covering the wafer surface surrounding the islands was noticed which was found to be thin oxide film (SiO_2, figure 4.14 C).

The extremely low partial pressure and concentration of oxygen in Ar is responsible for the formation of the oxide layer. However, deliberate introduction of oxygen at 0.001 SCCM level oxidized the substrate without forming the islands or the nanowires. The sample inspected after a heating cycle of 15 mins revealed surface roughening (figure 4.13 C) in the form of etched pits both on the surface of Si and palladium silicide island. This has been attributed to the disassociation of the thin oxide layer to volatile SiO with continuous supply of oxygen.

A similar phenomenon has been reported by Suzuki et al. [10]. Figure 4.14 C shows the SEM micrograph of a sample heated for 20 mins. The nucleation of nanowires could be observed along with ripening of the seeds to induce its birth. Localized Si etching was also observed along the catalyst periphery and subsequent sinking action of the nanoclusters was seen. As the eutectic alloy formation proceeds at high temperature, a tiny amount of Si diffuses from the substrate. Since there is no external supply of silicon, the silicide formation consumes silicon from the surrounding which gives the appearance of Si etching. Peng et al. [11] utilized the metal induced Si etching behavior along with nanolithography to synthesize ordered Si nanowires. As the nanoclusters vary in size distribution (several μm to nm), some of the nanowires seems to originate from silicon. The number density of nanowires increased two fold upon inspecting a sample heated at 1100^0 C for 30 mins.

EDS spectra on a bunch of nanowires (figure 4.14 D) away from the palladium nanocluster indicate Si and O composition. Extracting the stoichiometry by background subtraction reveals SiO_x ($1.8<x<2$) indicating a deficiency in silicon. Therefore, unfulfilled oxygen sites exist which makes these nanowires more reactive. The number density of nanowires increased for samples heated for 45 mins (figure 4.15). Also, the inset in figure 4.15A shows the reduction in the size of nanoclusters at the expense of nanowire growth.

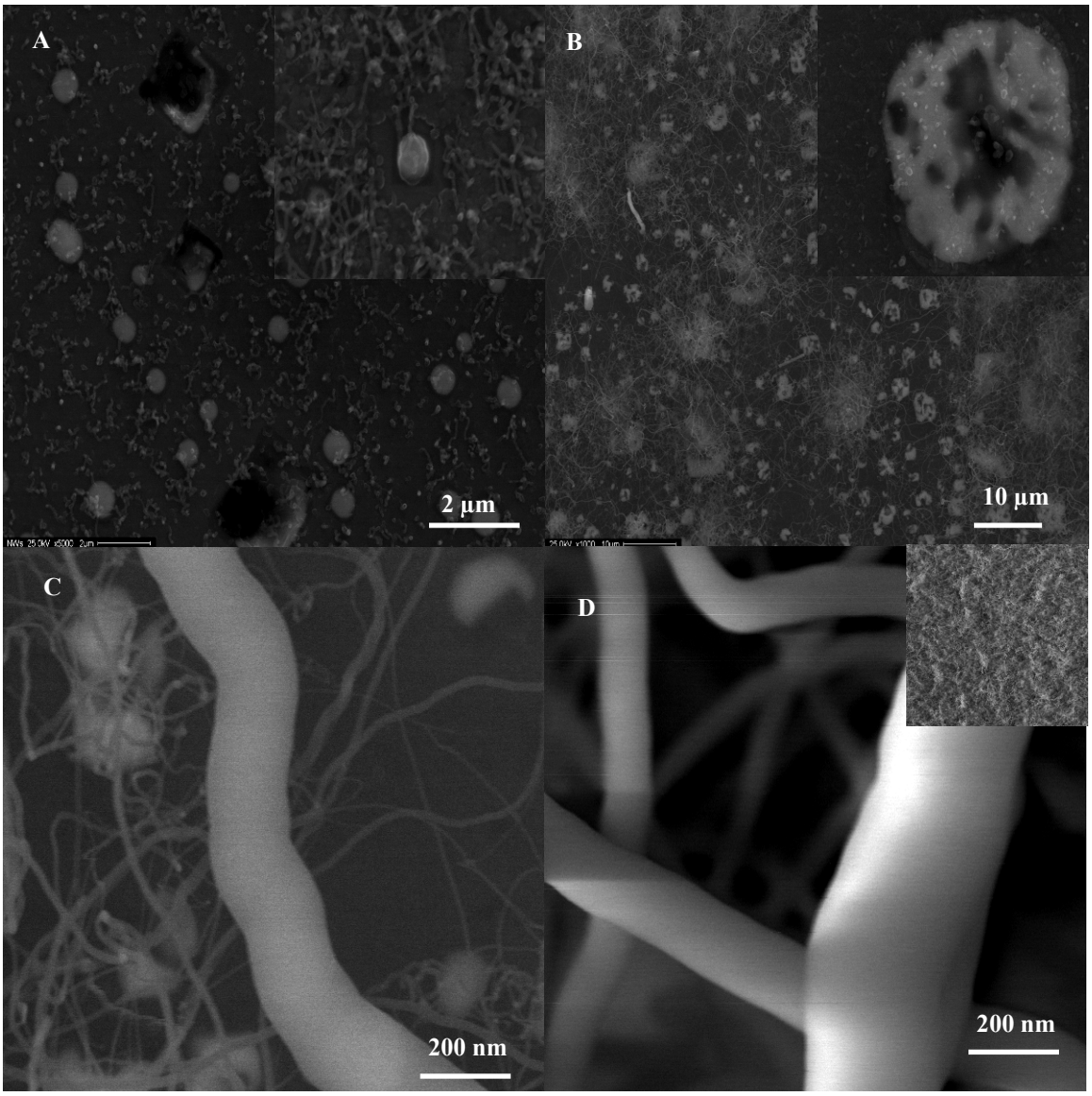

Figure 4.15 SEM Micrograph Illustrating the Morphology of the Pd Coated Si Wafer Heated at 1100^0C

(A) 45 mins, (B) 60 mins, (C) 75 mins and (D) 90 mins

Table 4.1 Comparison of Number Density of Nanowires

Time (mins)	Number Density of Wires (x 10^{12} wires/m^2)
20	1
30	2
45	3
60	5
75	6
90	8

Table 1 indicates the progressive increase in the number density of nanowires for 20, 30, 45, 60, 75 and 90 mins. Figure 4.15B shows bunches of nanowires along with secondary nucleation (inset) from the nanocluster. High aspect ratio nanostructures were seen on samples heated to 75 mins (figure 4.15C) along with size reduced parent nanoclusters. Samples heated for 90 mins at 1100^0 C show intertwined nanowires (figure 4.15D) devoid of nanoclusters. The bushy growth of nanowires has been shown in the inset. Next the growth rate (figure 4.16) was estimated by measuring the weight differential of Si substrate before and after nanowire growth as function of growth time.

For heating times up to 20 mins, there is a small dip in the growth curve due to the removal of silicon which dominates the early nucleation of the nanowires. Time zone between 20 and 45 mins show a linear increase in the growth of nanowires. Samples inspected for 60, 75 and 90 mins show a prolific growth differential. The growth trend after 90 mins indicates the system reaching steady state. Further, the re-usability of the substrate was investigated by etching the nanowires off the Si substrate (1100^0 C, 90 mins) in HF and using the processed substrate again for nanowire growth. There was little evidence of re-growth as seen from the SEM micrograph shown in figure 4.17A.

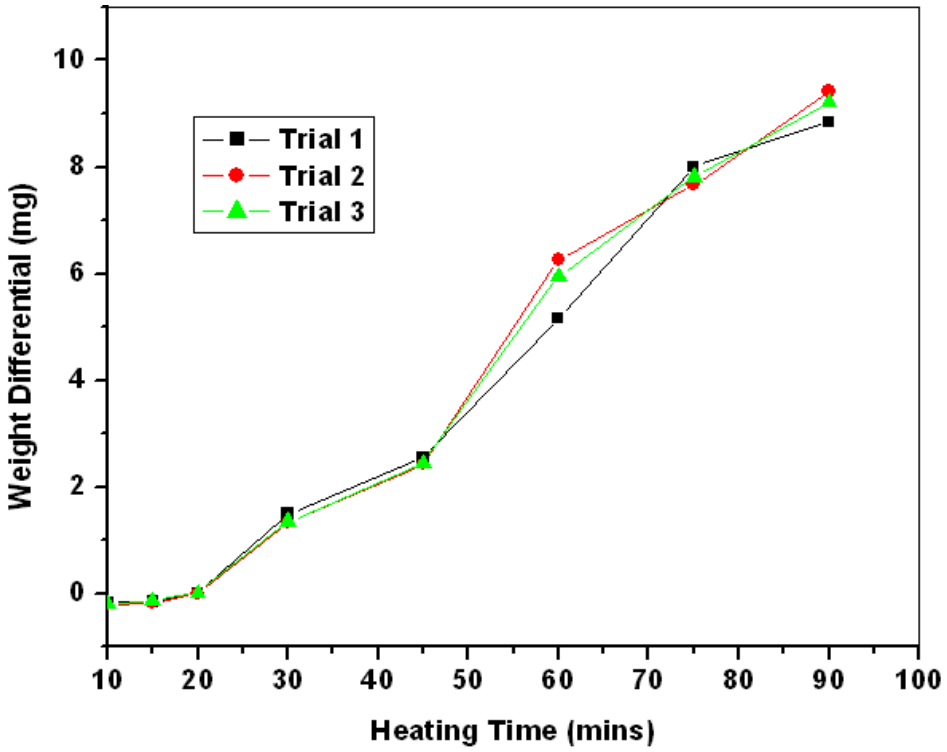

Figure 4.16 Schematic Illustrating the Growth Rate (Weight Differential) of Silica Nanowires as a Function of Heating Time

Some of the critical features observed or inferred from the nanowire growth are as follows:-

(a) The low concentration level of oxygen in Ar is the key to the growth of silica nanowires. Absence of nanowire formation was noted in the case of a minute increase in the oxygen level as well as no Ar flow (figure 4.17B). Though the concentration magnitude could not be estimated, the partial pressure of oxygen must be below $3x10^{-5}$ atm obtained from earlier report [12].

(b) The source of silicon originates from the substrate when the metal consumes Si for the alloy formation leaving exposed facets of Si. Also, the initial oxide layer dissociates into silicon monoxide and Si. Presence of SiO vapor aids nanowire growth by supplying both Si and O.

(c) A combination of growth models governs nanowire growth. The presence of metal catalyst at the tip of nanowires, formation of silicide in tandem with the need for Ar suggests vapor liquid solid model. To rule out the solid liquid solid model, the nanowires were mechanically removed and then the substrate was inspected (figure 4.17C) for any silicide nanocluster. The absence of catalyst at the sample surface negates the possibility of SLS model. Also, the formation of a thin oxide layer and role of SiO inducing nanowire growth signifies oxide assisted growth mechanism. A revised growth model has been illustrated in figure 4.18.

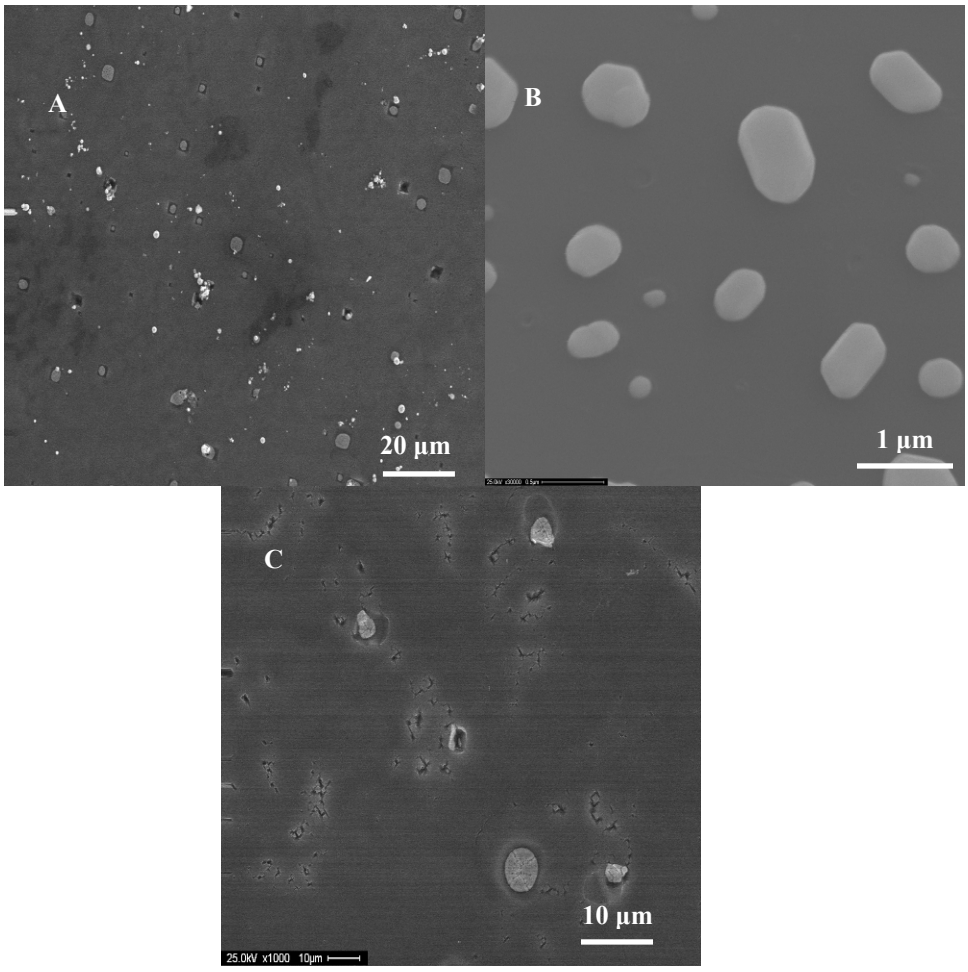

Figure 4.17 SEM Characterization of Pd Coated Si Surface
(A) Absence of nanowire growth after the processed Si substrate was re-heated, (B) Formation of Palladium Nanoclusters in the absence of Ar ambient and (C) Surface devoid of silicide island after mechanical removal of nanowires ruling out the possibility of SLS mechanism

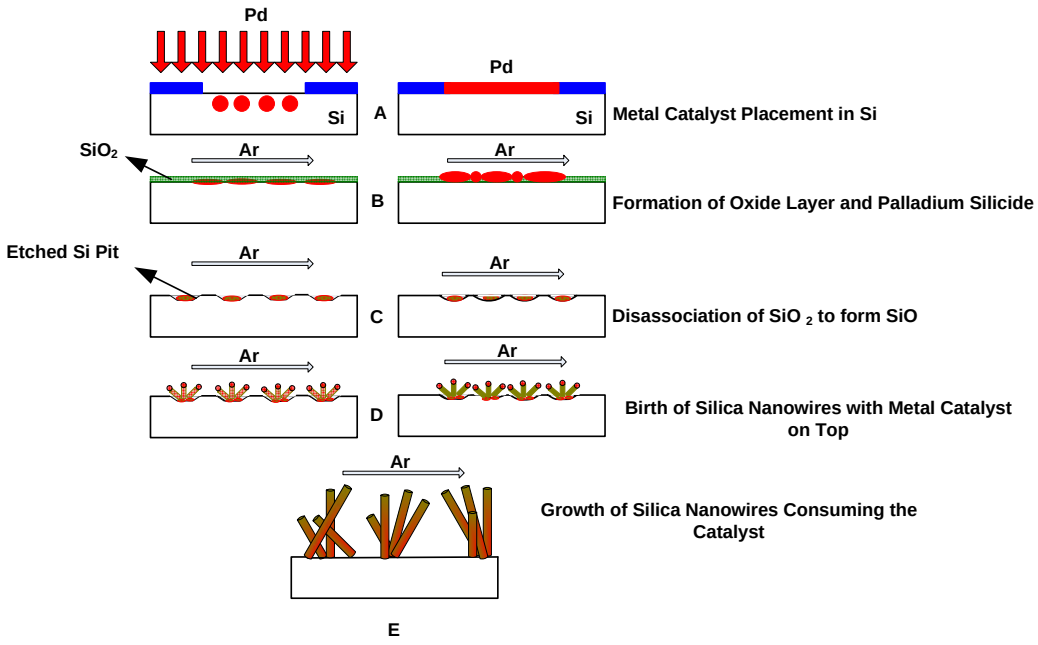

Figure 4.18 Revised Growth Model for Silica Nanowires on Si

(A) Metal Catalyst Placement in Si using ion implantation or sputtered thin film, (B) After sample introduction into furnace – Silicide formation along with a thin oxide layer, (C) Disassociation of oxide layer to form SiO and formation of Si etch pits with increasing heating time, (D) Birth of Silica Nanowires with Metal catalyst on Top and (E) Growth of Silica Nanowires of High Aspect Ratio

4.3.3 Conclusions

In summary, the manufacturing aspect of silica nanowire growth was investigated. Nanowires nucleate following a combination of vapor liquid solid model and oxide assisted growth mechanism. For a given thickness of Pd thin film, the nanowire growth seems to attain steady state after a heating time of 90 mins. It has been observed that the nanowires grow at the expense of the catalyst negating the re-usability for the substrate.

4.4 Metal Decorated Silica Nanowires: An Active SERS Substrate for Cancer Biomarker Detection

Surface-enhanced Raman spectroscopy (SERS) has been the defacto verification technique for multiplexed assay diagnostics with rapid screening. .In general, SER using microRaman spectroscopy offers the combined benefits of high spatial resolution and energy densities, making it a powerful molecular investigation tool with minimal sample volume. The signal enhancement in SERS is a strong function of the shape and size of the dielectric medium and the size of the metallic particles. The enhancement scales inversely with the size of its constituents. Among the various SER architectures, the nanocluster/nanowire configuration has the advantage of being engineered to grow on predetermined sites on a Si substrate, enabling the development of integrated microRaman detection on a chip. In this context, this research section demonstrates the use of Pd ion implantation catalysed silica nanowires as a SER substrate towards the detection of interleukin-10, a cancer biomarker.

4.4.1 Experimental

In the present work we report the use of metal decorated silica nanowires as an effective SERS substrate exemplified by highly sensitive screening of IL-10. IL-10 is a homodimeric protein biomarker often associated with various carcinomas, chronic inflammatory bowel ailment, and many more diseases and hence its detection is very crucial for diagnostic and therapeutic purposes. Nanowires were grown using the ion implanted seeding approach as demonstrated earlier. In brief, palladium (Pd) ions were implanted into Si (100) at 19 keV with a constant dose of 3E16 ions/cm^2. The implanted samples were then annealed at 1100^0 C in Ar ambient for time intervals of 180, 60, 30 and 7 min, respectively. For transmission electron microscopy (TEM) studies, the wires, grown for 60 min, were transferred directly onto the copper grids via ethanol suspension.

4.4.2 Results and Discussion

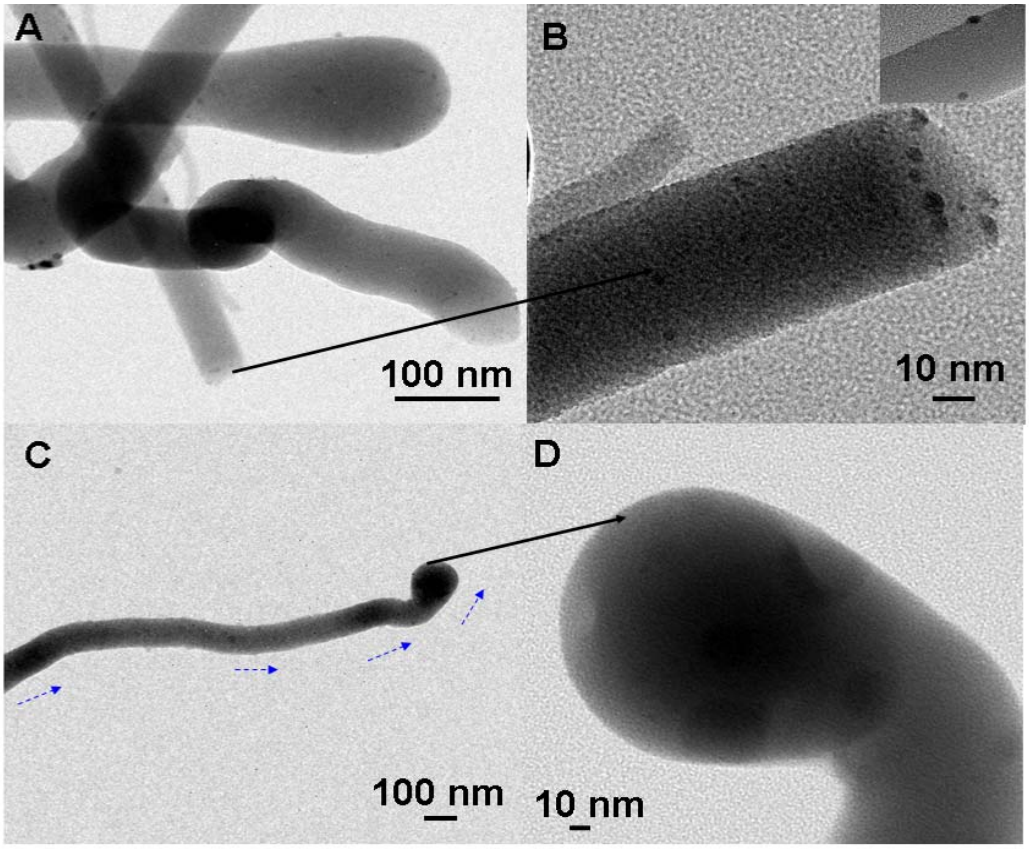

Figure 4.19 High Resolution TEM Micrographs of Metal Decorated Silica Nanowires from the Implanted Regions
(3E16 ions/cm^2, 1100^0 C, 60 min).
(A) Entangled amorphous nanostructures of varying size and high aspect ratio, (B) Higher magnification image clearly indicating the distribution of nanoparticles along the nanowire body and apex, Inset: Snapshot for number density estimation of catalyst particles, (C) Periodic dark regions giving an insight of the migration of catalyst particles highlighted by arrows terminating at the wire tip of higher concentration leading to further nanowire growth on continued heating and (D) Aggregation of nanoparticles near the nanowire tip. (Reproduced with Permission, Sekhar et al., JPC C, 112, 2008)

For transmission electron microscopy (TEM) studies, the wires, grown for 60 min, were transferred directly onto the copper grids via ethanol suspension. High resolution bright field image (figure 4.19A) from the implanted regions reveal entangled nanowires with high aspect ratio. Further investigations of a single strand (figure 4.19B) with higher magnification indicate the presence of metallic nanoclusters (dark) on the apex and along the body (see inset-top right). These clusters average about 6 nm in size and have an estimated density of 3.3×10^{12} particles/cm^2. The number density of the clusters on the wires was estimated by counting the clusters on wires in five 10x10 nm^2 of the TEM, and averaging them. Figure 4.19C shows the migration of these nanoparticles with periodic aggregation leading to dark areas of enhanced contrast. Such a configuration could be attributed to a combination of growth mechanism (VLS/VS) and the available surplus thermal energy for the catalyst to migrate. Initially Pd_2Si acts as catalyst for the initial nucleation of silica nanowires via Vapor-Liquid-Solid (VLS) mechanism. As the nanowires grow, Pd catalyst droplets wet the side wall and eventually get consumed. Figure 4.19D shows the TEM image of the nanowire head with high concentration of metallic nanoclusters.

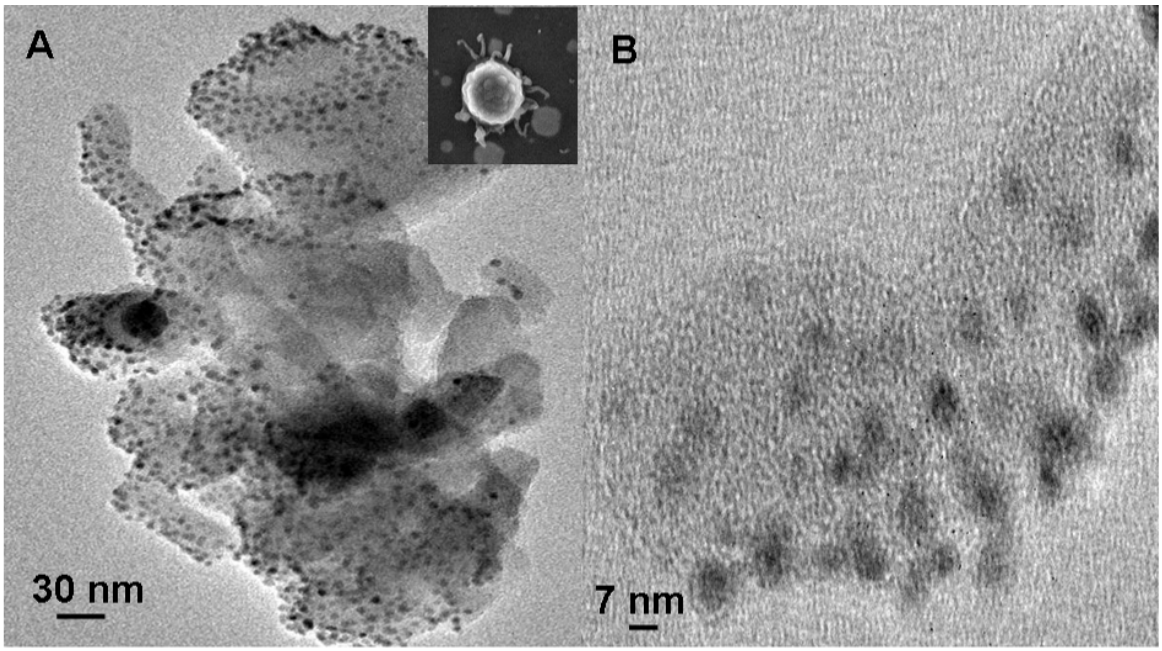

Figure 4.20 Migration of Pd Catalyst Particles Captured at an Early Growth Stage (3E16 ions/cm^2, 1100^0 C, 7 min)
(A) "Birth" of nanowires, nucleated wires of various sizes and shapes concentrated with Pd particles, Inset: Scanning Electron Microscopy (SEM) micrograph highlighting the early growth stage, Ostwald Ripening of the seeds observed and (B) Magnified image of a single nanowire for estimating the number density of the wires: 1x10^{13} particles/cm^2.
(Reproduced with Permission)

Figure 4.20 shows the TEM image indicating the decoration of catalyst nanoparticles along the nanowire at an early growth stage. An energy dispersive spectroscopy (EDS) map in tandem with captured lattice fringe spacing confirms that the clusters formed are of Pd (Appendix B, figure B.1). It also confirms the absence of any silicide along the nanowire. The number density of these metal nanoclusters increased three times when the growth time was reduced from 60 to 7 min. The uneven growth (few wires emerging at this early stage) is attributed to the Ostwald Ripening process along with the continuous consumption towards nanowire growth. In addition, the spatial distribution of the metal particles along nanowire surface seems to be random in nature.

Rutherford Backscattering Spectroscopy (RBS) was also carried out to investigate the stoichiometry of the wires along with the role of Pd in nanowire growth (Appendix B, figure B.2). RBS measurements were performed on samples with incident beam of 2 MeV He ions at a scattering angle of 160^0. Absence of Pd in sample was observed when the heating time for nanowire growth was increased from 60 to 180 min. This depletion suggests diminishing catalyst activity with increase in nanowire length (a function of heating time) [14]. Thus for Pd (atomic radius = 0.14 nm) catalysed nanosystem, the role of Pd stops at a length of 10 μm for an average radius of 50 nm. This indicates that the size dependent catalyst action can be leveraged for site specific growth (with controlled aspect ratio) through implantation based seeding approach. To evaluate the applicability of this metal decorated dielectric nanocomposites (NWs) as an effective SER substrate for biomolecule detection, IL-10 was chosen.

For this detection, the nanowire was functionalized with amine group by soaking it in 2% APTMS in ethanol for 60 min followed by rinsing in ample ethanol for 10 min. A standard "sandwich" assay protocol [15] was then used for the modification of nanowires with IL-10. The protocol involves the following steps: (a) deposition of specific capture antibody (Ab) for IL -10 antigens, over night incubation at 4 ^oC; (b) application of a blocking solution in order to control the non-specific binding, incubation for 2 h; (c) immobilization of IL-10 antigens, by incubation for 2 h ended the immobilization sequence with a rinse in phosphate buffer solution (PBS) (3 x 5 min) after every step. The concentration of IL-10 used for SERS validation was 100 μg/mL.

Raman signals were determined at every step to record the effect of the individual surface modification step on spectral shift. Additionally, to study the role of nanowire architecture in SER signal enhancement, the nanocomposite (1100^0 C, 60 min) was evaluated against both thermally grown SiO_2 (Thermal SiO_2 sub - 500 nm) and Au islands (Au on SiO_2 sub) hosted in silica (500 nm). For Au islands, 150 nm of Au was deposited on SiO_2 substrate and annealed in an Ar ambient at 1100^0 C, for 60 min. This resulted in metallic clusters averaging about 100 nm in diameter. The cluster density for Au was measured to be $3x10^{10}$ particles/cm^2, Au was chosen over Pd in these experiments as it has been demonstrated to show superior Raman sensitivity than Pd [16]. The amorphous texture of the dielectric medium (SiO_2) was maintained in all the cases.

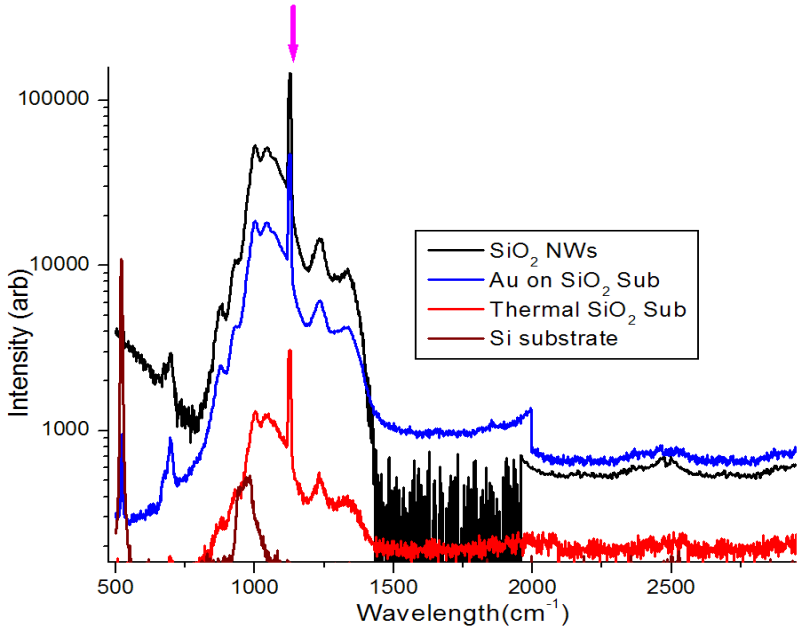

Figure 4.21 MicroRaman Spectroscopy of Plain Substrates as Reference Measurement and Calibration

Si: First order vibration mode at 521 cm^{-1} has been observed, All SiO_2 based samples (800 to 1400 cm^{-1}): Molecular vibrations due to surface phonons in amorphous Silica and SiO_2 nanocomposites (NWs) : Si-O-Si Stretch, Temporal Fluctuation – Non- homogenous morphology, Intensity Ratio at characteristic peak 1123 cm^{-1}, SiO_2: $AuSiO_2$: SiO_2 NWs = 1:15: 42).

Figure 4.21 shows the first order Raman signal of the different substrates. Si appears as a sharp peak at 521.1 cm^{-1}, with a broader outset at around 970 cm^{-1}. This Si substrate was used as a calibration standard. All silica samples exhibit a peak pattern from 864 to 920 cm^{-1} (including 994, 1034, 1123, 1226 cm^{-1}) indicating intrinsic surface phonon activity [17]. In nanocomposites, the characteristic D2 defect mode at around 697 cm^{-1} was also observed in Raman spectrum. This is congruent with the Si-O-Si stretch [18].

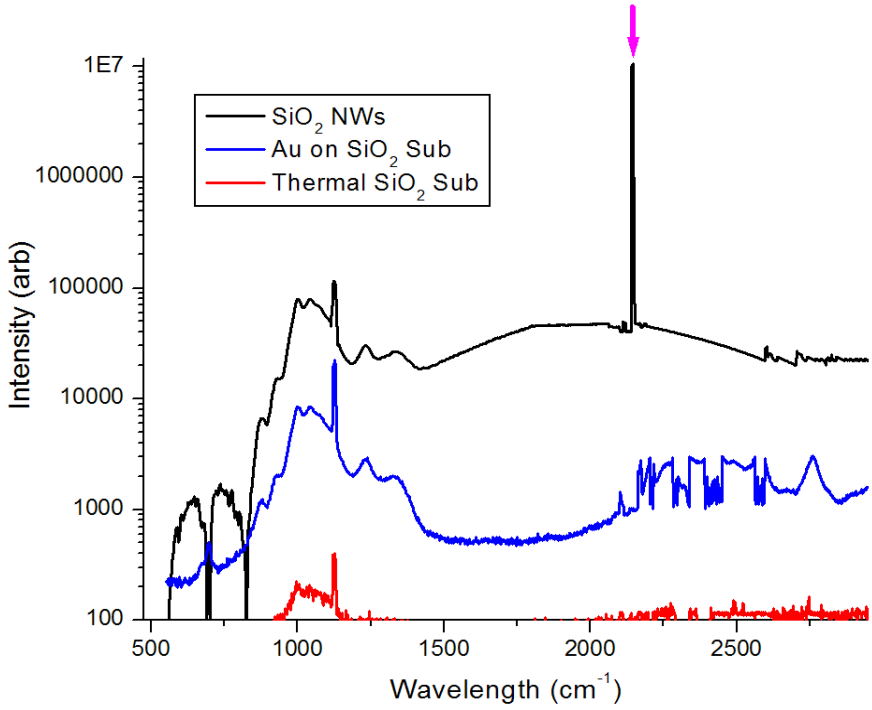

Figure 4.22 MicroRaman Spectroscopy of APTMS Functionalized Substrates SiO_2: Non-reactive with APTMS, degeneration of signal observed from 2200 to 2400 cm^{-1}, $AuSiO_2$: Partial interaction with APTMS, High frequency C-H vibrations seen and SiO_2NWs: Complete reaction with APTMS devoid of high frequency C-H mode. Intensity ratio at characteristic peak 2150 cm^{-1}, $AuSiO_2$: SiO_2 NWs = 1:3614.

Upon functionalization of the samples with APTMS (figure 4.22), degeneration of the Raman signal (2200-2400 cm^{-1}) was observed for thermally grown silica in addition to 2738 cm^{-1} peak. Reaction of Au nanoparticles on oxide with APTMS resulted in a peak around 2748 cm^{-1} with intensity magnitude of 2617. These spectral signatures resemble high frequency C-H vibrations suggesting incomplete reaction of the substrate with the silane compound. Whereas, the Stokes lines emerging from 2150 cm^{-1} (N-H stretch) recorded on Au loaded silica and nanocomposite seems to be a resultant of complete participation of substrates with the bidentate APTMS molecules.

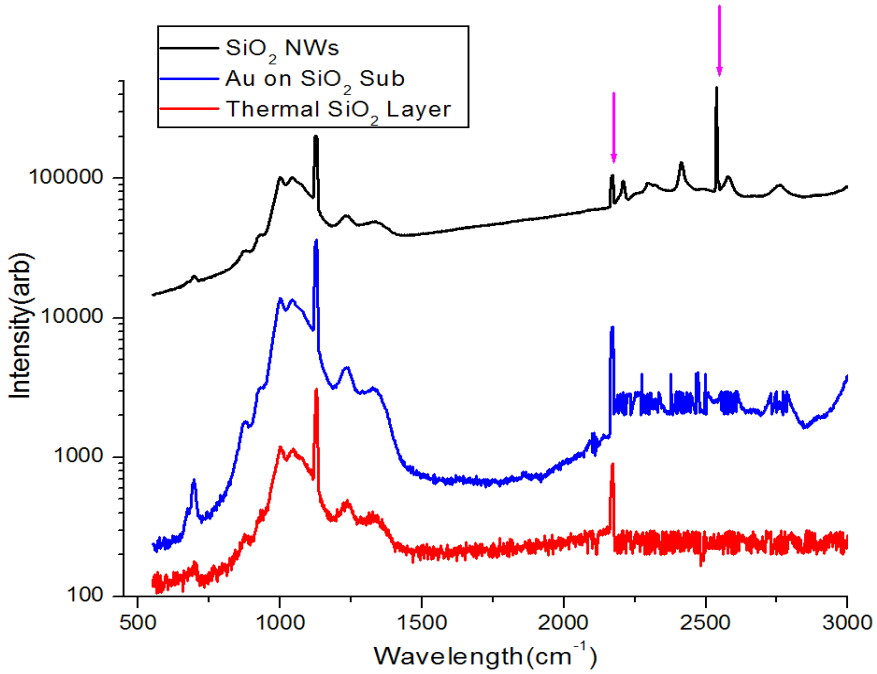

Figure 4.23 MicroRaman Spectroscopy of Immobilized Capture Antibody on Various Substrates SiO_2, $AuSiO_2$ (2160 cm^{-1}): Suggest binding deficiency- Unreacted Abs and SiO_2NWs (Group Frequencies: 2000-2600 cm^{-1}) – Suggest Better Ab Immobilization.

Upon immobilization of the antibodies on all samples, a curtailed Ab-APTMS association (figure 4.23) for both plain and Au coated silica could be observed at 2160 cm^{-1}. Temporal fluctuations from 2300 to 2800 cm^{-1} in the latter could be attributed to uneven distribution of Au particles. The antibodies confined to the inter-particle space seem to bring in coupling effects from local surface plasmons translated as noise pattern in the spectrum. These spectrum results suggest the binding deficiency of plain and Au coated silica sample in the immunoassay. Moreover, the signature group frequencies from 2000 to 2500 cm^{-1} arising from the nanocomposites can be attributed to interfacial behaviour coupled with charge transfer associated with the antibodies.

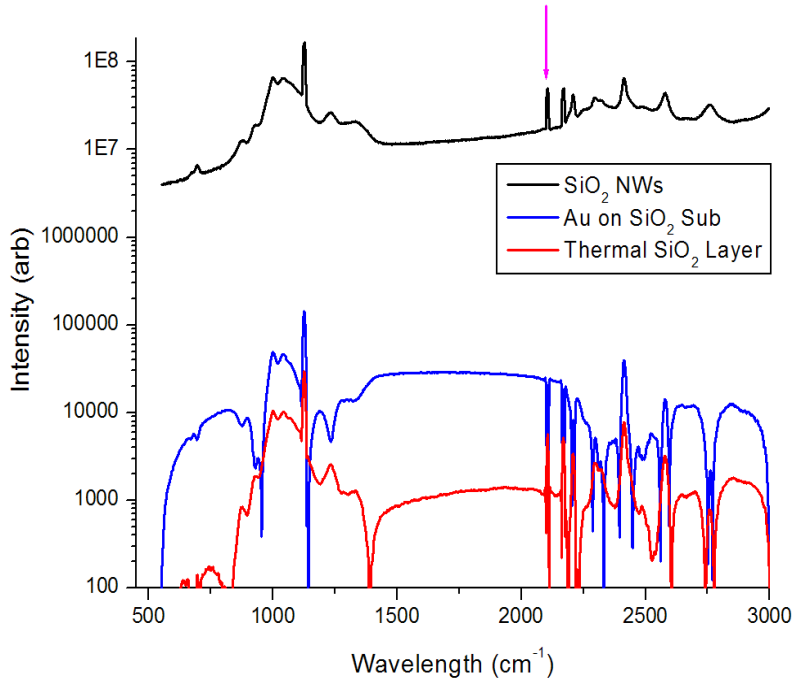

Figure 4.24 MicroRaman Spectroscopy Targeting IL-10 Detection on Various Substrates SiO_2, $AuSiO_2$ (2000 to 2500 cm^{-1}) : Photoinduced desorption of the adsorbates and SiO_2NWs: Characteristic IL-10 signature identified around 2105 cm^{-1} with an intensity of 10^7 in comparison with other substrates.

Finally, the characteristic vibrational footprint of IL-10 attachment was identified by comparing the Raman spectra (figure 4.24) of the layers forming the sandwich assay. Observed instability in the Raman for bare and Au coated silica suggests photoinduced desorption of adsorbates due to a weaker conjugate attachment. Such noisy behaviour has been attributed to the movement of the molecules in and out of the dielectric region surrounded by metal particles [19]. However, high frequency traces of APTMS-Ab interaction were still found to exist. In nanocomposite samples, a distinct sharp peak was noticed around 2105 cm^{-1} indicating IL-10 binding to form a complex moiety. The microRaman spectrum indicating IL-10 attachment was repeatable for different nanowire samples synthesized under similar experimental condition. A variation of 6 wavenumbers was observed around 2105 cm^{-1} for all the runs.

The approach in calculating the enhancement factor or intensity was similar to A.D McFarland et al. [20]. Enhancement factor was calculated as:

$$EF = (N_{sub} x I_{wires}) / (N_{wires} x I_{sub}) \quad \text{.....(4.1)}$$

Where,

N_{sub}, N_{wires} – Number of molecules probed on the SiO_2 substrate and wires respectively,

I_{sub}, I_{wires} – Raman intensity of the characteristic peak from the SiO_2 substrate and SiO_2 wires respectively. (The normalized enhancement factor is further calculated by assuming $I_{sub} = 1$)

During the functionalization stage, nearly four orders of increase were observed in the metal decorated nanowire sample in comparison with Au metal colloids in silica. A better binding chemistry of these nanoscale wires subsequently results in five fold augment in screening the antibody over other substrates. This in turn led to an overall structural enhancement of 10^7 (Table 4.2) in contrast to thermally grown silica towards IL-10 detection. It is interesting to note that this nanowire based SER configuration separates the plasmon phenomenon of the adsorbate molecules from the electronic resonances of the substrate.

Table 4.2 Comparison of the Enhancement Factor for Substrate Evaluation

Substrate	**Normalized Enhancement Factor (Thermal SiO_2 = 1) at Characteristic Vibrating Frequency**			
	Without Treatment	APTMS	Ab	IL-10
Au on SiO_2	15.4	2.7E3	5.2	-
SiO_2 NWs	42.0	1.0E7	116.2	4.7E7

As a measure of selectivity, the Raman spectrum of the assay using PBS (instead of IL-10) was recorded (Appendix B, figure B.3) which indicates the absence of any activity around 2100 cm^{-1}(devoid of IL footprint). The electronic resonances of the substrate were only observed. Further, to evaluate non-specific binding, IL-10 was attached to functionalized SiO_2 NWs in the absence of capture antibody. The Raman spectrum (appendix B, figure B.4) indicates the dominant signature of amine functionality at 2150 cm^{-1}. Absence of IL-10 foot print around 2100 cm^{-1} suggests the inactive participation of IL-10 in the assay.

In addition, both the concentrations of capture antibodies and IL-10 were varied (100 µg/mL to 0.1 ng/mL to estimate the detection limits of the current scheme. Figure 4.25 schematically illustrates the dependence of SER intensity on the concentration of the species. The relationship was found to be exponential in nature through a linear transformation and fit. A SER intensity of 10^3 was recorded for the lowest concentration of IL-10 suggesting a reliable detection limit of 0.1 ng/mL.

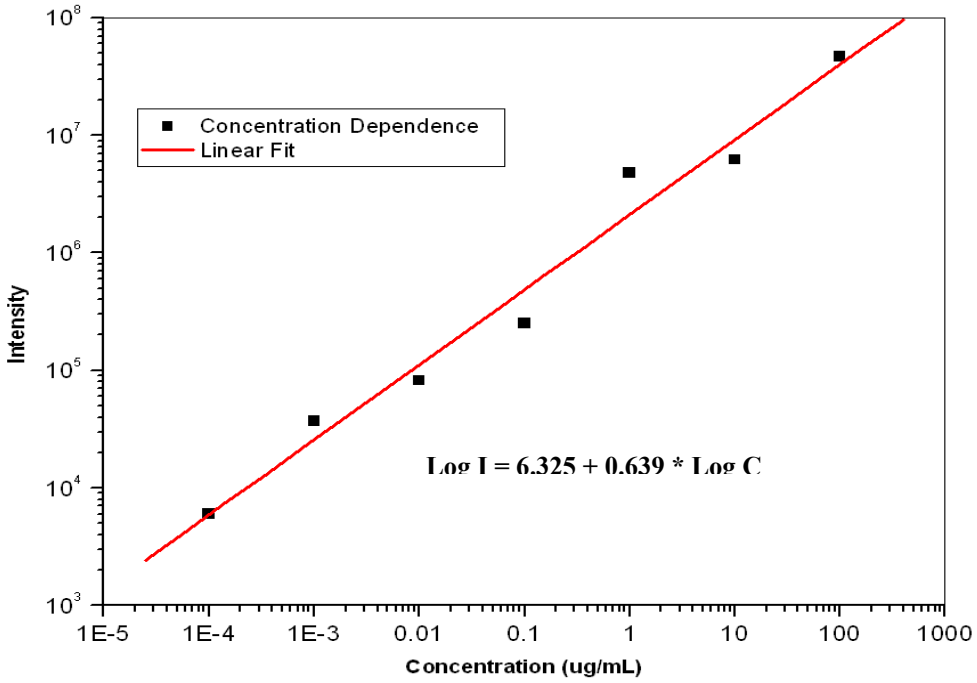

Figure 4.25 SER Intensity Variation for Different Concentrations (from 100 µg/mL to 0.1 ng/mL) of IL-10 and Capture Antibodies

These results collectively suggest the SiO_2 NWs as an effective SERS platform for sensitive detection of IL-10 molecules with good resolution. The observed enhancement is also supported by theoretical estimate of electronic polarizability per volume of 0.4 and plasmonic dispersion magnitude of 0.31 (for $\lambda = 514.5$ nm) for the Pd/SiO_2 NWs. In addition, it is hypothesized that the size of the metal nanoparticles induces quantum size effects that aids in addition to the classical electromagnetic enhancement as reported earlier [21].

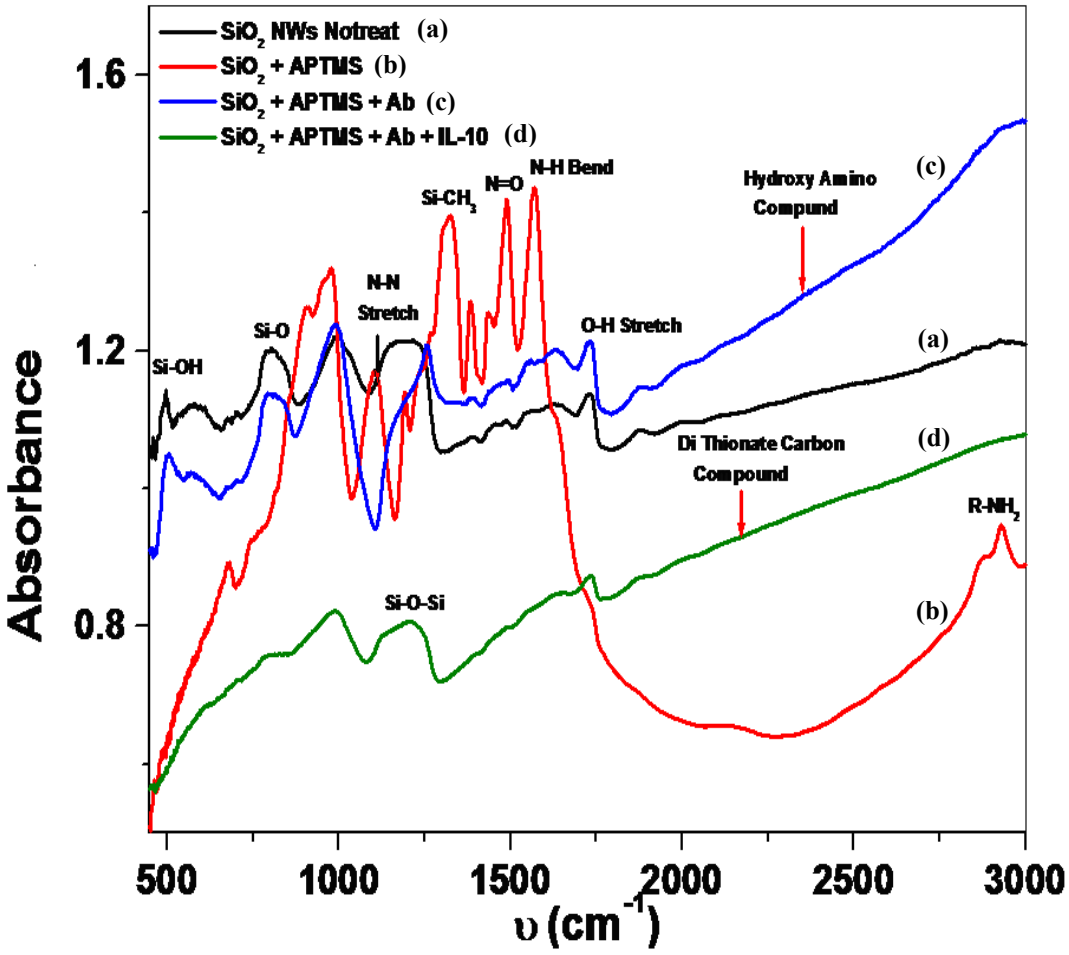

Figure 4.26 Fourier Transform Infra-Red (FTIR) Absorption Spectra of SiO_2 Nanowires (Complimentary results to MicroRaman spectroscopy)

IR characteristics indicate good binding chemistry of NWs with APTMS – formation of functional groups. Active participation of NWs in the assay – decrease in absorbance magnitude for Ab binding and IL-10 coupling.

Moreover, engineered SER materials exhibit varied response to chemical treatments, which is strictly a function of the substrate preparation techniques. Molecular dipole moment induced infra-red (IR) characteristics verifying the chemical affinity of these nanocomposites in the assay was obtained over a range of frequency (400-3000 cm^{-1}) with a resolution of 0.4 cm^{-1}.

The sample was inspected under the Perkin Elmer FTIR spectrometer (after every routine of Raman) for the complimentary infrared absorption using a sealed and desiccated optical module. Raman results before chemical treatment are validated by the partial Si-O stretch (figure 4.26) observed in the FTIR spectra. Pd loaded silica nanowires functionalized with APTMS exhibited a sharp CH_2 rocking mode around 940 cm^{-1}. Moreover, the silane interaction with the nanowires exhibit N-N, N-H and N=O functional groups.

The spectrum results give an insight to the degree of binding with complete participation of the wires in the chemical treatment. Further, formation of a complex hydroxyl amino compound structure was noticed upon antibody immobilization with a decrease in absorbance magnitude. Coupling of IL-10 antigen-antibody event has been characterized by further decrease in absorbance and the formation of poly carbon compound structure resembling a protein moiety (long chain amino terminated bonds). Thus, the easily synthesizable SiO_2 nanoarchitecture offers large active (chemical) sites for molecular interaction that could result in high through put screening.

4.4.3 Conclusions

In summary, controlling annealing kinetics of ion implantation seeded silica nanowires resulted in the evolution of the SER medium on Si, in a single heat treatment. This metallic nanocluster/dielectric nanowire composite serves as an active SER substrate exhibiting a sensitivity of 10^7 towards micromolar detection of IL-10, with high spatial resolution. The configuration also separates the plasmon phenomenon of the adsorbate molecules from the electronic resonances of the substrate. Metal decorated silica nanowire architecture holds a great potential for a wide variety of applications.

This stems from the fact that the ion implantation process catalyzing nanowire growth ensures isotopic purity level of the nanoclusters for which any metal across the periodic table can be used. Addition of other coinage metal nanocolloids in the host matrix via co-implantation would pave the way for composite resonant particles for multiplexed detection. Specifically, Au, Ag and Cu catalysed silica nanowires would be an interesting set of plasmonic materials for large SER enhancement with high spatial resolution.

These modifications impart the tunablility for SER action. Moreover, site specific growth on Si enables integrated plasmon optical circuits. Such a configuration on Si would enable a multi-modal sensing platform for lab-on-a-chip (LoC) applications targeting accurate biodiagnostics. A critical application of this engineered surface would be to sensitize the optical activity of Erbium (Er) which could revolutionize the telecommunication industry.

4.5 Selective Growth of Silica Nanowires Using Au Catalyst for Optical Recognition of Interleukin-10

The low optical activity (photoluminescence efficiency) and inherent semiconducting properties of the Si substrate limit the optical and electrochemical based sensing applications of SiO_2 nanowires. Moreover, investigations on selective growth of SiO_2 nanowires on substrates such as SiO_2, alumina and plastics have been limited. In the present report, we report selective synthesis of SiO_2 nanowires on Au-patterned electrodes on silica substrate via the VLS mechanism.

4.5.1 Experimental

Silica nanowires were synthesized on Si substrate using VLS mechanism as mentioned in earlier sections. In brief prime grade Si (100) wafers were first cleaned using a standard Radio Corporation of America (RCA) protocol. A fresh oxide layer of 3000 Å was deposited by dry oxidation. The patterning of Au on Si wafers was accomplished using photolithography, subsequent e-beam evaporation followed by metal lift-off. Subsequently, the Au patterned Si wafers diced into 12 x 12 mm^2 area, were kept on a blank Si-wafer (2.54 cm^2) and heated in the open ended quartz tube furnace (MB 71 Mini Brute Tube furnace 4 inch, Thermo products, CA) with Ar as a carrier gas (flow rate 30 sccm). The blank Si wafer was used as a source for producing Si vapor. The nanowire growth was done in three steps; initially the furnace was ramped to 1100^0 C in the presence of Ar ambient and then the sample was introduced and heated for 1 h, followed by natural cooling to room temperature.

4.5.2 Results and Discussion

Figure 4.27 (a) and (b) show the SEM micrograph of as-grown nanowires on the patterned SiO_2/Si wafer and figures 4.27 (c) and (d) represent the optical microscope images. The selective growth has been illustrated in Figure 4.27(a). Absence of nanowire growth in regions devoid of Au highlights the role of Au as a catalyst. A higher magnification view (inset, figure 4.26 (a)) of the protruding nanowires out of the electrodes indicate an average diameter of 200 nm with an aspect ratio (length to diameter) of ~500. Such high aspect ratio structures are required for sensing due to the enhanced reactive sites at the surface for the desired chemical reaction [26]. Figure 4.27 (b) shows pit formation on the oxide layer and the presence of large aggregates from which nanowires seems to originate.

The occurrence of pits can be attributed to partial etching of the oxide layer at a high temperature and low partial pressure of oxygen in an open tube furnace. Such a model of surface etching and subsequent catalysed nanowire growth has been previously observed [24]. It is interesting to note the behavior of some nanowires acting as interconnects between the electrodes. Nanowires are found to emanate from the surface at very acute angles.

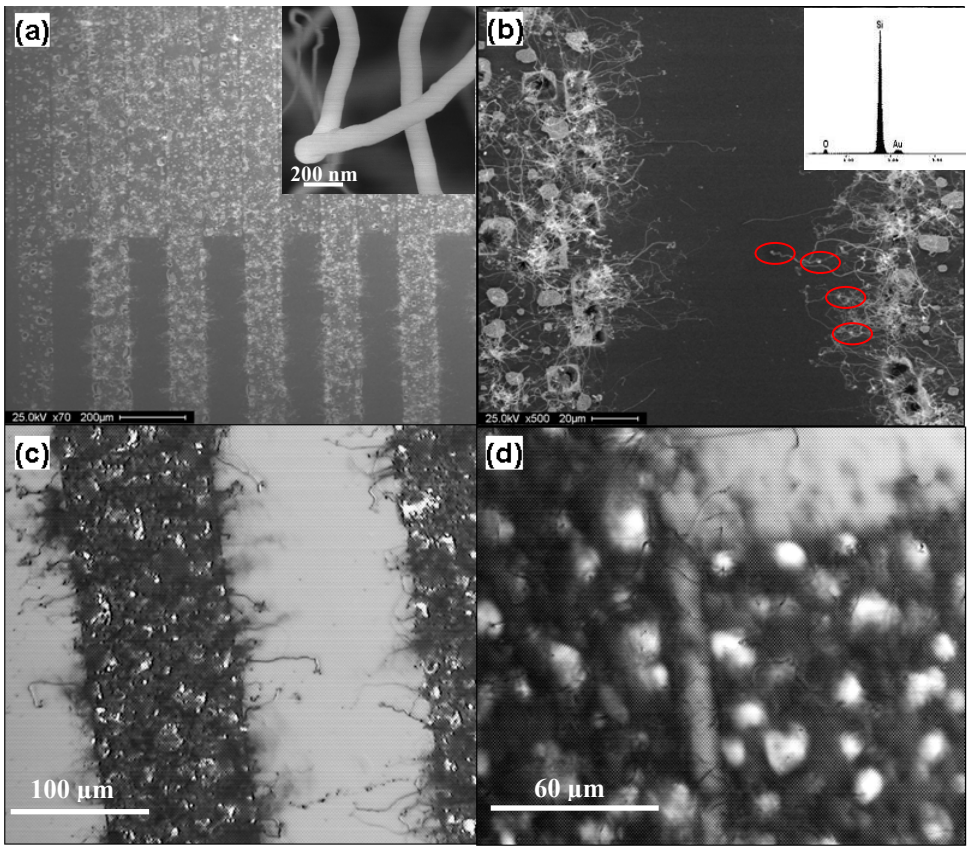

Figure 4.27 SEM Images of the Synthesized Nanowires (1100^0C, 60 mins, Ar) on the Si Wafer Containing Patterned Interdigitated Au Electrodes

(Reproduced with Permission, Sekhar et al., Nanotechnology, 19, 2008)

(a) Selective growth of nanowires on Au interdigitated electrodes, inset: Size of the nanowires, average diameter: 200 nm, aspect ratio > 500, (b) Nanowires emanating from the pit in the presence of large crystallites, inset: Low Energy EDS on the tip of the nanowires reveal an elemental composition Si, O and Au., (c) and (d) low magnification optical microscopy images showing the localized growth of nanowires with Au clusters appearing as bright whitish spots and dense intertwined nanowires.

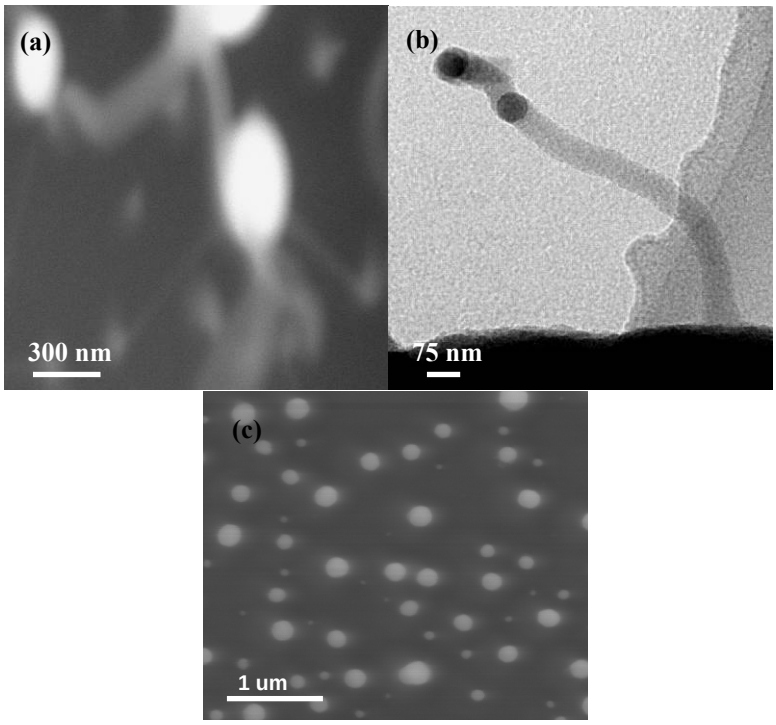

Figure 4.28 Evidence of VLS Mechanism

(a) Back Scattered SEM image showing significant contrast at the tip of the nanowire indicating the presence of metal (Au), (b) Bright Field TEM Image also confirming the migration of Au nanoparticles and (c) High magnification SEM image of the sample heated to 1100 C in the absence of support wafer (Si vapor source) and presence of Ar. Surface morphology devoid of nanowire growth confirms the VLS growth technique.

(Reproduced with Permission)

Figure 4.28 supports the claim of VLS mediated nanowire growth in the present study. Back scattered SEM image (figure 4.28 (a)) shows a significant contrast in the nanowire body and the tip. This atomic number differential suggests the presence of metal catalyst (Au) on the nanowire tip. Further, the migration of metal catalyst along the body of the nanowire has been observed in the bright field TEM image (figure 4.28 (b)). Figure 4.28 (c) is an SEM image of a sample for nanowire growth in the absence of the support wafer (Si vapor source) heated to 1100^0 C for an hour in the presence of Ar. The observed surface morphology devoid of nanowire growth confirms the VLS mechanism.

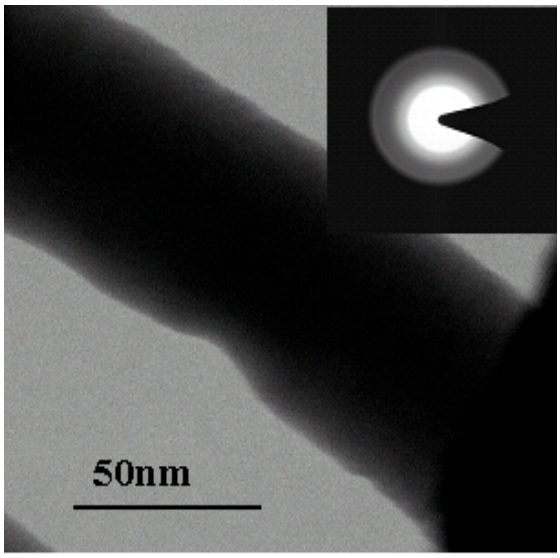

Figure 4.29 Bright Field TEM Image Indicating Amorphous Texture of the Nanowire
A differential structural contrast could be seen suggesting core-shell nanowire architecture.

The TEM image shown in figure 4.29 of a single nanowire of diameter 60 nm shows smooth morphology with differential contrast on the inner and outer surfaces. Such architecture possibly suggests a core (Si) – shell (SiO_2) configuration of the nanowire. Selected area diffraction calculations were carried using the equation:

$$d_{hkl} = L_{norm}\lambda / R \quad \text{.....(4.2)}$$

Where,

$L_{Normalized}$ is the Camera Length =1000 nm,

λ is the wavelength of electron = 0.28 nm, and

R – Ring Radius from the diffraction pattern.

The calculated d value of 0.330 nm is very close to the theoretical d value of 0.335nm, assigned for amorphous SiO_2. The selected area diffraction image reveals the amorphous texture of the nanowires.

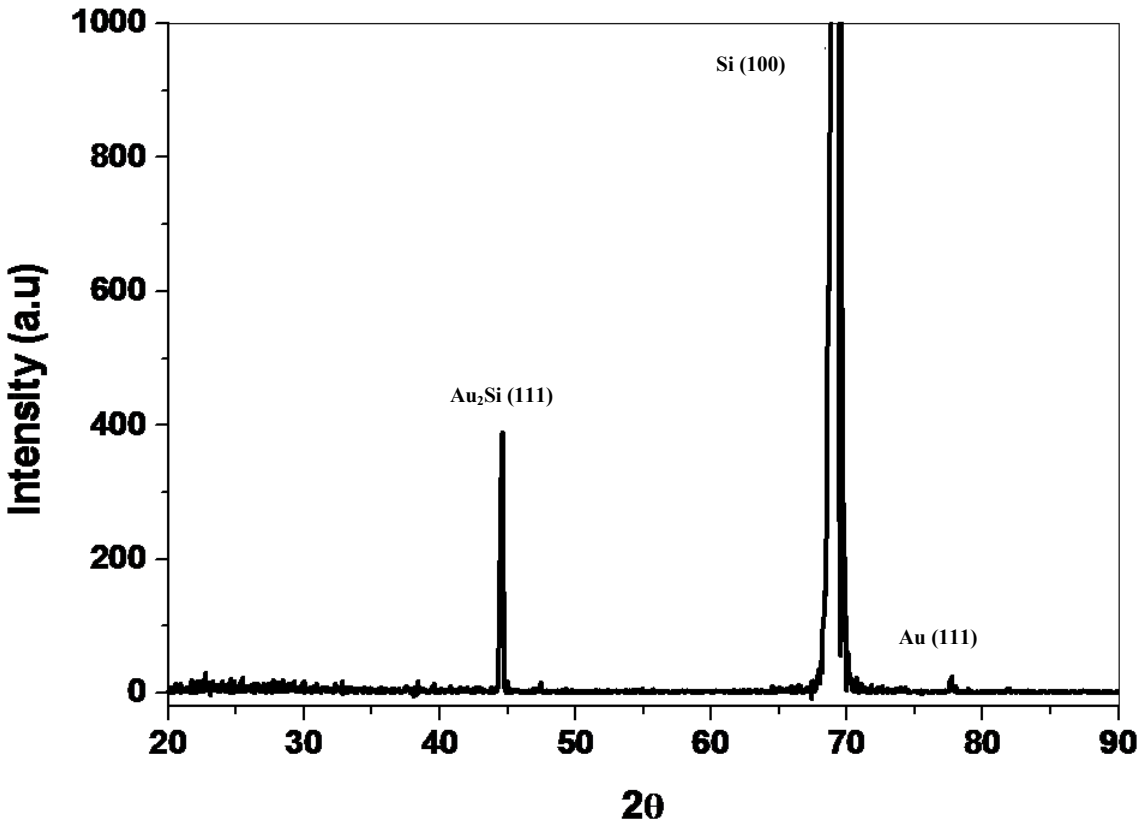

Figure 4.30 XRD Image of the Nanowire Sample
Illustrating the Formation of Au Silicide along with the Presence of Metallic Gold while Confirming the Amorphous Texture of Nanowires

Further, XRD (figure 4.30) reveals the possibility of gold silicide formation, which act as parent nanoclusters for nanowire growth. A peak at 44.5^0 corresponding to the Au-Si alloy in congruent with the silicide stoichiometry outlined in the Au–Si phase diagram under similar experimental conditions. Also, the amorphous nature of these nanowires is confirmed by the absence of crystalline peak in XRD at 32^0.

After exploring morphological characteristics, the nanowires were functionalized with APTMS and then immobilized with interleukin-10 according to the scheme shown in figure 4.31. Figure 4.32 shows the fluorescent images of functionalized SiO_2 substrate and SiO_2 NWs surface after attaching the detector antibody tagged to fluorescent QD-655.

The concentrations of capture antibody and IL-10 antigens used for the measurement were 1 mg/mL, 500 µg/mL, 250 µg/mL and 100 µg/ml.

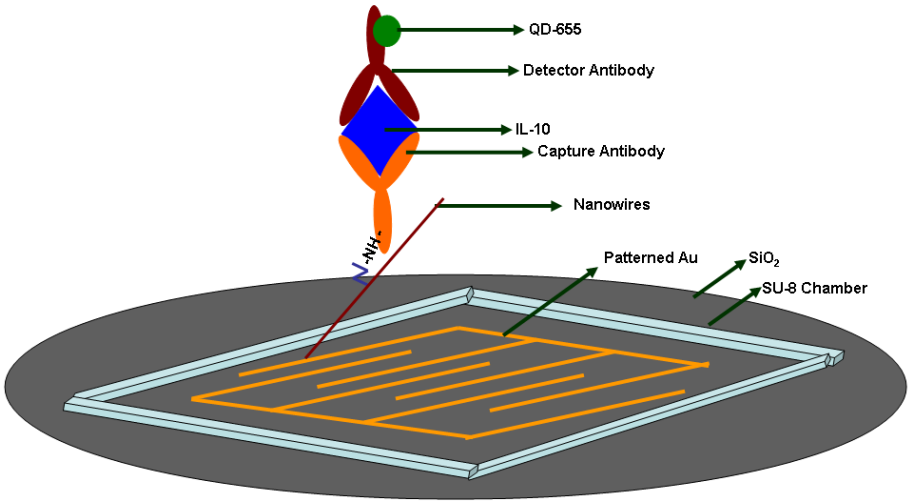

Figure 4.31 Illustration of the Assay Protocol Using Nanowire as a Template

Strong and sharp florescence was observed in the nanowire sample at an excitation of just 300 ms (figure 4.32). However, for SiO_2 substrate with patterned Au electrode, an excitation of 3500 ms (figure 4.32 A1), was required to barely identify the reaction. No significant binding could be optically observed on the Au-patterned sample as compared to that of SiO_2 NWs at the same excitation level. It has been demonstrated earlier that the role of the Si and Au regions in the binding chemistry with APTMS and assay protocol is insignificant.

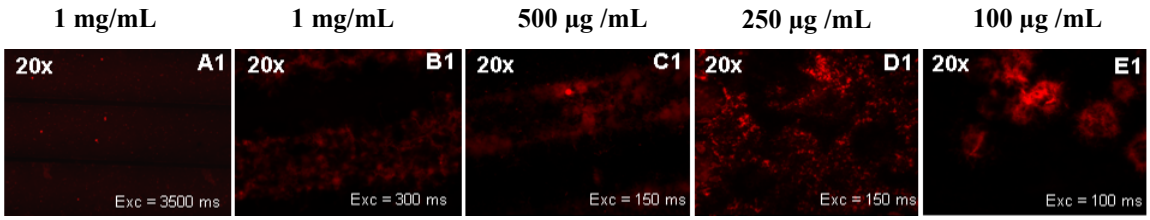

A1 – Immunoassay on Plain Au Interdigitated Electrodes
B1, C1, D1, E1 – Immunoassay on Nanowires Synthesized on Au Interdigitated Electrodes

Figure 4.32 Optical Fluorescent Images for Estimating the Optical Response to Varying Concentrations of IL-10

The time taken for the features to appear/fluoresce after input excitation from the microscope normalized to the magnification is referred as the optical response. To observe the effectiveness of using silica nanowires as template, the time taken for the assay to appear both on functionalized plain electrodes and nanostructured platform had been recorded. In particular, the optical response to varying concentrations of IL-10 using the nanowire template has been tabulated. Comparison of the optical response (ratio of excitation time to lens objective) upon IL-10 attachment has been shown in table 4.3.

It can be inferred from the table that the different optical response obtained from fluorescent images indicate a ten fold improvement upon using silica nanowires as template when compared to silica substrate. The fluorescence intensity appears to inversely vary with the species concentration. Sample assayed with minimal concentration (100 µg/mL) shows higher intensity than the rest of the volume.

Table 4.3 Comparison of Optical Response (Ratio of Excitation Time to Objective) upon IL-10 Attachment

Sample No	**Concentration (µg/mL)**	**Optical Response (ms)**
A1	1000	175
B1	1000	15
C1	500	7.5
D1	250	7.5
E1	100	5

The fact that immobilized molecules diffuse randomly in all three dimensions within the sample volume of wires and the low probability of them passing through the center of focus, each time they become visible, explains the observed behavior. Specific brightness or intensity is a function of molecular absorption cross section and the fluorescence quantum yield. Though researchers usually expect that the images with the more target proteins show stronger fluorescent intensity, the argument does not hold good for all the immunoassay systems and templates.

Such a phenomenon dealing with fluorescence–intensity distribution analysis has been reported by Kask et.al [25]. In optical sensing, the performance of the sensor depends on the nanowire diameter. Thinner wire is much more sensitive to the surroundings than the thick one providing much higher fraction of evanescent waves critical in biosensing applications [26]. Further, scaling down the wire diameter and light wavelength simultaneously enhances the sensitivity of the nanowire sensor. In addition, high aspect ratio nanostructures (long wires) are often preferred for biosensing applications to increase the probability of binding events. Hence, for increased sensitivity, nanowires of thinner diameter and increased length configuration are often preferred. It is possible to synthesize silica nanowires of smaller diameter by this thin film based catalysis by reducing the thickness of the Au catalyst and growth temperature of the nanowires. Reducing the thickness of the catalyst results in smaller nucleation sites (parent nanoclusters). The ability to control the size of silica nanowires (grown via VLS mechanism) for specific applications makes them a potential candidate in developing multi-modal sensing platform.

As an orthogonal verification measure, the active participation of the nanowires in the immunoassay has been shown using photoluminescence (PL) behavior. Upon observing the PL spectrum, a quenching in the intensity and shift in peak was indicative after every step in the immunoassay. Figure 4.33 shows the PL plot recorded at different stages of functionalization of SiO_2 -NW prior to fluorescence measurements. A broad peak that can be deconvulated into two peaks around 2.71 and 3.4 eV, corresponding to defect mediated radiative transition and self-trapped excitons in amorphous silica nanowires was observed. Interestingly, after modifying the nanowires surface with APTMS a quenching in the PL intensity was observed, which extends with further modification/application of capture antibody, IL-10 antigen, detector antibody and quantum dots.

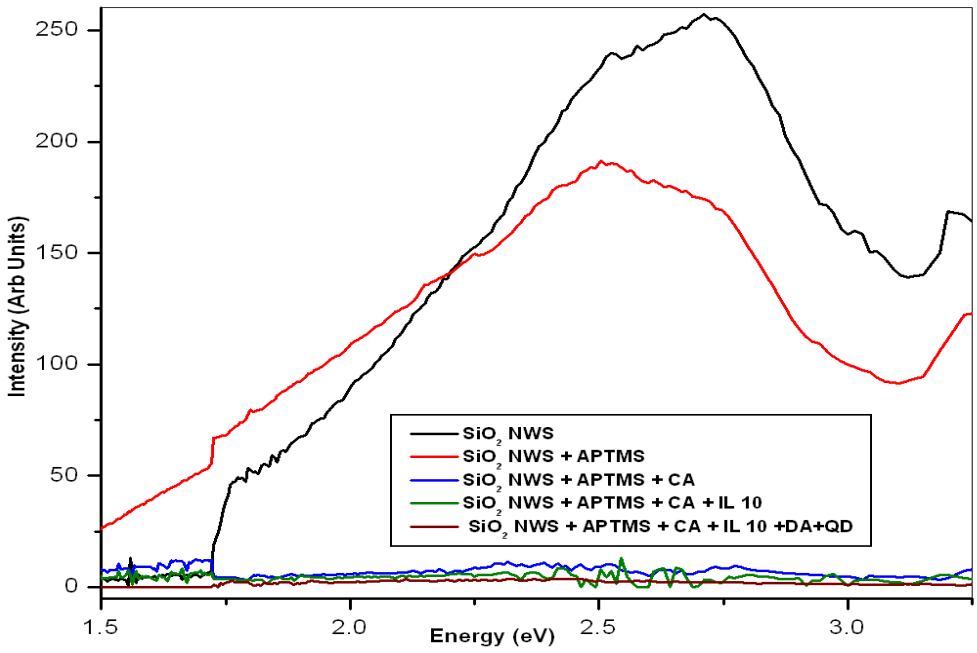

Figure 4.33 Photoluminescence Spectrum Recorded at Every Step of the Immunoassay for IL-10 Detection

A shift in energy peak and reduction in PL intensity was observed after functionalization and attachment on SiO_2 NWs prior to fluorescence measurements.

A quantitative summary of the results indicating the changes in PL attributes (intensity and shift) has been shown in Table 4.4. These results suggest that under minor structural variation on the nanowires, the PL changes dramatically. Although the silica nanowires are fully oxidized, but the presence of structural defects can not be ruled our completely. These structural defects act as recombination centers for the observed PL bands. However, the reduction of PL intensity by two orders of magnitude suggests the domination of de-excitation of self-trapped excitons as suggested by Glinka et.al [27].

Table 4.4 Summary of the PL Behavior after Every Step in the Immunoassay

Sample Condition	**PL Peak (eV)**	**Intensity (arb.units)**
SiO_2 NWs	2.71	252
SiO_2 NWs + APTMS	2.5	183
SiO_2 NWs + APTMS+CA	2.48	11
SiO_2 NWs + APTMS+CA + IL	2.42	9
SiO_2 NWs + APTMS+CA+IL DA + QD	2.3	3

4.5.3 Conclusions

Summarizing, SiO_2 nanowires appear as a promising template for the optical detection of IL-10 as demonstrated. Leveraging their large surface to volume ratio and chemical affinity to silane compounds, they could be used as an immunoassay template for electrochemical detection. In addition, the use of Au, Ag, Cu and Pd as catalyst for nanowire growth paves the way for plasmonic sensing applications. Combining such possibilities, the nanostructured platform could enable a multi-modal sensing scheme for orthogonal validation required for accurate diagnostics.

4.6 Voltammetric Detection of Interleukin-10 in Serum Using Silica Nanowires

The high surface to volume ratio, coupled with the larger density of defect states on the nanomaterials, makes them highly sensitive to minor surface perturbations (i.e., binding chemistry). This could result in a sensor with a high degree of selectivity and sensitivity and a unique chemical signature. Among the one-dimensional nanoentities, silica nanowires (SiO_2-NWs) have been widely studied because of their unique anisotropy in physical, optical, electronic properties with excellent photoluminescence and biocompatability. Moreover, the nanowires' surface can be easily and effectively modified with the well-known chemistry of Si, thereby allowing the creation of a label-free platform for more sensitive detection of marker level. In the present work, the applicability of the SiO_2 nanowires as an effective template in the enzyme immunoassay for voltammetric (electrochemical) detection of two potential lung cancer biomarkers has been demonstrated.

4.6.1 Experimental

In this work, the preclinical blood (plasma) specimens were collected from participants in the lung cancer (helical screening) clinical trials (CT) at the Moffitt Cancer Center. The detection of IL-10 from the one of these samples was accomplished through enzyme based electrochemical recognition using functionalized and localized SiO_2-NWs. The nanowires were grown on Si wafer via Pt thin film catalysis via the VLS mechanism reported in earlier sections. Figure 4.34 shows the microelectrode cell and the testing protocol used for the present study. For detection, Au microelectrodes based electrochemical cell was fabricated on oxidized Si-wafer using standard lithography and lift-off techniques.

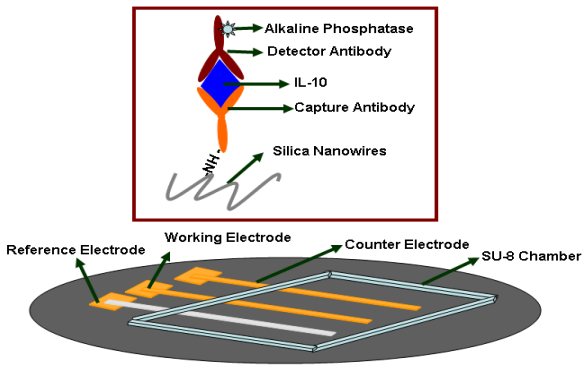

Figure 4.34 Illustration of Nanowire Surface Modification Protocol and the Electrochemical Cell (Reproduced with Permission, Ramgir et al., JPC C, 111, 2007)

Microelectrodes are uniquely suited for probing electrochemical systems as at moderate scan rates, non planar diffusion between the electrodes gives rise to steady state currents. Such amplification of the limiting current has been employed for improving the lower detection limit. Moreover, the product p-nitrophenol (pNP) of the enzymatic reaction, between the Alkaline Phosphatase (ALP) and the p-nitrophenyl phosphate (pNPP) substrate is electroactive and highly stable at room temperature. Furthermore, it can be easily detected by electrochemical reduction of its aromatic nitro group or by oxidation of its aromatic hydroxyl group. The nature of this reaction could be exploited for realizing highly sensitive voltammetric detection using Au microelectrodes.

A standard "sandwich" immunodetection methodology optimized in previous studies on development of protein microarrays was used. The assay exhibited a high specificity towards IL-10 having no cross reactivity with other proteins. The substrates with patterned nanowires were transferred into a glass vial containing 2% solution of APTMS in ethanol. APTMS precipitates onto silica substrates generating a high concentration of reactive primary amine groups that are evenly distributed across the surface. For this, the wires were soaked in the aliquot for an hour and then rinsed with ample ethanol for 5 min. After immobilizing the functionalized nanowires with the capture antibody and IL-10 antigen, streptavidin coated alkaline phosphatise was attached and then incubation for 30 min at room temperature. Finally, 30 µL of (pNPP) solution was added to the chamber and the enzymatic reaction was allowed to proceed for 60 min in dark at RT under humid conditions. The reaction was stopped by adding of 50 µL of PBS stopping solution. The stopping solution results in the change of pH and adds a high concentration of phosphates (an alkaline phosphatase inhibitor) enough to stop the reaction. The product of the reaction pNP was then collected in a vial and used for electrochemistry.

ALP hydrolyzes (dephosphorylates) the substrate pNPP to yellow, water-soluble product pNP with a characteristic absorbance at 405 nm. Electrooxidation of pNP is reported to be a diffusion controlled process and usually occurs at a higher potential between 0.7 to 1.2 V depending upon the electrodes and its configuration.

4.6.2 Results and Discussion

Figure 4.35 shows the voltammograms recorded for the reaction product pNP (3 μL) collected with incubation time of 20 min for different concentration of IL-10 antigen in pH 9 tris buffer solution. As can be seen pNP underwent an irreversible oxidation at 0.85 V when a potential scan from 0.4 to 1.0 V (vs. Ag pseudo reference) at a scan rate of 50 mV is applied. The anodic peak current was decreasing with decrease in IL-10 concentration. Oxidation of phenolic compounds often results in surface passivation and thus pNP is expected to cause electrode fouling. Nonetheless, the voltammograms were observed returning to the baseline after washing with tris buffer, which is of particular significance for doing real time measurements under similar conditions. This could be attributed to the use of microelectrodes with small test volumes (3 μL).A linear dependence of the scan rate on the peak current has been observed (supplemental information). Accordingly, a good linear relationship between the peak height and the concentration of IL-10 can be further established for the determination of unknown IL-10 concentrations.

Careful investigations also reveal a reversible redox peak at lower potential range of 66 mV (not shown for brevity) and could be attributed to the formation of nitrogenated and non-nitrogenated organic intermediates/quinones. This particular peak also show a strong dependence on the IL-10 concentration in the test samples, however demands more experimentation for better understanding. Absence of any appreciable oxidative behavior for similar experiments performed on planar thermally grown amorphous silica substrate (very light yellow color as compared to that of nanowire sample) confirms the role of nanowires in the present approach.

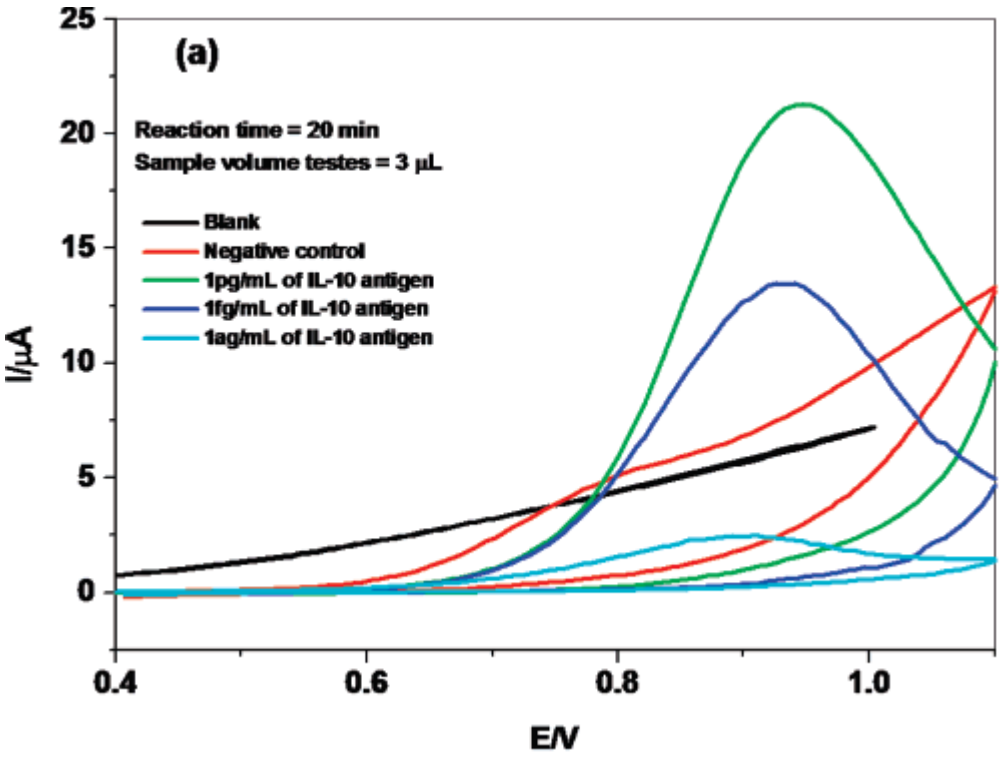

Figure 4.35 Cyclic Voltammograms (CV) Recorded for the Samples with Different Concentration of IL-10 in Tris Buffer (pH 9.2)

Inset shows the CV plot recorded for the sample with IL-10 concentration of 1fg/mL at scan rate of 100 mV/s.

(Reproduced with Permission)

Real sample testing were performed with the whole lung serum specimens that were collected from individuals who participated in lung cancer screening study, but were not diagnosed with lung cancer at the time of screening with lung imaging modality - helical CT (computer tomography). Figure 4.36 shows the electrochemical response recorded for both the whole and diluted serum (1:10 in PBS) with (1pg/mL) and without IL-10 antigen. No appreciable redox behavior was observed for the reaction products collected by performing the negative control experiment on both the whole and dilute serum i.e., without antigen. However, a presence of IL-10 antigen even at 1pg/ml level in the whole serum resulted in a redox reaction with an anodic peak at 0.6 mV. An increase in the peak current upon the usage of diluted serum could be attributed to the fact that the concentration of interferences present in the whole serum is higher as compared to that of diluted serum.

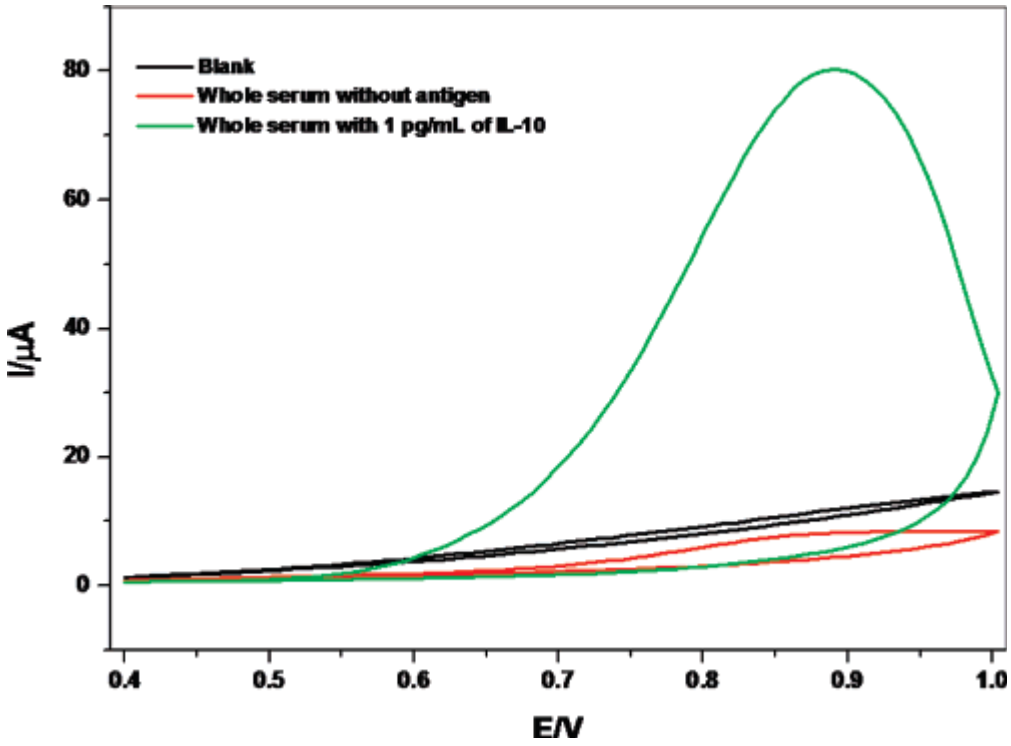

Figure 4.36 CV Plot Recorded for the Serum Samples with 1pg/mL Concentration of IL-10 at Scan Rate of 100 mV/s

(Reproduced with Permission)

4.6.3 Conclusions

In summary, we demonstrated the use of silica nanowires as an effective template for the enzyme immunoassay. More importantly, simple enzymatic reaction between the alkaline phosphatase enzyme and the PAPP was used to detect IL-10 concentration down to 1fg/mL in ideal and 1 pg/mL in clinically relevant samples of lung serum. Additionally, the electrochemical measurements were carried out in a smaller test volume of 3 μL. Moreover, a simple wash with the tris buffer rejuvenates the electrode surface suggesting the possibility of reuse of single electrode without cross contamination issues. Conclusive proof that the change in electrochemical responses observed were due to detection of IL-10 antigen was obtained through simultaneous use of optical and electrochemical measurements. Our results also demonstrate the feasibility of extending the present approach to other biomarkers by careful choice of nanowire modification techniques. Additionally, the use of aligned nanowires with controlled surface modification technique could further help in improving the detection limit less than 1 fg/mL.

4.7 Voltammetric Detection of Osteopontin Using Silica Nanowires

The high surface to volume ratio, coupled with the larger density of defect states on the nanomaterials, makes them highly sensitive to minor surface perturbations (i.e., binding chemistry). This could result in a sensor with a high degree of selectivity and sensitivity and a unique chemical signature. Among the one-dimensional nanoentities, silica nanowires (SiO_2-NWs) have been widely studied because of their unique anisotropy in physical, optical, electronic properties with excellent photoluminescence and biocompatability. Moreover, the nanowires' surface can be easily and effectively modified with the well-known chemistry of Si, thereby allowing the creation of a label-free platform for more sensitive detection of marker level. In the present work, the applicability of the SiO_2 nanowires as an effective template in the enzyme immunoassay for voltammetric (electrochemical) detection of Osteopontin (A lung cancer biomarker) has been demonstrated.

4.7.1 Experimental

The microfluidic device for carrying out the assay and testing as shown in figure 4.37 was fabricated in oxidized (100) silicon substrate. Also, the Au electrodes were fabricated on thermally oxidized silicon. This was accomplished by photolithography, subsequent e-beam evaporation and lift-off of Cr/Au layers. Cr (300 Å) was used as the adhesion layer for Au (1500 Å). One of the Au electrodes was plated with Ag for use as a reference electrode for the small volume samples. Microelectrodes are uniquely suited for the detection of the electrochemically reversible systems, for at moderate scan rates the non-planar diffusion between the electrodes gives rise to steady-state currents. A 60 µm tall microfluidic chamber of SU-8 (3 x 2 mm) (Microchem Corp., Newton, MA) was finally fabricated to hold the reagents. The SU-8 chamber was then hard-baked at 180 °C for 3 min to prevent any outgassing or contamination.

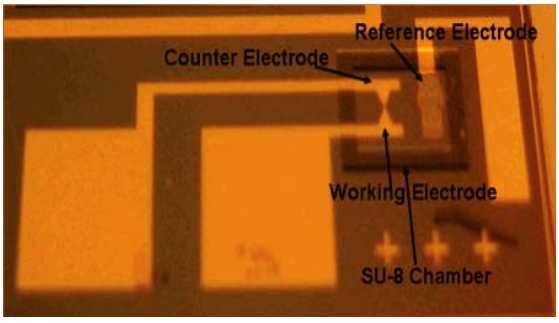

Figure 4.37 Optical Image of the Electrochemical Cell used for the Detection

All cyclic voltammetry was performed in a homemade cell with a total volume of 3 μL using an Autolab PGSTAT30 from Eco chemic N.V, at room temperature. A standard three-electrode configuration was used, in which the Au microelectrodes worked as both the working and the counter electrode, while the reference electrode was fabricated by depositing Ag on one of the Au electrodes. The use of an Ag-plated electrode in the miniaturized electrochemical cell is not a problem for the quantitative determination. pNPP was used as a substrate for electrochemical detection with AP enzyme, a useful enzyme for the heterogeneous electrochemical enzyme immunoassays. 25 One AP unit hydrolyzes 1 μmol of pNPP per min at pH 9.8 and 37 °C. The incubation time was also varied to establish the optimum working conditions. Both the concentrations of capture antibodies (1 μg/mL to 1 pg/mL), which corresponds to the concentration of 10 mM to 10 μM, and the OPN antigens (1 ng/mL to 1 ag/mL) were varied to estimate the detection limits of the proposed scheme and to find the optimal subset of parameters for the detection.

4.7.2 Results and Discussion

For better performance of the sensor, an optimum concentration of both the antigen and corresponding capture antibody must be established. Accordingly, experiments were carried out with varying concentrations of capture antibody and OPN antigen, respectively, in the test samples (buffer solution). Figure 4.38 shows the CV recorded for samples with varying concentrations of capture antibody with a fixed concentration of OPN antigen, i.e., 1 μg/mL. As the antigen concentration is higher, 100 pg/mL of capture antibody also resulted in the appreciable anodic peak current.

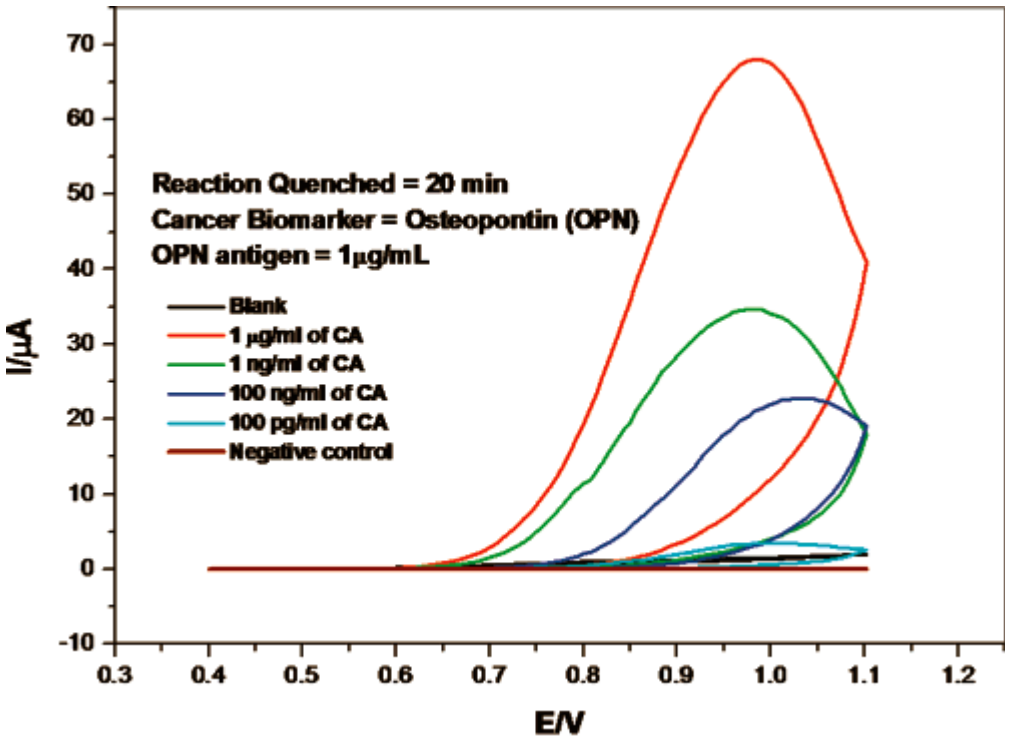

Figure 4.38 CV Recorded for Samples with Varying Concentrations of Capture Antibody with a Fixed Concentration of OPN Antigen
(Reproduced with Permission)

Figure 4.39a shows the CV plot recorded with varying concentrations of antigen with a fixed capture antibody concentration of 0.5 µg/mL. Figure 4.39b shows a good linear dependence with respect to antigen concentration that can be fitted to a linear equation with slope = 0.41 and intercept at 3.69, respectively. A correlation coefficient and the standard deviation as derived from the linear fit is 0.98 (R^2 = 0.96) and 1.23, respectively. Thus, it is evident that both the antigen and antibody concentration have a vital impact on the anodic peak current. pNP can therefore be quantified by measurement of the height of the peak current, thereby giving the concentration of cancer antigens. Moreover, pNP solutions have indefinite stability at room temperature and need not be degassed for storage.

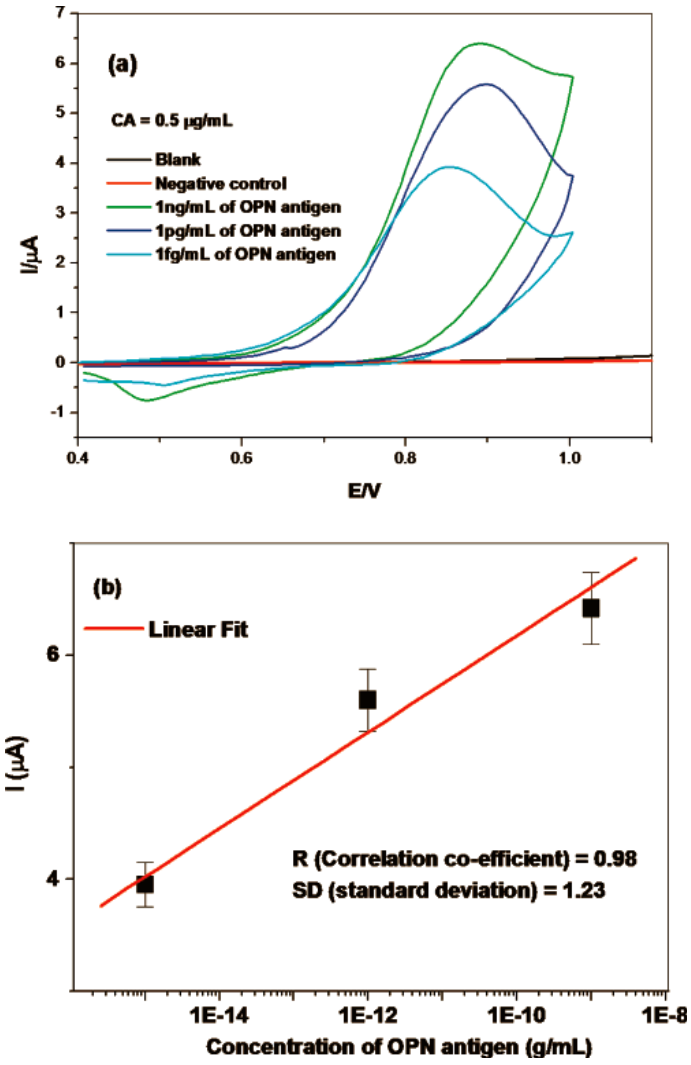

Figure 4.39 CV Plot

(a) CV Recorded with varying concentrations of OPN antigen with a fixed CA concentration of 0.5 fg/mL and (b) The linear dependence of anodic current on the antigen concentration.

4.7.3 Conclusions

In summary, we demonstrated the use of silica nanowires as an effective template for the enzyme immunoassay. Both the capture antibody concentration and the antigen concentration have a strong influence on the anodic peak current as demonstrated by the results with OPN. Additionally, the electrochemical measurements were carried out in a smaller test volume of 3 µL.

The density of nanowires also has a significant impact on the response, implying the possibility of further improvement in sensitivity and selectivity upon using nanowires with controlled aspect ratio and density. Our results also demonstrate the feasibility of extending the present approach to other biomarkers by careful choice of nanowire modification techniques. Additionally, the use of aligned nanowires with well-defined aspect ratio and controlled surface modification technique could further help in improving the detection limit. Also, leveraging the electroactive nature of silica nanowires, a multimodal optical/electrochemical) sensing platform for accurate biodiagnostics could also be easily implemented. This can be further extended to develop an integrated system-on-chip (SOC) in which distinct nanowires and surface receptors can be incorporated as individual device element.

4.8 Ion Beam Synthesis and Doping of Photonic Nanostructures

Whilst there has been intense interest in the synthesis, structure and properties of silica nanowires, little work has been performed on optical doping and functionalization of such materials. In the present study, we report new results for Er-doped silica nanowires, including the impact of the nanowire structure on the Er luminescence and a novel ion-implantation technique that enables simultaneous nanowire growth and doping.

4.8.1 Experimental

The synthesis of optically-active silica nanowires on silicon substrates using ion-implantation, with two different strategies employed for their fabrication has reported [28]. First is based on Er implantation of nanowires produced by a thin-film Pd catalyst layer, and the second employing implanted Er as both the catalyst and dopant. The luminescence properties of the resulting Er-doped silica nanowires are reported and compared with similarly implanted fused silica samples.

In this research, silica nanowires were synthesized using Pd thin film catalysis as reported earlier. Subsequent doping of the nanowires was achieved by ion-implantation with 110 keV ErO^- to fluences in the range from 5×10^{14} to 1×10^{16} ions.cm^{-2}, and fused silica samples were simultaneously implanted for comparison. The implanted Er has a mean-projected range in SiO_2 of 45 nm and its peak concentration ranges from 0.3 at. % to 5 at. % for the fluences studied. All samples were then annealed at 900°C for 1 hour in either N_2 or O_2 to optically activate the erbium. As an alternative doping strategy, silicon samples were implanted with 30 keV ErO^- ions to a fluence of $6x10^{14}$ ions.cm^{-2} and annealed to 1100^o C to induce nanowire growth from Er precipitates. These experimental procedures are summarized in figure 4.40.

Photoluminescence (PL) measurements of the Er emission were performed at room temperature using the 488 nm line of an argon ion laser as the excitation source. The luminescence emission was analyzed with a Triax 320 spectrometer equipped with a high-sensitivity liquid-nitrogen cooled germanium detector. The excitation laser was mechanically chopped at 15 Hz and standard lock-in techniques employed to collect the spectra. For time resolved measurements, the output of the detector was connected directly to a digital storage oscilloscope and the response averaged over 128 cycles. The time response of the system is estimated to be less than 0.5 ms.

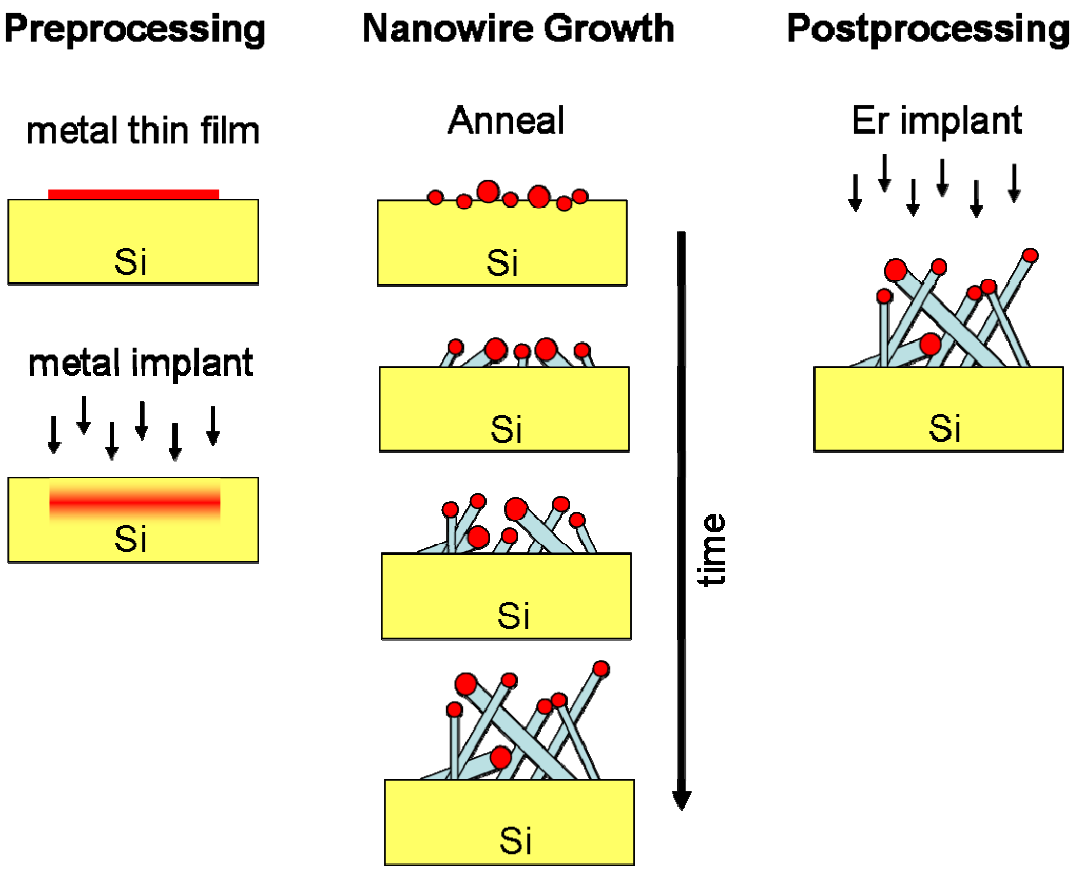

Figure 4.40 Schematic Diagram Showing Sample Processing Conditions
Preprocessing includes the formation of metal catalyst particles by thin film deposition and decomposition, and ion-implantation and precipitation. Nanowire growth is achieved via high temperature annealing in an ambient containing a low partial pressure of oxygen. Post processing is achieved by ion-implantation of Er ions.

4.8.2 Results and Discussion

The physical structure of nanowires produced by Pd-thin-film induced self-assembly is shown in figure 4.41. Wires have diameters in the range from 100 nm to 1 μm (average of around 150 nm) and lengths exceeding 100 μm. The diameter of individual nanowires is relatively constant along their length although many exhibit kinks and twists during growth, as shown in the high-resolution SEM image of figure 4.41. Significantly, SEM images of samples implanted with 110 keV ErO^- ions showed no obvious change in structure.

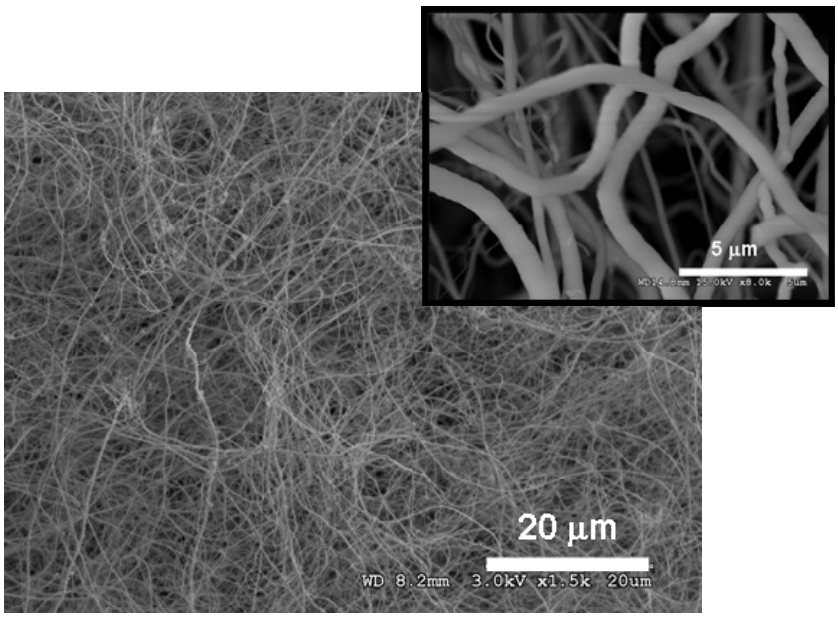

Figure 4.41 SEM Images Showing Nanowires Produced by Pd Induced Growth on Silicon A 20 nm of Pd was deposited onto the silicon and annealed at 1100°C in Ar for 4 hours. Low and high magnification images are shown**.**

Figure 4.42 shows an RBS spectrum of the nanowire sample after implantation with 110 keV ErO^- to a fluence of $5x10^{14}$ cm^{-2}. Although interpretation of this spectrum is complicated by the complex sample structure it is evident that the nanowire layer is thick enough to fully stop backscattered He ions, suggesting that it has an equivalent thickness > 2 µm of bulk SiO_2. Comparison with simulations further suggests that the nanowires are composed of silicon-rich silicon-dioxide (i.e. SiO_x) rather than stoichiometric SiO_2. (The exact stoichiometry is difficult to deduce due to the underlying signal from the Pd, or Pd-silicide, catalyst). Scattering from the Pd (or Pd-silicide) catalyst shows that it is distributed throughout the nanowire layer, consistent with its expected transport during the growth of the wires (see figure 4.40). Finally, scattering from the implanted Er shows that it is located in the 'near-surface' region of the nanowire array, as expected from the fact that the projected range of Er is less than the average nanowire diameter.

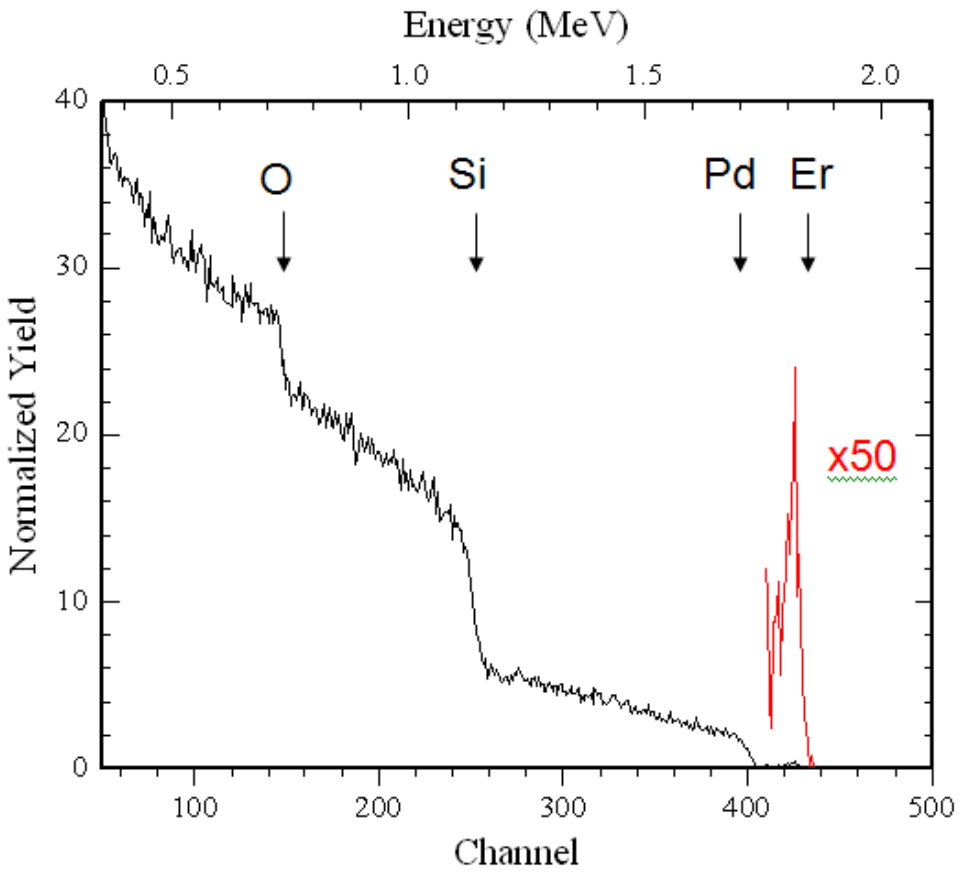

Figure 4.42 RBS Analysis of Er Implanted Silica Nanowires
The sample was implanted with 110 keV ErO^- ions to a fluence of $5x10^{14}$ cm^{-2} and analysis performed with 2.0 MeV He^+ ions using normal incidence and a scattering angle of 168^o.

Representative PL spectra from Er implanted nanowires are shown in figure 4.43 for samples implanted to fluences of $6x10^{14}$ $Er.cm^{-2}$ and $1x10^{16}$ $Er.cm^{-2}$. The 1.54 μm emission corresponds to the $I_{13/2}$ to $I_{15/2}$ transition in Erbium, as shown in the schematic of the energy level scheme. These spectra are typical for Er in silica, as is the slight spectral broadening of the emission from the high fluence sample. However, despite these similarities, significant differences are evident in the Er emission from bulk silica and nanowire samples, as discussed below.

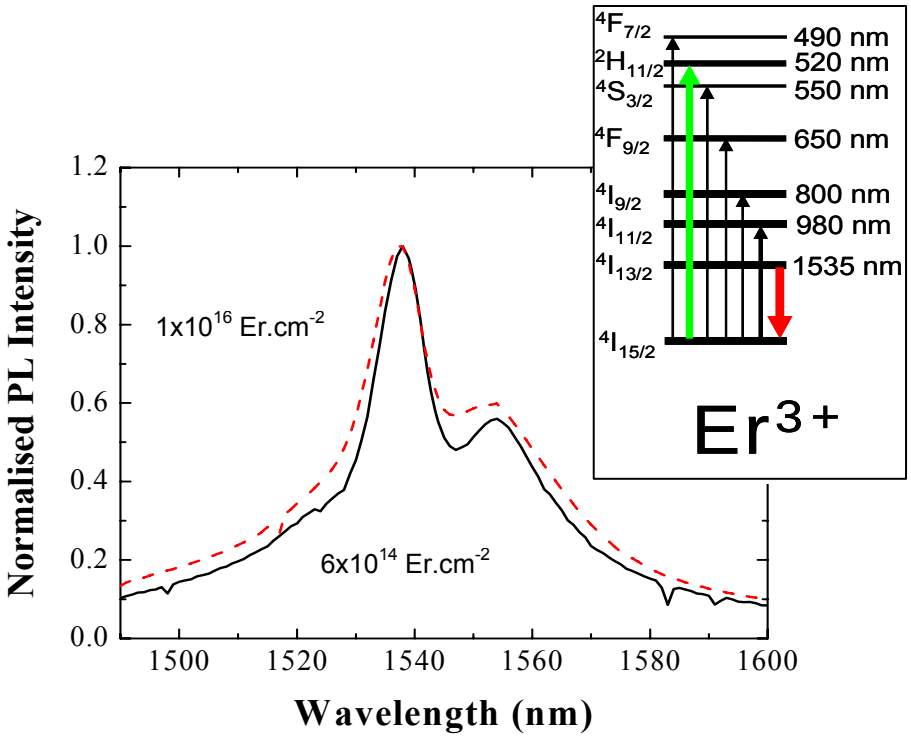

Figure 4.43 Typical Photoluminescence Spectra from Er Doped Silica Nanowires

Inset: Schematic of the Er^{3+} Energy Level Scheme showing the $^4I_{13/2}$ to $^4I_{15/2}$ Transition giving rise to the 1535 nm emission.

Spectra represent room-temperature measurements for samples implanted with $6x10^{14}$ and $1x10^{16}$ $ErO^{-}.cm^{-2}$.

Figure 4.44 shows the integrated PL intensity from nanowire and bulk silica samples implanted to various fluences and annealed at 900^0 C in either N_2 or O_2. For bulk silica samples the PL intensity initially increases with increasing fluences before reaching a maximum at a fluence of around $3x10^{15}$ $Er.cm^{-2}$ and then decreasing at higher fluences, behavior previously attributed to concentration quenching [29]. In contrast, the PL intensity from nanowire samples increases monotonically with increasing fluences, with no evidence for a saturation effect. In many respects the response of the nanowire samples is similar to that of bulk-silica samples implanted to lower fluences, and such an effect might be expected from the complex implant geometry presented by the nanowires.

An estimate of these geometrical effects based on the small dimensions and cylindrical geometry of the nanowires suggests that the effective implant fluences may well be reduced by a factor of 1.5 - 2.0 in these structures, partly explaining the observed behavior.

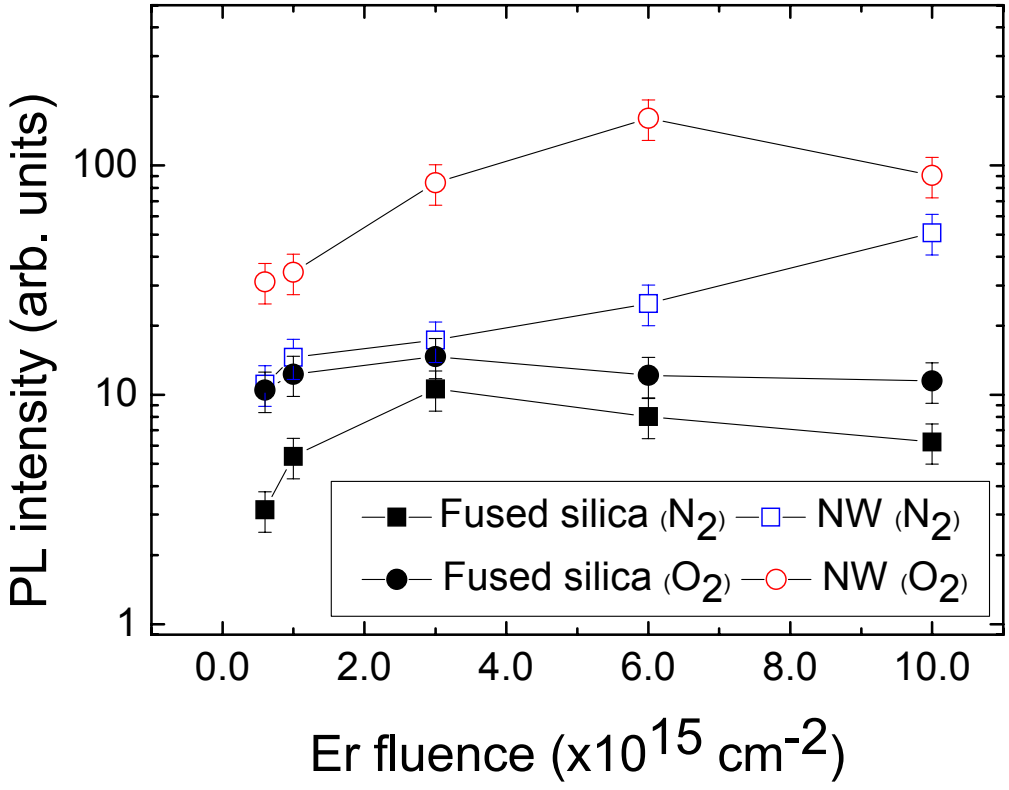

Figure 4.44 Integrated PL Intensity Data for Bulk Silica and Nanowire Samples Implanted with 110 keV ErO^- Ions to a Fluence of $6x10^{14}$ cm^{-2} after Annealing at 900°C for 1 hour in N_2 and O_2.
(The absolute intensities from bulk and nanowire structures cannot be compared directly.)

Another significant difference between the PL response of nanowire and bulk silica samples is illustrated in figure 4.45. This compares the temporal decay of the PL signal for bulk and nanowire samples implanted to a fluence of $6x10^{14}$ $Er.cm^{-2}$. These data show that the PL lifetime in nanowire samples is longer than in comparably implanted bulk silica samples, an effect that is attributable to the nanostructure of the sample, as discussed below.

The spontaneous emission rate of an optically active centre, Γ_{ij}, is given by Fermis' golden rule:

$$\Gamma_{ij} = \frac{\pi\omega}{\hbar\varepsilon(R)}\left|M_{ij}\right|^2 \rho(\omega, R) \quad \text{.....(4.3)}$$

Where,

ω is the angular frequency of the radiation,

ε (R) is the (position dependent) dielectric function,

M_{ij} is the dipole transition matrix, and ρ (ω, R) is the optical density-of-states which is proportional to the refractive index of the medium, n [30, 31].

Confinement of Er ions within silica nanowires is expected to reduce the available optical density-of-states in two ways. Firstly, the wire will act as a single mode waveguide and thereby restrict the solid angle for emission, and secondly the nanowire layer will have an average refractive index less than that of bulk silica (i.e. $1.0 > n < 1.5$). Both effects will lead to a reduction in the transition rate and therefore increase the luminescence lifetime, as observed.

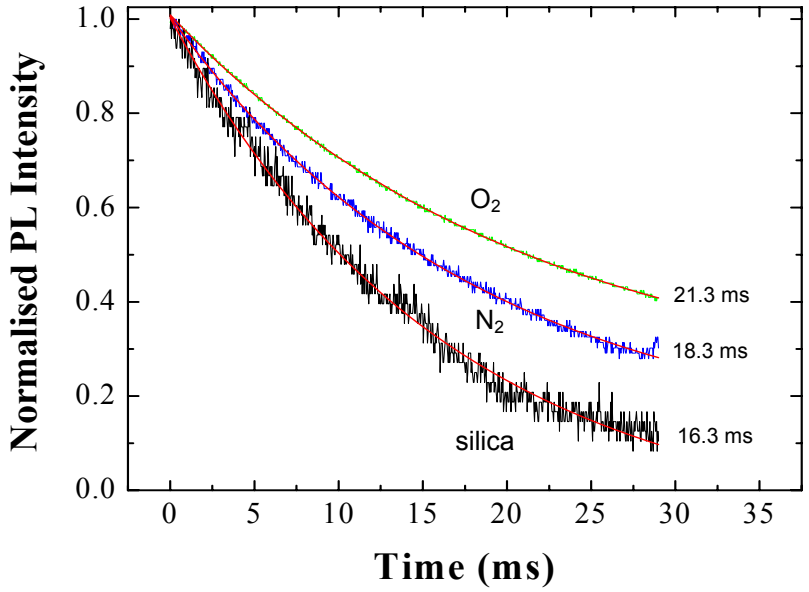

Figure 4.45 Normalized Time Resolved PL Measurements of the 1.54 μm Emission for Nanowire Samples

Nanowire sample implanted with 110 keV ErO^- Ions to a Fluence of $6x10^{14}$ cm^{-2} after Annealing at 900°C for 1 hour in N_2 and O_2. Measurement for a Fused silica sample included for reference. PL lifetimes are indicated for each sample.

Annealing in oxygen increases the PL intensity and increases the luminescence lifetime. For the sample implanted to a fluence of $6x10^{14}$ $Er.cm^{-2}$ the intensity increases by a factor of 3-5, whilst the lifetime increases by around 15 - 20%. The PL intensity, I_{PL} is given by:

$$I_{PL} = \sigma\tau\phi n / \tau_{rad} \quad \text{.....(4.4)}$$

Where,

σ is the absorption cross-section,

φ is the photon flux,

n is the number of optically active centers,

τ is the luminescence lifetime and

τ_{rad} is the intrinsic radiative lifetime of the centre)

The observed increase in intensity cannot be accounted for by the increase in lifetime alone. It is therefore concluded that this increase is largely due to an increase in the optically active Er^{3+} fraction for samples annealed in O_2. The increase in PL lifetime, on the other hand, is expected to result from a reduction in the concentration of non-radiative defects that compete with the radiative emission.

Finally, an alternative approach to the fabrication of Er-doped nanowires is introduced. This involves the use of Er metal as the catalyst for nanowire growth, a process that simultaneously dopes the nanowires as they grow. A small concentration of Er is expected to be incorporated into the growing nanowires and exhibit Er luminescence similar to that reported above. These preliminary measurements are currently being extended to better understand and optimize this and related processes.

4.8.3 Conclusions

In summary, two different approaches to the synthesis of Er-doped silica nanowires were presented together with data on the optical properties of the resulting materials. In the first approach, nanowires were fabricated by a metal-induced growth process using a Pd thin-film as the catalyst layer, and these were subsequently implanted with low energy Er ions. In the second approach, implanted Er was used as both the catalyst and dopant. The luminescence properties of these structures were reported and discussed in relation to comparable Er-doped fused silica samples. Differences between the response of bulk-silica and nanowire samples were discussed in terms of the material nanostructure.

4.9 Optical Emission from Erbium Doped Silica Nanowires

There has been an explosion of interest in the synthesis, structure, properties, and applications of nanostructures in recent years, largely stemming from the fact that materials confined in one or more dimensions can exhibit interesting properties as well as provide the basis for new devices. Nanowires (NWs), which are structures confined in two dimensions (typically 1–100 nm long and with diameters in the range 1–200 nm), represent an important class of nanomaterials that have found widespread application in fields as diverse as microelectronics, optoelectronics, and biosensing. Silica NWs are of interest in this regard because silica is known to be a suitable host for optically active impurities and is chemically inert and biocompatible, making it a suitable choice for use in integrated photonics and biosensing. Infrared optical emission from erbium-doped silica nanowires is shown to have property characteristic of the material nanostructure and to provide the basis for the fabrication of integrated photonic devices and biosensors.

4.9.1 Experimental

Optically active silica nanowires on Si were synthesized via VLS mechanism using Pd thin film catalysis. Silica nanowires of approximately 150 nm diameter were grown on a silicon wafer by metal-induced growth using a thin (20 nm) sputter-deposited palladium layer as a catalyst. The resulting wires were then ion implanted with 110 keV ErO^- ions and annealed at 900°C to optically activate the erbium. PL measurements were performed by exciting samples with light of wavelength 488 nm from an Ar-ion laser and analyzing the luminescence emission with a Triax 320 spectrometer equipped with a high-sensitivity liquid-nitrogen cooled germanium detector. The excitation laser was mechanically chopped at 15 Hz and standard lock-in techniques were employed to collect the spectra. For time resolved measurements, the output of the detector was directly connected to a digital storage oscilloscope and the response averaged over 128 cycles. The time response of the system is estimated to be less than 0.5 ms. Temperature-dependent measurements were performed over the temperature range from 10 K to room temperature (300 K) using a Janis closed cycled helium cryostat with quartz windows.

4.9.2 Results and Discussion

The representative PL spectra from Er doped NWs implanted to low and high fluences indicate the characteristic Er^{3+} transition at 1.54 μm as show in figure 4. 44. Figure 4.46 shows the integrated PL intensity as a function of pump power (photon flux) as measured at room temperature from bulk-silica and NW samples implanted to two different Er fluences.

No significant saturation of the PL intensity is observed for photon fluxes up to 4 x10^{25} photons m^{-2} s^{-1}, consistent with the low absorption cross section expected for Er in SiO_2 at the excitation wavelength (typically around 10^{-21} cm^2 for Er in bulk SiO_2 at 488 nm.)

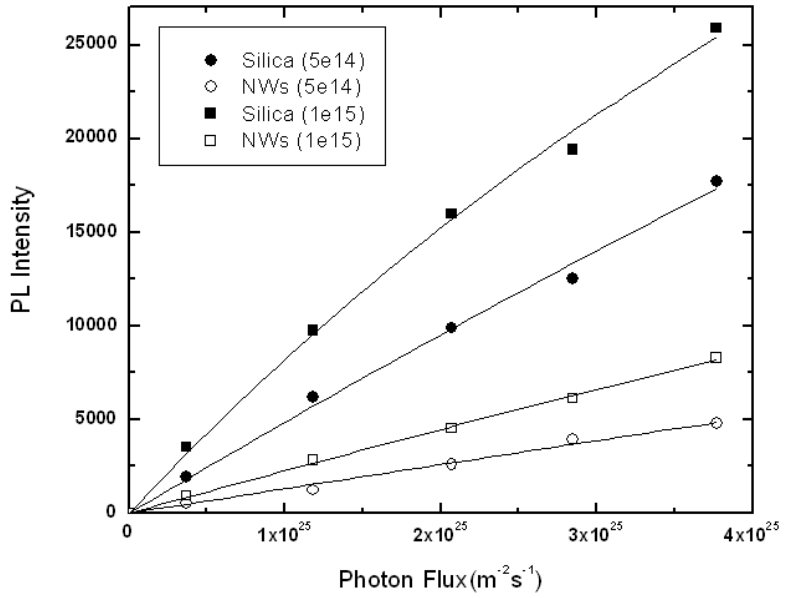

Figure 4.46 Integrated PL Intensity as a Function of Photon Flux for Bulk Silica and Nanowire Samples Implanted to the Fluences Indicated

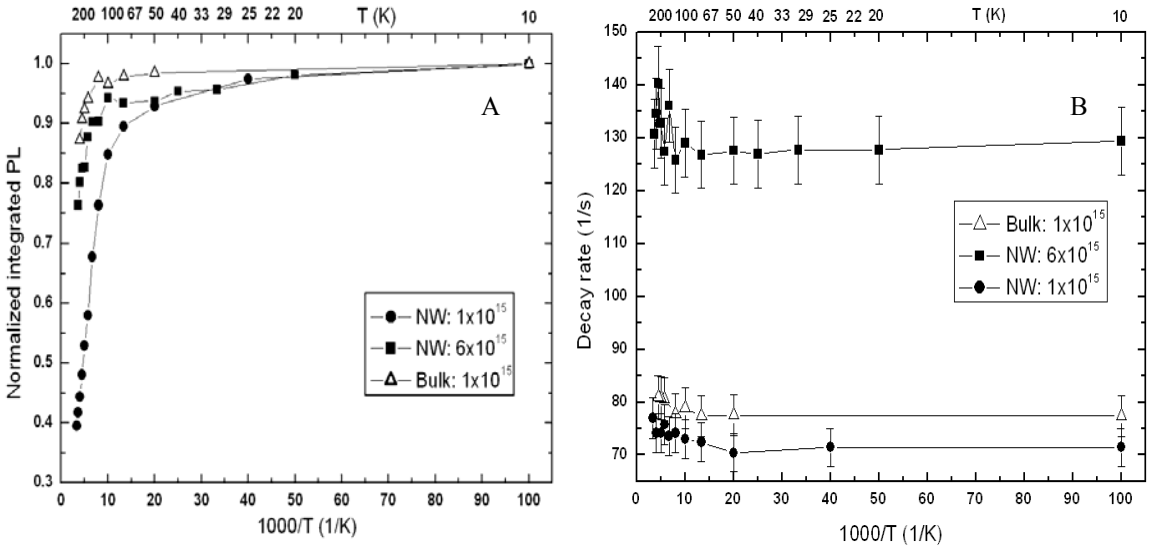

Figure 4.47 Temperature Dependence on the Optical Emission of Fused Silica (Bulk) and Silica Nanowires Doped with Er

(A) Fused silica showing a weak PL dependence on temperature; In nanowire samples, significant temperature quenching has been observed and (B) Below 50 K, the decay rate of both the samples are independent of temperature, though a higher dose nanowire sample

Figure 4.47 shows the temperature dependence (10–300 K) of the PL intensity and lifetime measured at 1.54 μm for samples implanted to fluences of 1015 Er cm^{-2} (0.5 at. %) and $6x10^{15}$ Er cm^{-2} (3 at. %). Consistent with previous reports, the PL intensity and decay rate for the bulk silica reference sample exhibit only a weak dependence on temperature, although some thermal broadening of PL spectra from these samples was observed over this temperature range. The PL intensity falls around 12% between 10 and 300 K, while the lifetime decreases by around 5% over the same temperature range. In contrast, the NW samples show significant temperature quenching, particularly in the temperature range above 100 K. For the sample implanted with $1x10^{15}$ Er cm^{-2}, the PL intensity decreases by 60% over the temperature range from 10 to 300 K, while the lifetime decreases by only 7%. The PL intensity is proportional to the product of the active Er concentration, n, and the luminescence lifetime, τ.

The data in figure 4.47 therefore demonstrate that the reduction in intensity above 100 K is mostly due to a reduction in the optically active erbium concentration. For Er-doped c-Si, two luminescence quenching regimes have been identified.

Below 150 K, an impurity Auger effect involving free carriers is dominant, and above 150 K a nonradiative, multiphonon emission process (back transfer process) is dominant. However, the Auger effect is significantly reduced for Er in silica due to the low concentration of free carriers, and although back transfer is still present above 150 K, it is reduced, too, due to the large mismatch between the band gap of SiO_2 and the first excited state of Er^{3+}. It is therefore speculated that quenching in the current case arises from a temperature-dependent defect interaction that is very fast compared to the luminescence lifetime. Such quenching is likely to be a direct consequence of the unique structure of the silica NWs and possibly results from enhanced charge trapping and recombination at bulk and surface defects. The latter is expected to be particularly significant due to the large surface-to-volume ratio of the NWs. Such effects are particularly germane to biosensing where surface adsorbates could be expected to influence the quenching rate of the luminescence.

The data in figure 4.47 further show that thermal quenching is concentration dependent, with the NW sample implanted to $1x10^{15}$ Er cm^{-2} exhibiting a stronger thermal quenching effect than a similar sample implanted to $6x10^{15}$ Er cm^{-2}. The reduced thermal quenching in the latter case is due to the significant concentration quenching already present in this sample, i.e., the effect of thermal quenching is mitigated by the concentration quenching for high Er concentrations. Thermal quenching becomes dominant at lower erbium concentrations where competing processes are reduced in significance.

4.9.3 Conclusions

In summary, it has been shown that optically active silica NWs can be produced by ion implantation of dopants into pre-existing nanostructures and that the optical emission from these structures exhibits features characteristic of the nanostructure. These include a reduced luminescence decay rate due to a lower optical density of states in the NW samples, reduced concentration quenching due to a lower effective Er concentration in ion-implanted NW samples, and enhanced thermal quenching attributed to the proximity of surfaces to the emitting center and the large surface-to volume ratio of the nanostructures.

The latter is particularly significant as it suggests that the luminescence emission from Er is very sensitive to the state of the NW surface and as such should respond to changes in the surrounding ambient. This raises the possibility of using functionalized NW surfaces to selectively detect absorbed molecules via changes in the luminescence.

4.10 Enriched Erbium Emission for Nanoengineered Silicon Surface

Trivalent rare-earth ions are optically active species with ocular transitions in the visible and near infra-red spectrum. The emission from Er^{3+} at 1.54 μm (characteristic of the $^4I_{15/2} - {}^4I_{13/2}$ transition in erbium) is of particular interest as it is used extensively for optical telecommunication. A critical challenge in many such applications is the need to achieve maximum Er emission intensity (high active concentration and long luminescent life time). Reports on enhancing the optical activity of Er^{3+} have established that the Er emission can be increased either by the addition of impurities or clusters that act as sensitizers for Er excitation or changing the local atomic environment to increase the fraction of Er in the 3^+ oxidation state, or increasing the rate of Er excitation by local field enhancement in the vicinity of metallic particles. The presence of non-radiative defects also has a significant effect on the emission intensity and the passivation of such defects has been shown to lead to a substantial increase in emission intensity.

Er-emission has been investigated in a range of host materials, including Si and SiO_2, and in structures with a range of micro-, meso- and nano-scale architectures. Among the hosts, silicon has received particular attention due to its potential for the integration of electronic and optical systems. The fact that the solubility and luminescence efficiency of Er in many materials, especially in bulk Si, is quite low has led to the use of nanometer-scale structures in many applications. In this research, silica nanowires have been investigated as an Er sensitizer.

4.10.1 Experimental

In the present study [32], this approach is exploited to produce catalyst particles based on Er and Au, and Er only, with a view to incorporating optically active Er along the full length of the nanowire rather than the upper most layers doped by ion-implantation of pre-existing nanowires. In this study, nanowire growth was performed on prime-grade (100) silicon wafers using ion-implanted metals as the catalyst. Two sets of samples were prepared for comparison. One set of Si samples were implanted with Er (Er) and rest co-implanted with Au and Er (Au: Er). For (Er) samples the Si wafers were implanted with 30 keV ErO^- ions to fluences in the range from $6x10^{14}$ cm^{-2} to $1x10^{16}$ cm^{-2}. For the (Au: Er) samples, the wafers were additionally implanted with 30 keV Au^- ions to a fixed fluence of $3x10^{16}$ cm^{-2}. The projected range of Er and Au in Si was around 21 nm in both cases [33]. After implantation at room temperature, the samples were annealed at 1100^o C in a closed tube furnace for 4 hrs in an Ar ambient.

The nanowires were then inspected using scanning (SEM-S800, S4500) and transmission electron microscopes (TEM- CM 300, FEI Tecnai F20 S-Twin) equipped with Energy Dispersive X-ray (EDX) detectors. TEM samples were prepared by scraping the wires from the substrate and dispersing them in alcohol before deposition onto a copper grid.

4.10.2 Results and Discussion

Figure 4.48 compares the morphology of silica nanowires produced by annealing silicon wafers implanted with Au and Er, and Er only. In both cases, the wires were found to nucleate heterogeneously on the silicon surface and to have lengths exceeding 10's of micrometer. The average diameters were estimated to be 175 and 125 nm for Au: Er and Er based catalysis respectively. The morphology of the wires was also found to vary for the two catalyst variants. Wires seeded by the Au: Er catalyst combination exhibited a twisted and corrugated morphology, while those seeded by Er exhibited a relatively smoother morphology.

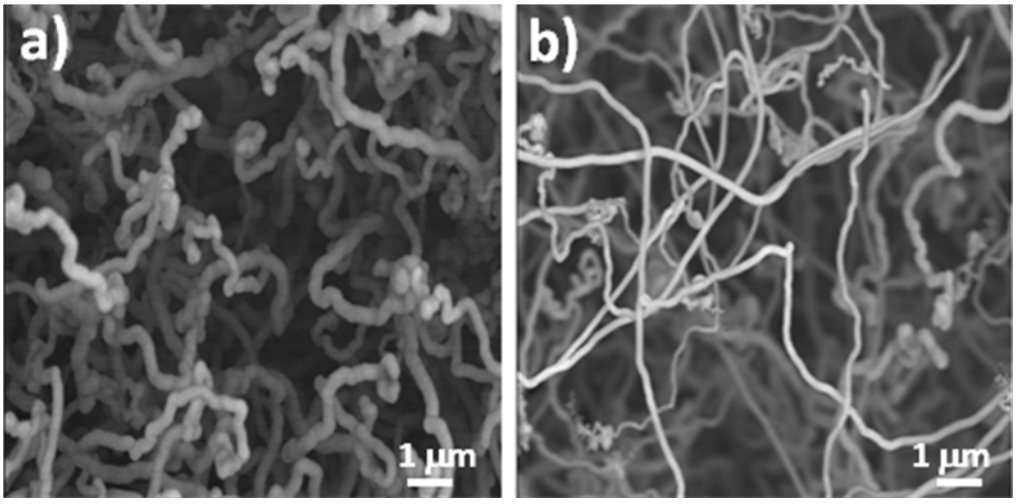

Figure 4.48 SEM Micrographs of Nanowires Produced by Implanting (100) Si Wafers a) Au (30 keV Au^-, $3x10^{16}$ ions.cm^{-2}) + Er (30 keV, $3x10^{15}$ ErO^- ions.cm^{-2}) and b) Er ($3x10^{15}$ ErO^- ions.cm^{-2}). Average wire diameter is: a) 175nm, b) 125nm.

Figure 4.49 is a composite of SEM micrographs illustrating the morphologies of nanowires catalyzed by a) Au (30 keV, $3x10^{16}$ ions.cm^{-2}) + Er (30 keV, $3x10^{15}$ ions.cm^{-2}), b) Er ($3x10^{15}$ ions.cm^{-2}) and c) Er ($6x10^{14}$ ions.cm^{-2}). The number density of the nanowires was estimated using these SEM micrographs by counting the wires in five 100 μm^2 of SEM images and averaging them.

Table 4.5 compares the number density of nanowires for various concentrations of Er. An increase in the number density of wires was observed in Er seeded wires as the Er fluence was increased from $6x10^{14}$ to $6x10^{15}$ ions.cm^{-2},and an additional two-three fold increase in the number density of wires was observed for a given Er implant fluence when Au was incorporated as a co-dopant. This is consistent with the fact that Au is an effective catalyst for nanowire growth in its own right.

SEM micrographs of the Er implanted sample using back scattered mode (figure 4.50 a) indicate the presence of a high-atomic number element on the nanowire tip, and X-ray Diffraction (XRD) spectra, such as that shown in figure 4.50 c, shows peaks consistent with the presence of polycrystalline Er. This is consistent with a float-growth process in which Er is present at the growing tip of the wire. For low Er concentrations, where minimal metal is available for catalyst formation, the wires also seem to be tapered.

It is well known that the length of the nanowires is a function of the available catalyst material as nanowires grow at the expense of consuming the catalyst [34]. This can lead to tapering of the nanowires due to a reduction in the catalyst volume as growth proceeds.

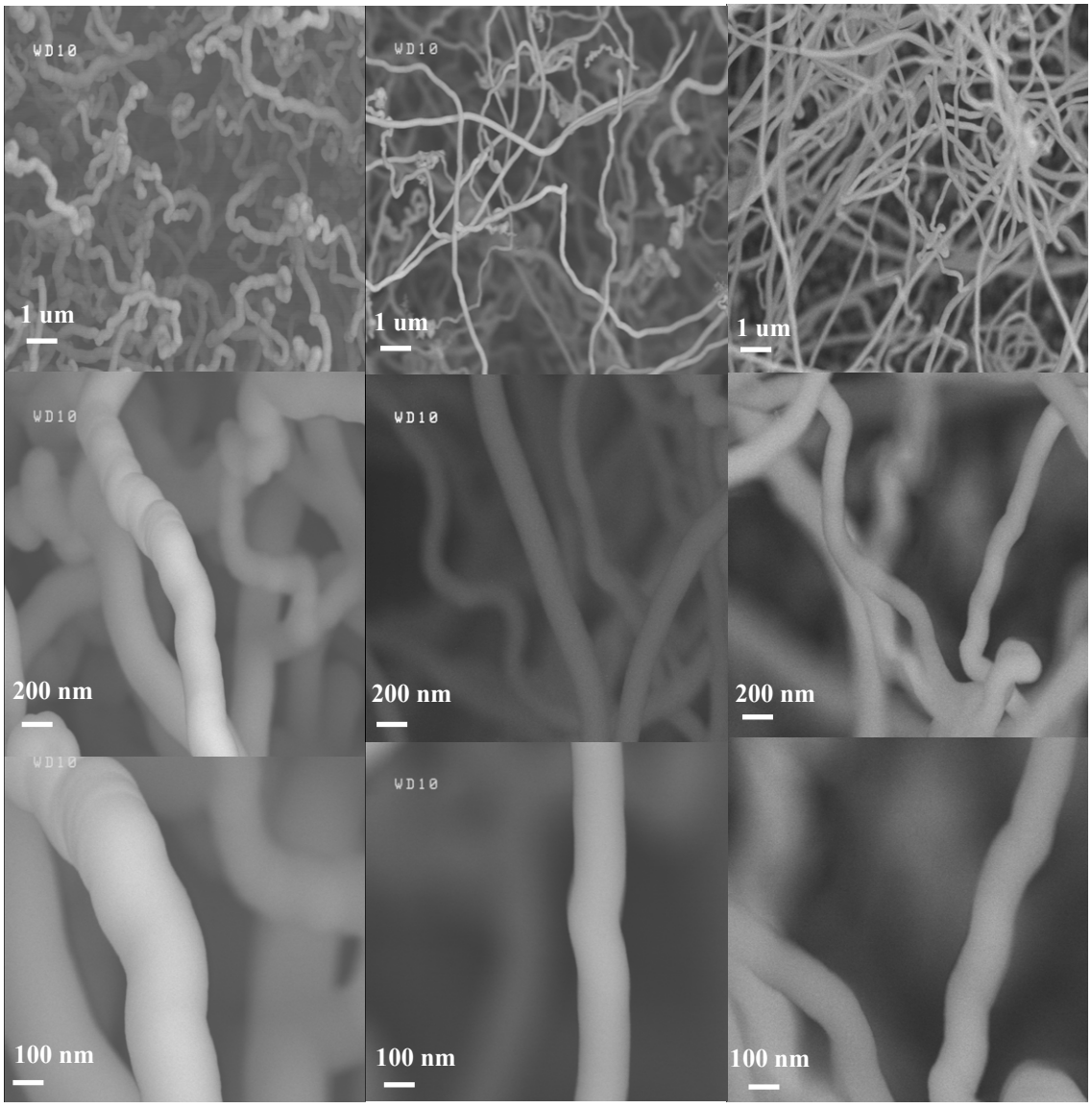

Figure 4.49 SEM Micrographs of Ion Implantation Seeded Nanowires Using Different Catalyst Combinations

a: Au (30 keV, $3x10^{16}$ ions.cm^{-2}) + Er (30 keV, $3x10^{15}$ ions.cm^{-2}), b: Er ($3x10^{15}$ ions.cm^{-2}) and c: Er ($6x10^{14}$ ions.cm^{-2}). Number Density of the Nanowires: c<b<a

Tapering can also occur when the vertical growth rate is comparable to the lateral growth at the base of the wires. Slow growth might reasonably be expected for Er-mediated growth as Er-metal and its silicides have melting temperatures above that employed for nanowire growth.

As a consequence growth is likely due to a vapor-solid-solid process rather than the vapor-liquid-solid process associated with the Au: Si eutectic system. As solid-phase diffusivities are much lower than liquid-phase diffusivities, the transport of reactants from the gas phase to the growing nanowire, and hence the nanowire growth rate, is expected to be correspondingly lower in this case. Figure 4.50 b shows an SEM image (secondary electron mode, S800) of Au: Er seeded nanowires characterized by globules at its tip. EDX results (figure 4.50 d) at the apex and body of Au: Er seeded nanowires suggest that Au is concentrated at the nanowire tip, again consistent with a float-growth model as reported by Kolasinski [35].

Table 4.5 Number Density Estimate of Nanowires with Varying Er Concentration

Er Dose (ions/cm^2)	**Number Density of Nanowires x 10^{12}(wires/cm^2)**	
	Er	**Au (3e16) + Er**
1e16	3.8 (4)	11.6 (12)
6e15	2.7 (3)	7
3e15	2	4
1e15	1.4 (1.5)	3.2 (3)
6e14	0.9 (1)	1.5 (2)

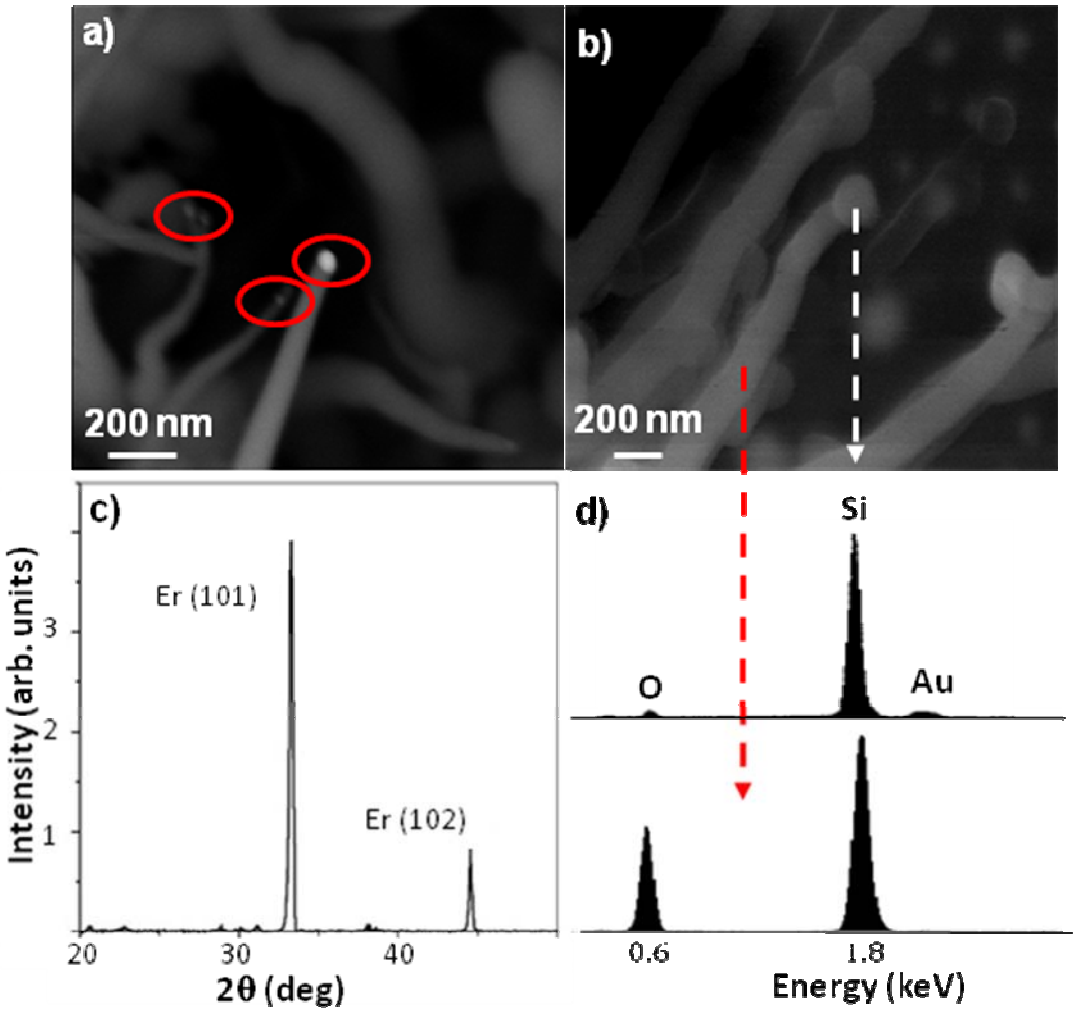

Figure 4.50 SEM Characterization of the Nanowires Catalyzed by Er Implantation (30 keV ErO^-, $6x10^{14}$ ions.cm^{-2}) and Au: Er co-implantation (Au – 30 keV Au^-, $3x10^{16}$ ions.cm^{-2} + Er – 30 keV ErO^-, $3x10^{15}$ ions.cm^{-2}) heated at 1100 C for 4 hrs.

(a) Back scattered SEM (S 4800) micrograph of the Er implanted sample showing differential contrast indicating the role of Er as a catalyst to induce nanowire growth of average diameter of 125 nm, (b) SEM (S 800) micrograph of Au:Er co-implantation seeded nanowires (of average diameter 175 nm) (c) Er seeded nanostructures: Absence of crystalline peak at 32^0 (θ-2θ), indicates the amorphous nature of these nanostructures while recording the existence of Er crystallites seen around 33.2^0 and 44.5^0 , and (d) Au:Er seeded nanostructures: EDX images on the apex (black arrow) and body (red arrow) of the nanowire suggests Au catalyzed nucleation of wires composed of Si and O.

A TEM image of the Er seeded nanowire is shown in figure 4.51a. This confirms the relatively smooth surface morphology of the wires and the associated diffraction pattern (Figure 4.51b) shows diffuse rings, consistent with the amorphous structure of the SiO_x nanowires. In contrast, the TEM image (figures 4.51c) of a wire grown from Au: Er catalyst shows a corrugated nanowire surface coated with small particles. The high magnification TEM image in figure 4.51 d shows a subset of smaller particles present on the nanowire surface. The inset SAED pattern in figure 4.51c, taken from the nanowire, is consistent with the presence of metallic Au and Er and suggests that the particles present on the nanowire surface are formed from the catalyst metals. Nucleation of semiconducting nanowire heterostructures has been discussed in detail recently in a topical review by Lieber et al. [36], with metal precipitation along the nanowire body attributed to a combination of VLS and VS (Vapor Solid) mechanisms. Such a combination of mechanisms might reasonably be expected in the present case as Au-mediated growth is expected to proceed via a VLS mechanism while Er and its silicides are expected to remain solid at the growth temperature, as discussed earlier.

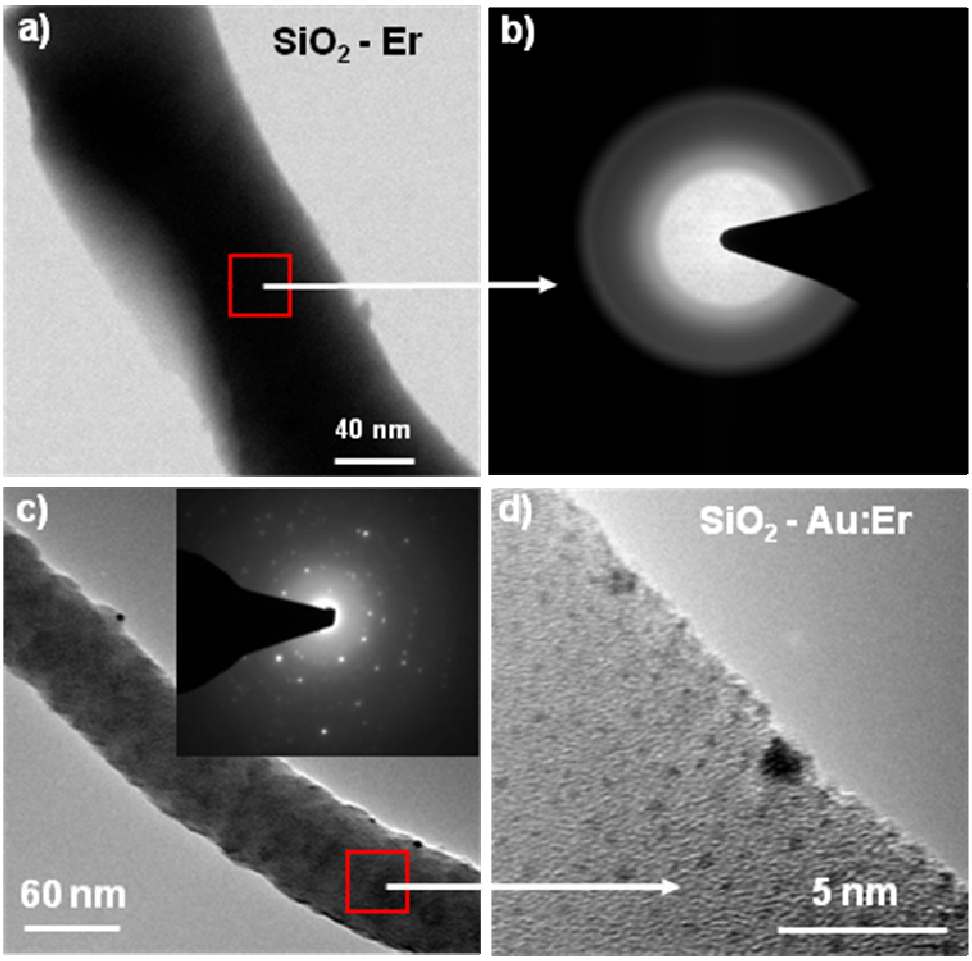

Figure 4.51 Characterization of the SiO_x Nanowires Using TEM Studies (a) Er (1e16 ions.cm^{-2}) seeded nanowire of diameter 60 nm with differential contrast along the body of the nanowire, (b) Selected area diffraction pattern (SAED) collected from the rectangular region indicating amorphous composition suggesting the presence of SiO_x: Er based on the extraction of d-spacing; also a smooth morphology of the nanowires could also be inferred from the SAED pattern, (c) Au:Er (Au - 3e16+ Er - 1e16 ions.cm^{-2}) catalyzed nanowire (diameter 70 nm) indicating a corrugated morphology and nanoscale particles of dark contrast, inset: SAED pattern collected from the rectangular region (from c) showing bright spots on the periphery of a concentric ring pattern along with random spots encircling a diffused outer ring. This configuration suggests the presence of non-homogenous Au clusters in combination with SiO_2: Er reminiscence based on the extraction of d-spacing and (d) High resolution TEM image indicating randomly dispersed nanoparticles on the nanowire ranging from 0.5 to 8.5 nm.

Optical emission spectra are shown in figure 4.52 for silica nanowires seeded by Au: Er, Er only and Au only. The emission from these nanowires at around 1.54 μm is characteristic of the $4I_{15/2}$ to $4I_{13/2}$ transition in erbium and is similar to that observed for Er-doped silica. The additional structure observed in spectra from Au:Er samples is particularly intriguing as it appears to be specific to the Au:Er system. Indeed, it has been observed for nanowire samples prepared using different methods, including co-deposition of Au and Er, but not for other metal combinations, such as Pd:Er or Ni:Er. Further work is required to resolve the origin of this effect. A comparison of the photoluminescence intensities from different samples must take into account the volume of active material produced under the different growth conditions. i.e. nanowires grown from Au: Er catalysts have a higher areal density and are expected to be longer than those produced from the Er-only catalyst. Figure 4.53 shows the integrated PL intensity normalized with respect to the areal coverage of nanowires, as summarized in Table 4.5. This shows that the PL intensity from nanowires catalyzed by Au:Er is significantly higher than from those catalyzed by Er-only when the Er fluence exceeds a threshold of around $3x10^{15}$ cm^{-2}. The photoluminescence intensity at low pump powers, I_{PL} is given by:

$$I_{PL} = \sigma \varphi \tau n / \tau_{rad} \quad (4.5)$$

Where, σ is the absorption cross section, φ the photon flux, τ the luminescence life-time, n the concentration of optically active Er ions, and τ_{rad} the radiative life-time of center. This shows that for fixed excitation conditions, the PL intensity depends on the product of the luminescence life time and the concentration of optically active Er ions.

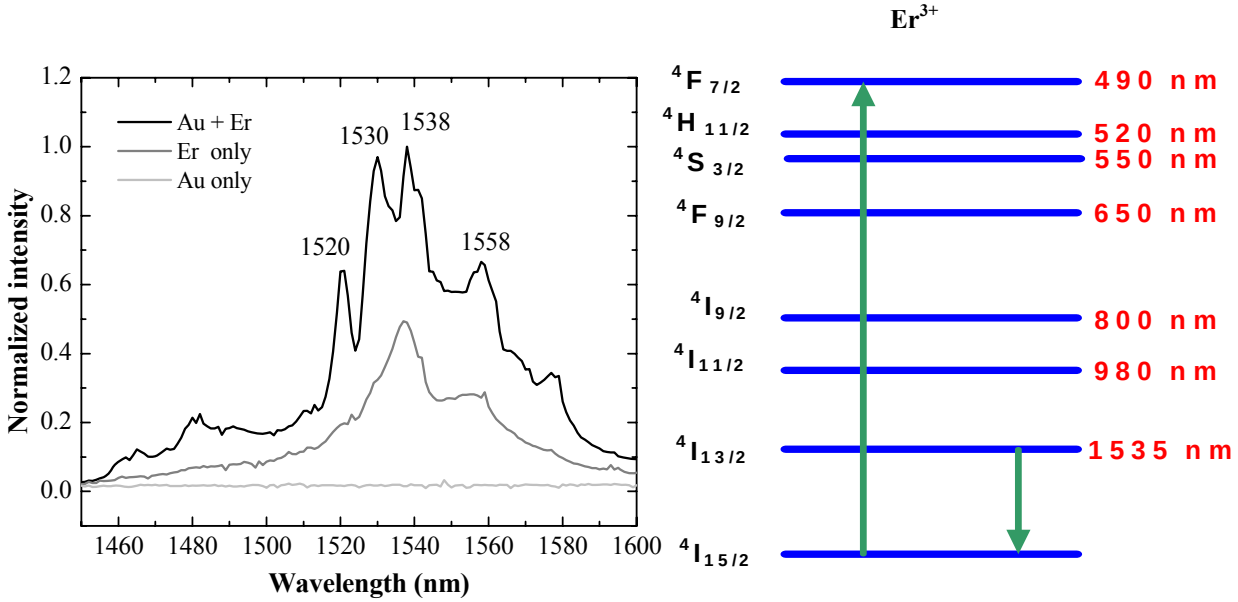

Figure 4.52 PL Spectra from Samples Showing a Characteristic Peak (Er^{3+} Transition) at 1538 nm for Both Au:Er and Er Catalyzed Silica Nanowires (for a constant Er^{3+} dose of $6x10^{15}$ ions.cm^{-2}).

The additional structure observed in spectra from Au:Er samples remains unexplained at present.

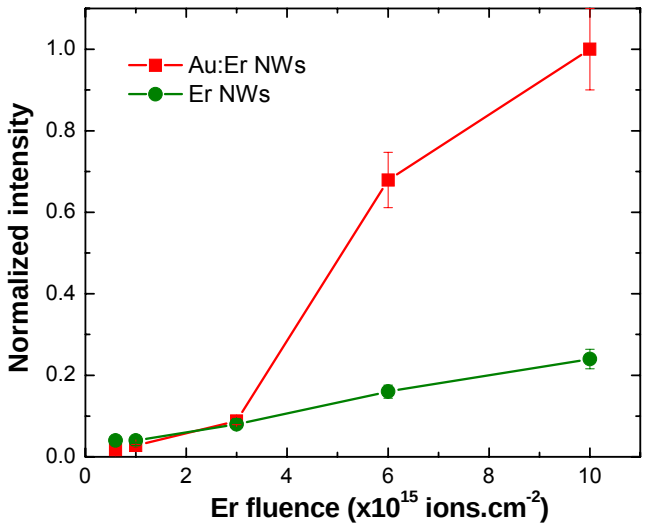

Figure 4.53 Normalized PL Intensity as a Function of Er Fluence

As inferred from the time resolved PL results, the maximum luminescence life time, irrespective of the catalysts, was found to be 24 ms at different fluence levels. It is 25 % higher than the highest value expected for Er in bulk silica (~18 ms). Confinement of Er ions within the nanowire is expected to reduce the available optical density of states for emission and thereby reduce the transition rate (i.e. increase in life time.) This could arise from the fact that erbium ions are effectively confined within a single-mode optical fiber (silica nanowire), thereby limiting the number of emission modes available; however, this effect would be improved by the complex morphology and curvature of the wires. Also, the augment in luminescence life time can largely be accounted for by the lower refractive index of the nanowire layer proportional to the refractive index of medium.

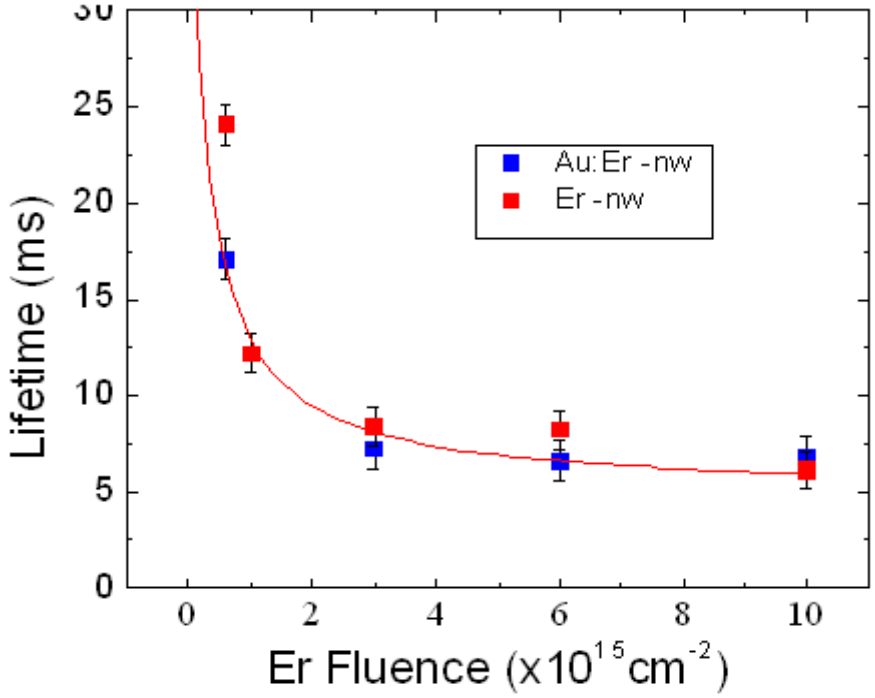

Figure 4.54 Luminescence Lifetime of the 1.5 μm Emission from Optically Active Silica Nanowires on Si

Si Samples implanted with: Au+ Er (30 keV Au; $3x10^{16}$ ions.cm^{-2}, 30 keV ErO$^-$; $6x10^{14}$ to $1x\ 10^{16}$ ions.cm^{-2}) + Er (30 keV ErO$^-$; $6x10^{14}$ to $1x\ 10^{16}$ ions.cm^{-2}). Results for a fused silica sample implanted with 150 keV ErO$^-$ is shown for comparison. The maximum luminescence lifetime was found to be 24 ms.

4.10.3 Conclusions

In summary, dense arrays of amorphous silica nanowires were synthesized by metal-catalysed VLS mechanism via self-organized Er implantation and Au: Er co-implantation based catalysis process. The nanowires nucleate following the float growth model with incorporation of Au and Er nanoparticles in an amorphous SiO_x shell in a single heat treatment. Structural and optical characterization of these nanowires highlights the dual role of Er as a catalyst and optical dopant. The optical emission from these wires exhibit features characteristic of the nanostructure. Further, the luminescence-lifetime of Er^{3+} ions was found to be 24 ms at room temperature. Infrared optical emission from erbium-doped silica nanowires is shown to have property characteristic of the material nanostructure and to provide the basis for the fabrication of integrated photonic devices and biosensors.

The ion-implantation based seeding methodology for nanowire growth offers several unique advantages such as:-

(a) The ability to use isotopically pure catalysts and optical dopants,
(b) The ability to control the size and distribution of the catalyst nanoclusters by varying the ion fluence, and
(c) Being an integral part of the substrate lattice, the process would be free from impurities

Taking into consideration the fact that detectable Er emission at room temperature in a crystalline semiconductor is often difficult to achieve, such an engineered nanosystem on Si holds a great potential for nanophotonics. Moreover, the self-organized metal-dielectric nanocomposite architecture could be tailored to further enhance the optical activity of Er to unprecedented levels by:-

(a) Varying the energy and fluence of Au implant,
(b) Using different Er fluence,
(c) Varying the aspect ratio of the nanowires via controlling the nanowire growth variables,
(d) The exploration of hybrid plasmonic configurations such as Ag and Au as catalysts and
(e) Systematic investigation of a combination of above mentioned processes

The metal decorated SiO_2 nanowire architecture in silicon would serve as a key functional block in nanophotonic devices. For example, such a configuration could enable the development of new surface enhanced Raman (SER) substrate on Si for ultrasensitive bioscreening applications with integrated microRaman laser. Moreover, optically active silica nanowires on Si enable the development high resolution optical head for near-field optical microscopy.

The oxide nanofibers rich in silicon are candidate electroluminescent materials for display and optoelectronics. In summary, an ensemble of these silica nanowires on Si would facilitate wavelength controlled optical nanoswitches and wavelength selective photoresponsive devices and would revolutionize Si based photonics.

4.11 Polyurethane Silica Nanowire Composite

The incorporation of amorphous silica nanowires into polyurethane is seen to influence the physical, mechanical and electrical properties of the host matrix. Thermal stability of hard and soft segments was found to improve with the addition of fillers. A 20 % increase in hardness and a 7.4% augment in Youngs' modulus have been recorded for the highest filler concentration of 1% silica in polyurethane.

Development of engineered polymer composites with inorganic fillers has led to a pool of mechanically robust multi-functional materials [37-39]. Further, escalating research interests and the need for cost-effective manufacturing schemes [40, 41] has facilitated the use of nano-sized fillers to effectively control/tune the macroscopic performance of the host. The additives with particle size in the nanometer range have small number of atoms per particle leading to different properties than the bulk. Additionally, an extremely large surface-to-volume ratio of these entities could induce a stronger interaction with the host matrix aided by the inter-particle distance, a function of particle diameter and concentration in the host. Extensive applications of nanocomposites derive from their fundamental behavior across several domains (such as physical, chemical, mechanical and electrical etc...). Probing such interactions would also provide a better understanding of the microcosm for efficient material design and application specific needs. However, limited property database restricts the visibility of certain scalable combination of materials.

One such sub set of engineered nanocomposites of profound interest include polyurethane (PU) based derivatives. Polyurethane is a robust polymeric material with superior mechanical strength, low temperature flexibility which possesses abrasion and oil resistance properties with varying hardness and elastic moduli. In addition, segmented PU has been the candidate material for developing vascular prostheses and implantable balloon stents [42-44]. However, they exhibit poor thermal stability. Also, there is a huge scope for improvement in mechanical properties. Addressing these needs, the investigations on polyurethane based nanocomposites could be broadly classified into organic and inorganic types based on the nature of the filler. Rehab at. al [45] has reported polyurethane–organoclay composite synthesized via in-situ polymerization. The motive of this work was to eliminate some disadvantages concerning with thermal stability and solvent resistance properties of conventional clay particles as fillers.

Also, polyurethane-organosilicate composite for anti-bacterial application has been demonstrated by Styan et al. [46]. On the other hand, inorganic additives in polyurethane has imparted fire retardant properties using Bi_2O_3 nanoparticles [47], magnetic properties by incorporating Fe_2O_3 [48] and shape memory attribute by carbon black [49] to mention a few. However, the flexibility in engineering PU for multi-functional applications has overlooked their mechanical instability.

It has been earlier established that dispersed clay particles as well silica based nanoscopic solids in PU act as effective reinforcing agents [50]. These inorganic moieties are chemically synthesized particles of uniform size and morphology. Su Chen at al [52] had employed 3-aminopropyltriethoxysilane (APTS) as a functionalization protocol to improve the stability and dispersion of the filler in the host. Earlier reports suggest the need for high concentration of silica and complex routes to strengthen PU. Very few studies have been devoted to high aspect ratio anisotropic silica nanostructures. The synthesis of polyurethane nanocomposites using silica nanowire as filler would be an interesting research subset that would update the database of scalable combination of materials for composites. This research article provides an insight into the physical, mechanical and electrical properties of the nanocomposite as a function of filler concentration.

4.11.1 Experimental

Fusion of polymer-inorganic matrix using a simple melting procedure would be beneficial for initial exploration. In this research, silica nanowires were synthesized by Pd thin film catalysis on silicon via the VLS mechanism.

The nanocomposite was synthesized by sonicating the isolated silica nanofibers in the (–NCO) PU prepolymer and chain extender to optimize dispersion. A small amount of catalyst (typically stannous octoate) was added. The resulting material was then placed in an oven at 107^0 C for two hours for curing. Three concentrations of the filler as weight percentages (0.1, 0.5 and 1) and untreated polymer formed the sample space for experimentation. This is in contrast to previously reported literature of a higher volume (>10 %) percentage of filler addition to enhance the host performance [53].

4.11.2 Results and Discussion

Analyzing these wires in TEM by a simple drop cast method, dense growth of interwoven nanowires was observed. The (EDS) image, shown as an inset (figure 4.55a) indicates the presence of Pd (used as a catalyst). In addition, the elemental composition of these nanowires were found to align with the SiO_x stoichiometry ($1.5<x<2$). The catalyst migration has been highlighted by the dark contrast spots along the nanowire body (figure 4.55b). Also, the results give an insight into the wetting characteristics of the surface. Non-uniform diameter of these wires could be attributed to the variation in seed size. The estimated diameter was found to be 80 nm. High aspect ratio of these nanostructures (50:1 to 10,000:1) as seen in figure 4.55c has been a strictly a function of growth time and nucleation kinetics.

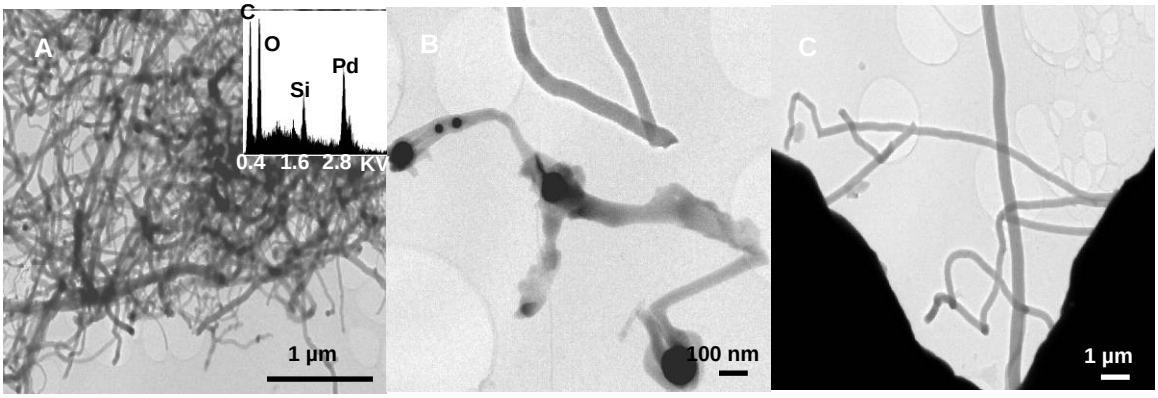

Figure 4.55 TEM Images of Nanowires Catalyzed by Pd Thin Film
(A) Dense intertwined wires showing dark contrast, Inset – Presence of Pd catalyst, SiO_x stoichiometry ; (B) Metal loaded silica nanowires of various size, average estimated diameter = 80 nm, (C) High aspect ratio nanostructures (40-800:1)

The morphology of the synthesized composite was studied under SEM and the TEM. SEM (figure 4.56a) results indicate a better dispersion of inorganic nanostructures in the segmented polyurethane. Anisotropic nanoparticles are seen distributed with some possible agglomeration in the host template as seen in the TEM image (figure 4.56b). Introducing the filler via sonication could be cited as possible explanation for the observed non-uniformity in size and shape. The EDS spectrum shows an elemental composition of C, Si and O (Inset). Absence of any phase separation is indicated by the diffused concentric ring in the selected area diffraction. The thermal properties were determined using thermogravimetric analysis (TGA).

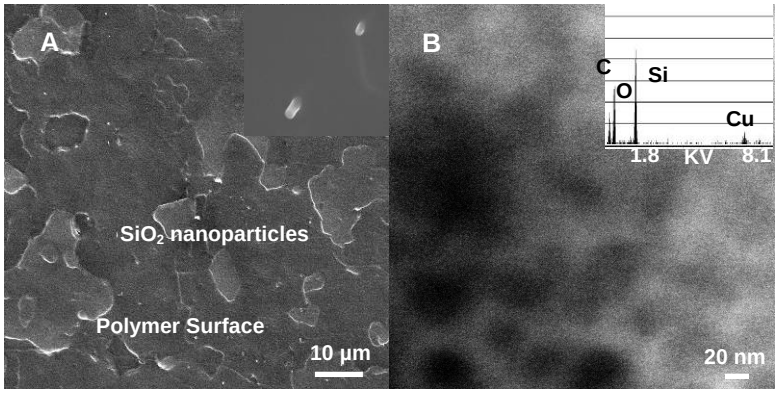

Figure 4.56 Polyurethane Nanocomposite Using Silica Nanowires as Filler (A) SEM image indicating dispersed whitish silica nanoparticles in the polymer matrix, Inset: Higher magnification SEM micrograph revealing nanowire outgrowth from the intentionally fractured polymer surface and (b) Dispersion of silica nanowires in the polyurethane host , Inset: EDX spectrum indicating the presence of C, Si and O

Results from table 4.6 comparing the thermal degradation properties of all samples indicate improved thermal resistance in the presence of SiO_2 NWs. It can be inferred that both soft and hard PU segments are thermally strengthened. However, the effectiveness of filler addition seems to saturate with 1% of the additives. This threshold value could be further extended by inducing additional ligand interaction via functionalizing the SiO_2 nanowires with APTMS (3-AminoPropylTriMethoxySilane). The glass transition temperature (T_g) was observed using differential scanning calorimetry (DSC). T_g remains constant irrespective of filler insertion (table 4.7). This confirms the absence of any plasticizer effect softening the host. Hard segments may be chemically bound to the nanowire surface reduced mobility.

Table 4.6 Thermo-Gravimetric Analysis

Degradation Temperature	PU Control (^{0}C)	PU NWs (0.1%) (^{0}C)	PU NWs (0.5%) (^{0}C)	PU NWs (1%) (^{0}C)
Soft Segment	313.5	330.3	329.4	321.3
Hard Segment	374.5	385.5	386	378.8

Table 4.7 Differential Scanning Caloriemetry Computation

Sample	Glass Transition Temperature (^{0}C)
PU Control	-74.6
PU NWs (0.1%)	-74.2
PU NWs (0.5%)	-74.6
PU NWs (1%)	-74.3

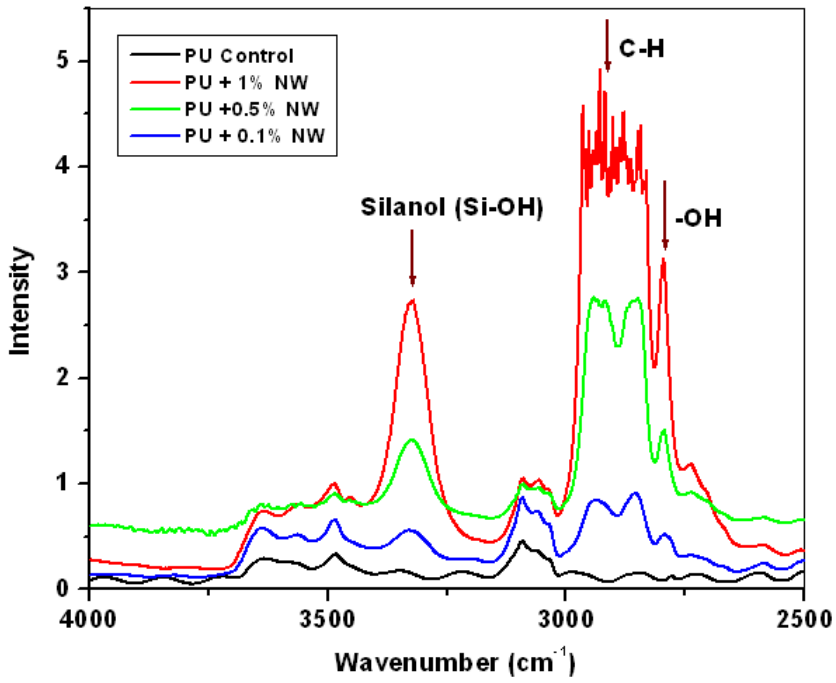

Figure 4.57 FTIR Spectrum Indicating the Presence of Silanol, Hydroxyl and Alkyl Groups in the Polyurethane-Silica Nanocomposite

Increase in the intensity of the functional group with rise in filler concentration has been observed.

The functional groups from the addition of silica nanowires in the polymer matrix are found to be as silanol (Si-OH), hydroxyl (-OH) and aliphatic stretching peaks from the FTIR (figure 4.57) spectrum.

Increase in the absorption magnitude of these functional groups with rise in filler concentration suggests the loading effect with a uniform dispersion in the polymer host rather than aggregation.

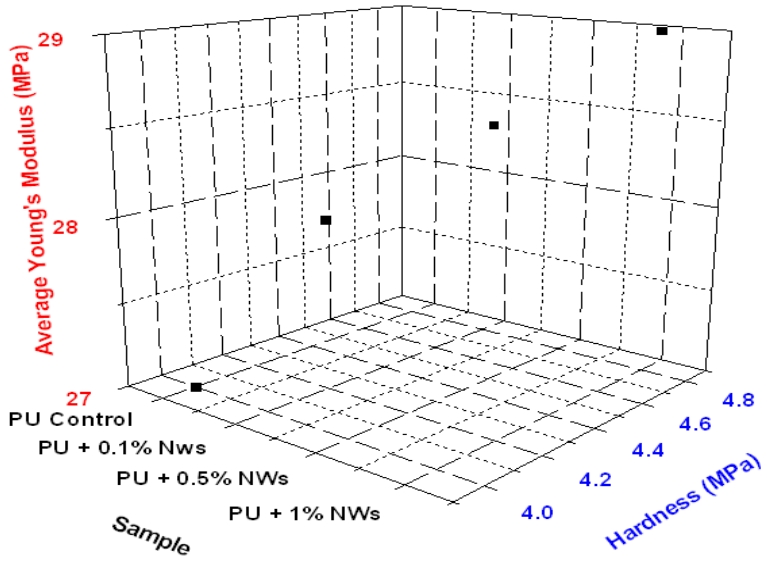

Figure 4.58 Variation of Youngs' Modulus (σ_M = 0.017 MPa) and Hardness (σ_H = 0.008 MPa) for Different Filler Concentrations

The elastic modulus and hardness data for the entire sample were calculated from indentation load-displacement experiments with a view to explore the mechanical properties. The nanoindentation tests were performed on MTS Nano Indenter XP (MTS Cooperation, Nano Instruments Innovation Center, TN, USA) in a constant depth mode. The depth was set to half the thickness (500 nm) of the polymer coating. The measurements were carried out on 16 random spots on the sample and averaged. Results (figure 4.58) indicate a 7.4% increase in averaged Youngs' modulus with addition of 1% silica nanowires. Also, a 20% augment in hardness has been observed for the composite with highest silica concentration. It is noteworthy to infer the closeness of the modulus and hardness values of polyurethane (control sample) obtained experimentally and standard literature [54]. The modest increase in the mechanical properties have been concurred by earlier reports [55] and the interaction between the wires and soft segment of the polymer reduces the mobility of the later thereby increasing the modulus.

4.11.3 Conclusions

Silica nanowires grown using Pt as a catalyst following a VLS mechanism has been used as reinforcing agents in polyurethane. The addition of silica nanowires has resulted in an increase in Young's modulus by 7.4 % and 20 % augment in hardness for a filler concentration of 1% silica in PU.

4.12 Summary

The experimental results and the associated discussions on manufacturing, characterization and applications of silica nanowires were presented. The next chapter will emphasize the future work based on these preliminary experimental results and the subsequent research thrusts.

4.13 References

[1] D.K.Sood, P.K.Sekhar and S.Bhansali, "Ion implantation based selective synthesis of silica nanowires on silicon wafers", Applied Physics Letters 88(2006), 143110

[2] G.K.Muralidhar, S.Bhansali, A.Pogany and D.K.Sood, "Electron microscopy studies of ion implanted silicon for seeding electroless copper films", Journal of Applied Physics 83 (1998), 5709

[3] I.G. Brown, "Vacuum ion sources", Review of Scientific Instruments, 65 (1994), 3061

[4] H. Baker, *ASM Handbook - Alloy Phase Diagrams* (ASM International, Materials Park, 1999), Vol. 3, Chap. 1, p.2.34

[5] V. Schmidt, S. Senz, and U. Gosele,"Diameter-dependent growth direction of epitaxial silicon nanowires", Nano Letters 5 (2005), 931

[6]. V. Schmidt, S. Senz, and U. Gosele, "The shape of epitaxially grown silicon nanowires and the influence of line tension", Applied Physics A 80 (2005), 445

[7] Y.Wu, Y.Cui, L.Huynh, C.J.Barrelet, D.C.Bell and C.M.Lieber, "Controlled Growth and Structures of Molecular-Scale Silicon Nanowires", Nano Letters 4 (2004), 433

[8] P.K.Sekhar, S.N. Sambandam, D.K.Sood and S.Bhansali, "Selective growth of silica nanowires in silicon catalysed by Pt thin film", Nanotechnology 17 (2006), 4606

[9] P.K.Sekhar and S.Bhansali, "Manufacturing Aspects of Semiconducting Nanowires", IEEE Transactions on Nanotechology", (Under Review), 2008

[10] T.Suzuki, “Effect of Annealing a Silicon Wafer in Argon with a Very Low Oxygen Partial Presuure”, Journal of Applied Physics 88 (2000), 6881
[11] K.Peng, H.Zhang, A.Lu, N-B.Wong, R.Zhang and S-T.Lee, “Ordered Silicon Nanowires via Nanospehere Lithography and Metal-Induced Etching”, Applied Physics Letters 90 (2007), 163123
[12] T.Suzuki, “Relation between the suppression of the generation of stacking faults and the mechanism of silicon oxidation during annealing under argon containing oxygen”, Journal of Applied Physics 88 (2000), 1141
[13] P.K.Sekhar, N.S.Ramgir and S.Bhansali, “Metal-Decorated Silica Nanowires: An Active Surface Enhanced Raman Substrate for Cancer Biomarker Detection”, Journal of Physical Chemistry C 112 (2008), 1729
[14] J. B. Hannon, S. Kodambaka, , F. M. Ross, and R. M. Tromp, “The influence of the surface migration of gold on the growth of silicon nanowires”, Nature 440 (2006), 69
[15] L. M. Hillyer, and B. Woodward, **“**Interleukin-10 concentration determined by sandwich enzyme-linked immunosorbent assay is unrepresentative of bioactivity in murine blood **“** Am. J. Reg. Integr. Comp. Physiol. 285 (2003), 1514
[16] G. D. Sockalingum, A. Beljebbar, J. Morjani, J.F. Angiboust, and M. Manfait, “Characterization of island films as surface-enhanced Raman spectroscopy substrates for detecting low antitumor drug concentrations at single cell level,” Biospec,. 4 (1999), 71
[17] R. B. Laughlin and J. D. Joannopoulos, “Phonons in amorphous silica” Phy. Rev. B 16 (1977), 2942
[18] R. Abdelali, B. Magali, and B. Claude, “Signature of small rings in the Raman spectra of normal and compressed amorphous silica “ Phy. Rev. B 68 (2003), 184202
[19] Y. Maruyuma, and M. Futamata, **“**Elastic scattering and emission correlated with single-molecule SERS” Jnl.Raman.Spec, 36 (2005), 581
[20] A.D. McFarland, M.A.Young, J.A. Dieringer and R.P Van Duyne, “Wavelength-Scanned Surface-Enhanced Raman Excitation Spectroscopy” J. Phys. Chem. B 109 (2005), 11279
[21] V. N. Pustovit and T. V. Shahbazyan, “Surface-enhanced Raman scattering on the nanoscale: a microscopic approach“, J. Opt. A: Pure Appl. Opt 8 (2006), S208
[22] P.K.Sekhar, N.S.Ramgir, R.K.Joshi and S.Bhansali, “Selective growth of silica nanowires using Au catalyst for optical recognition of Interleukin-10”, Nanotechnology 19 (2008), 255502

[23] L A Bauer, N S Birenbaum and G J Meyer, “Biological Applications of High Aspect Ratio Nanoparticles”, J.Mater.Chem. 14 (2004), 517

[24] M Paulose, O.K. Vargheese and C.A. Grimes, “Synthesis of Gold-Silica Composite Nanowires through Solid-Liquid-Solid Phase Growth”, J. Nanosci. Nanotech. 3 (2003), 341

[25] P. Kask, K. Palo, D. Ullmann and K. Gall, “Fluorescence-intensity distribution analysis and its application in biomolecular detection technology”, PNA 96 (1999), 13756

[26] J L Lou, L Tong and Y Zhizhen, “Modeling of silica nanowires for optical sensing” ,Optics Express 13 (2005), 2135

[27] Y.D.Glinka, S.H. Lin and Y-T. Chen, “Time-resolved photoluminescence study of silica nanoparticles as compared to bulk type-III fused silica”, Phy.Rev B 66 (2002), 035404

[28] R.G. Elliman,A.R. Wilkinson,T. Kima,P. Sekhar and S. Bhansali, " Ion beam synthesis and doping of photonic nanostructures", Nuclear Instruments and Methods in Physics Research B 266 (2008), 1362

[29] A. Polman, “Erbium implanted thin film photonic materials”, Appl.Phys.Rev. 82 (1997),1

[30] M.J.A. de Dood, J. Knoester, A. Tip and A. Polman, “Förster transfer and the local optical density of states in erbium-doped silica”, Phys. Rev. B71 (2005) 5

[31] E. Snoeks, A. Lagendijk and A.Polman, “Measuring and Modifying the Spontaneous Emission Rate of Erbium near an Interface “, Phys. Rev. Lett. 74 (1995), 2459

[32] P.K.Sekhar, R.G. Elliman, A.R. Wilkinson, and S. Bhansali, “Enriched Er Emission from Nanoengineered Si Surface”, The Journal of Physical Chemistry C: Letters, (In Print) (2008)

[33] J.F.Ziegler, J.P.Biersack, and M.D.Ziegler, “The Stopping and Range of Ions in Matter”, Lulu Press (2008)

[34] J.B. Hannon, S. Kodambaka, F.M.Ross, and R.M. Tromp, “The influence of the surface migration of gold on the growth of silicon nanowires”, Nature 440 (2006), 69

[35] K.W. Kolasinski, “Catalytic growth of nanowires: Vapor–liquid–solid, vapor–solid–solid, solution–liquid–solid and solid–liquid–solid growth”, Current Opinion in Solid State and Materials Science 10 (2006), 182

[36] W. Lu and C.M. Lieber, “Semiconductor nanowires”, J.Phys.D: Appl.Phys. 39 (2006) , R387

[37] F.Gao, “Clay/Polymer Composites: The Theory”, Materials Today 7 (2004), 50

[38] V.P.Veedu, A.Cao, X.Li, K.Ma, C.Soldano, S.Kar, P.A.Ajayan and M.N. G Nejhad, “Multifucntional Composites using Reinforced Laminate with Carbon Nanotube Forests”, Nature Materials 5 (2006), 457

[39] H.D.Wagner,"Nanocomposites:Paving the way to stronger materials", Nature, Nanotechnology 2 (2007), 742
[40] E.W.Gacitua, A.A.Ballerini and J.Zhang," Polymer Nanocomposites: Synthetic and Natural Fillers A Review" , Maderas. Ciencia y tecnología, 7 (2005), 159
[41] O.Breuer and U.Sundararaj, "Big returns from small fibers: A review of polymer/carbon nanotube composites", Polymer Composites 25 (2004), 630
[42] F.J.Davis and G.R.Mitchell, Polyurethane Based Materials with Applications in Medical Devices, Bio-Materials and Prototyping Applications in Medicine, Springer (2007)
[43] M.G.Jeschke, V.Hermanutz, S.E.Wolf and G.B.Koveker, "Polyurethane vascular prostheses decreases neointimal formation compared with expanded polytetrafluoroethylene", J Vasc Surg. 29 (1999), 168
[44] D.J.Wheatley, L.Raco, G.M.Bernacca, I.Sim, P.R.Belcher and J.S.Boyd, "Polyurethane: material for the next generation of heart valve prostheses?", European Journal of Cardio-Thoracic Surgery 17 (2000), 440
[45] A.Rehab, A.Akelah, T.Agag, and N.Shalaby, "Polyurethane-nanocomposite materials via in situ polymerization into organoclay interlayers", Polymer for Advanced Technologies 18(2007), 463
[46] K.Styan, M.Abrahamian, E.Hume, and L.A.Poole-Warren, "Antibacterial Polyurethane Organosilicate Nanocomposites", Key Engineering Materials 342 (2007), 757
[47] B.Son , T-S.Hwang and D-C.Goo, "Fire-Retardation Properties of Polyurethane Nanocomposite by Filling Inorganic Nano Flame Retardant", Polymer Society of Korea 31 (2007), 404
[48] Z.Guo, S.Park, S.Wei, T.Pereira, M.Moldavan, A.B.Karki, D.P.Young, and H.T.Hahn, "Flexible high-loading particle-reinforced polyurethane magnetic nanocomposite fabrication through particle-surface-initiated polymerization", Nanotechnology 18 (2007) 335704
[49] I.S.Gunes, F.Cao, and S.C.Jana, "Evaluation of nanoparticulate fillers for development of shape memory polyurethane nanocomposites", Polymer 49 (2008) 2223
[50] Y.Chen, S.Zhou, H.Yang, G.Gu and L.Wu, "Preparation and characterization of nanocomposite polyurethane", Journal of Colloid and Interface Science 279 (2004), 370
[51] Y.Zhu and D.Sun, "Preparation of silicon dioxide/polyurethane nanocomposites by a sol-gel process", Journal of Applied Polymer Science 92 (2004), 2013

[52] S.Chen, J.Sui and L.Chen, “Positional assembly of hybrid polyurethane nanocomposites via incorporation of inorganic building blocks into organic polymer”, Colloid Polym Sci, 283 (2004), 66
[53] P.K Sekhar and S.Bhansali, “Polymer – Silica Nanowire Composite”, Polymer, (2008) (Under review)
[54] Z.S.Petrovic, I.Javni, A.Waddon and G.Banheygi, “Structure and properties of polyurethane–silica nanocomposites”, Journal of Applied Polymer Science 76 (2000), 133
[55] R.C.R Nunes, J.L.C. Fonseca and M.R.Pereira, “Polymer-filler interactions and mechanical properties of a polyurethane elastomer”, Polymer Testing 19 (2000), 93

Chapter 5

Conclusions and Future Outlook

5.1 Conclusions

Selective manufacturing of silica nanowires on silicon has been demonstrated using metal ion implantation based seeding approach and thin film catalysis. While the former technique has the advantage of precise placement of catalyst and near to uniform growth, the latter offers inexpensive way to mass manufacture them. A unique feature of this synthesis methodology is the use of simple open tube furnace heated up to 1100^0 C in a high purity Ar ambient unlike the use of harmful gases like silane or complex processes like sol-gel. These nanowires exhibit high aspect ratio (~3000:1) and are amorphous in nature.

Time sequence study of the nanowire growth reveals a combination of VLS and oxide assisted models to be valid. Growth rate characteristics indicate an initiation period, prolific growth regime and steady state. Structural characterization at a high resolution indicates catalyst metal nanoclusters along its body. Upon functionalization, these metal decorated nanowires served as an effective SER substrate towards the detection of micromolar concentrations of interleukin-10. Further, the role of silica nanowires as an immunoassay template has been demonstrated through femtomolar detection of both interleukin-10 and osteopontin.

In addition, optically active silica nanowires were produced in a single heat treatment by ion beam doping of erbium and subsequent annealing. These nanostructures showed characteristic Er^{3+} emission spectra at 1.54 μm depicting representative nanoscale properties. Time resolved photoluminescence studies indicate superior emission and luminescence life time when compared to fused and bulk silica. Erbium was ion implanted in Si to induce silica nanowire with a view to improve the dispersion of Er in the nanowires. The use of Er as both catalyst and dopant to synthesize optically silica active nanowires has the potential to revolutionize the optical telecommunication industry. Also, silica nanowires have been used as a filler material in the synthesis of polymer nanocomposites of superior mechanical properties.

Among the one dimensional nanostructures, engineered silica nanowires on Si has the potential for several unique applications such as localization of light, low dimensional waveguides for functional microphotonics, scanning near field optical microscopy (SNFOM), optical interconnects on a futuristic integrated optical microchip, sacrificial templates, biosensors, and optical transmission antennae.

5.2 Future Tasks

Futuristic research thrust leveraging the reported results are as follows but not limited to:-

(a) Vertically Aligned Growth of Nanowires of Uniform Geometry

As nanowires will be a critical interconnect element of any nanosytem, the ability to produce them at a desired location, in a controlled manner, is of great importance. In addition, producing an ordered array of vertically aligned wires is critical for sensing applications. Nanowires can be grown vertically or in an aligned fashion using electric field assisted assembly (against gravity), porous alumina templates and self-assembly using bioengineered interfaces. Vertically aligned nanowires are easier to manipulate. Also, they offer more selectivity with greater surface coverage.

Various arrayed patterns of desired dimensions (typically 30-100 nm) would be transferred to the Si substrate via E-beam lithography (figure 5.1). Selective catalyst deposition would be achieved by metal deposition and lift-off process. Further, the nanowire growth would be initiated by heating the patterned Si substrate at 1100^0 C. As the size of the nanowires depend on the parent nanocluster, confining the geometry of the metal cluster enables controlled growth of the wire. As an alternate procedure, commercial anodic alumina (AAO) templates of various sizes (30-100 nm) would be used as masking structures during the metal implantation process. This in turn would constrain the size of the parent cluster and hence the geometry of the nanowires. Finally, the VLS model would be applied for nanowire growth using multi-metal catalyst combinations towards developing a hybrid system.

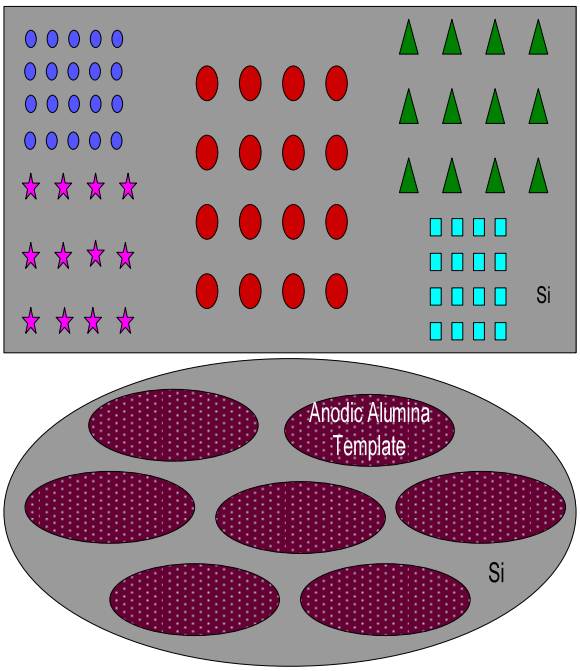

Figure 5.1 E-Beam Lithography (Top) and Templated Patterns (Bottom) for Selective Deposition of Metal Catalyst

(b) Low Temperature Growth of Nanowires on Polymer Substrates

Growing nanowires at low temperature on various substrates is critical for device applications. As mentioned in earlier sections, the presence of SiO is vital for silica nanowire growth. By employing a multi zone furnace, the SiO vapor can be produced in a high temperature zone which could be carried away by Ar to a low temperature zone (~200 C). Metals of very low melting/eutectic points such as indium or gallium can be coated onto a polymer substrate and metal thin film induced catalysis can be envisioned.

(c) LEAP (Local Electrode Atom Probe) Characterization and In-Situ TEM Investigation

The atom probe is a combination of a field ion microscope and a mass spectrometer, as shown in figure 5.2 [1]. Investigating silica nanowires using the LEAP would yield interesting results on the elemental composition and texture along the length of the wire. Also, looking at the nanowires at their early stage of growth using LEAP would provide fundamental details on nucleation and the role of catalyst inducing growth. Moreover, these results can give an insight on the growth model. For an accurate representation of the growth model, the growth must be studied in a more direct way. Many researchers have characterized and grown material within a TEM while observing the process in real-time.

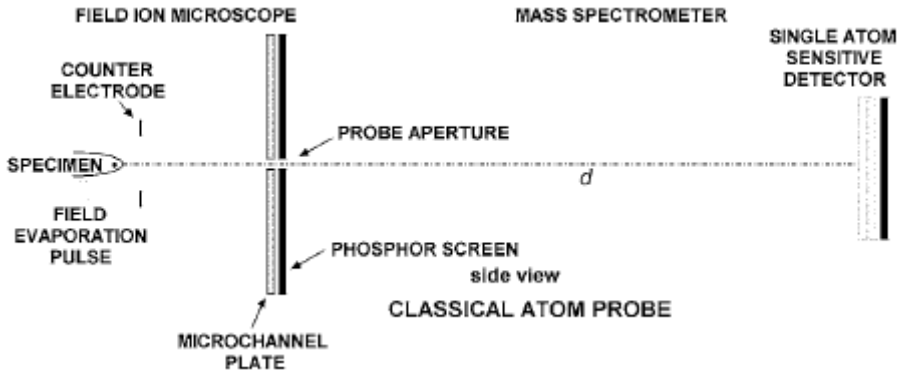

Figure 5.2 Schematic Diagram of the Atomic Probe
(Reproduced with Permission, [1])

(d) Probing Silica Nanowire – Human Cell Interaction

As mentioned earlier, the versatility of silica in synthesis aspects as well as surface modifications offers great advantage to the use of the material in bioanalysis. There is a rich database developed for surface modification of silica nanostrutcures. However, there is a research gap of investigating the nanowire-cell interaction which would provide a plethora of information on sub-cellular activities. The information, in turn, can be extracted to design drug delivery systems and biosensors. Investigating the cytotoxicity of these materials is of paramount importance. Using NIH/3T3 human fibroblast cells as our biological system, silica nanowires as well as silica nanoparticles at different concentrations: $100\mu gmL^{-1}$, $70\mu gmL^{-1}$, $30\mu gmL^{-1}$, $20\mu gmL^{-1}$ can be studied in vitro for cytotoxicity at different time periods: 4hrs, 8hrs, 12hrs, 24hrs, and 48hrs. The interaction between the cells and nanostructures will be studied using cell apoptosis assays, live/dead assays, viability and cytotoxicity assays.

(e) Surface Enhanced Raman Substrate for Single Molecule Detection

Silica nanowires can be coated with different metal nanoparticles such as Au, Ag and Cu of various sizes electrochemically to get a superior Raman enhancement (as a SER substrate) thereby engineering the system to detect single molecules, in particular, for cancer detection.

(f) Sacrificial Templates

Bulk silica has been routinely used in the MEMS industry as a sacrificial template in the fabrication of complex devices. In this context, the nanoscale silica wires forms an excellent template for the fabrication of bottom-up metallic nanostructures.

5.3 Summary

In this section, the experimental results are summarized and the futuristic research tasks have been mentioned. Manufacturing silica nanowires on Si has far reaching implications in interdisciplinary fields. Also, the current research investigation opens the gateway for using ion implantation as a general purpose nanoscale catalysis tool towards mass manufacturing bottom-up controlled nanosystems for wide variety of applications.

The envisioned goals and objectives bring in unique synergy of broad disciplines such as material science, engineering, manufacturing, physics and biology to realize an application specific complex microcosm. Such a research would provide a basis for students to work at the intersection of disciplines that will advance the knowledge and understanding in diverse field from basic science to field deployable applications

5.4 Reference

[1] T.F.Kelly and M.K.Miller , "Atom Probe Tomography", Review of Scientific Instruments 78 (2007), 031101

.

Appendices

Appendix A: Literature Review on Silica Nanowire Growth

Table A.1 Literature Review on the Various Approaches in Silica Nanowire Growth

Substrate	Type of Catalyst and Preparation	Growth Conditions			Mechanism	Reference et al.
		Temperature (C)	Time (min)	Ambient		
Glass, Si,Al_2O_3	Spu -Au, 15-90nm	CVD 350-1000	30	Ar	VLS	Wang L Nanotech. 2006
Si (111)	Ga, Ni Power $Ni(NO3)_2.H2O$	950	30	Ar/NH3	VLS	Cai, X.M. JAP 2005
Si	Ga Molten Droplets	700-950	10-60	$NH3_3$	VLS	Luo, S Small 2006
Si	NiO Powder	1000-1100	50-100	NH3	SLS	Park, B, Surf.Rev. Lett 2003
Fused Silica Capillary	2 Chloro-1,1,2 TriFluoroEthylMethyl Ether	400	720	-	VLS/VS	Woldegiorgis A, Electrophoresis 2004
Silica	Si, C and Co	1500	60	Ar	Solid Phase/ Gas solid Reaction	Zhu,Y.Q J.Mat.Chem 1998
Silica	Si/Si Powder	1400,Pyrolysis	12	N2	VS	Z.L.Wang, Adv Mat 2000
AAO	SiCl4, Wash CCl4	Hydrolysis			Surface Chem, Sol-gel	Kovtyukhova Adv Mat 2003
Fused Silica/Si (111)	-	1800, HFCVD	20	SiCl4+H2	-	Jih-Jen Wu, Av Mat 2002
Si	Molten Ga	520-900	5-300	Ar/O2	Extended VLS	L.Dai, Phy.Lett A 2005
Si (111)	Sn	980	2	Ar	VLS	S.H.Sun Solid.State.Commun. 2003
Si	MgO+Graphite Powder and Au	1100	45	Ar	VLS	S.Kar Solid.State.Commun. 2005
Si	Ga/In2O3	400	120	Ar/NH3	VLS	J.C. Wang Solid.State.Commun. 2003
Si	Si/Al2O3	1150	8-60	Ar	VLS	X.S.Fang Appl.Phys A 2005
SiO2	Au	1100	60	Ar	SVLS/OAG	Houlier Jnl of Phase Equ and Diffusion 2007
Si (100)	Co NPs	1100	120	Ar/H2/CH4	Coils	F.Wang JPC, 2007
Crucible	SiO (P) + Fe	850	240	Ar	VLS	D.P.Yu APL, 1998

Appendix A: Continued

Table A.1 (Continued)

Crucible	SiO (P) + Fe	850	240	Ar	VLS	D.P.Yu APL, 1998
Si	GaN	1150	300	Ar	Extended VLS	Z.L.Wang JACS 2001
Pellets	SiO2, FeNO3.9H2O, Active C Ball Mill	1350	180	Ar	Carbothermal Redn +VLS	X.C. Wu Chem.Phy .Lett 2001
Substrate	**Type of Catalyst and Preparation**	**Growth Conditions**			**Mechanism**	**Reference et al.**
		Temperature (C)	**Time (min)**	**Ambient**		
Si		800-1300	30	H2/H2O/ O2	Thermal Growth	J.Q.Hu Chem.Phy .Lett 2003
AAO	TEOS + Ethanol	1 Day Aging, 200 C-1 Day	-	-		Zhang 1999, J.Mat Sci.Lett
Si	Pd/Au , 1:1 Spu	1100	40	N2	VLS	Elechiguerra, ApplyPhys A 2001
Si (111)	Ni – 40 nm	950		Ar/H2	SLS	Yan Chem Phys Lett 2000
TiN/Ni/SiO 2/Si		1050	20	H2/Ar	Solid state reaction	K-H Lee Chem Phy Lett (2004)
Si + PMMA Mask	Ni	1100	20	Ar/H2	SLS	Ju Hung Hsu Nanotechnology 2006
Si	NiO, WO3	1100	60	Ar	SLS + Carbothermal	B.T.Park, Nanotech, 2006
Si	Sn + SiO	1320	420	Ar/H2	VLS+OAG	H.Wang Angew.Chem.Int(2005)
Si	Ga	1050	60	Ar/H2	VLS	Yiqin Chen Nanotech 2006

Appendix A: Continued

Table A.1 (Continued)

Si	CuO/C	1000	60	Ar	VLS + Carbothermal	Yu-Chiao Lin IEEE Nano 2005
Si	Thermal Evap, Laser Ablation, SiO Powder	800-1300	30	Ar	[111]	J-Q.Hu Adv.Mat 2003
Si	Ni + In2O3	650	45	N2/NH3	VLS	Renzlin Ma Chem.Phy .Lett 2003
Si (111)	Ni Sputter	1000	60	Ar/H/SiH 4	VLS	Niu Physica E 2004
Crucible	SiO + SnO	1180	240	Ar	VLS	J.Hu Small 2006
Si	Zinc Carbonate , Hydroxide and Graphite	1100	60		VLS	Q.Wei Solid.State Communc 2006
Graphite	Si Powder	1200	30	Ar/O2	VLS	K.S Wenger J.Mat.Chem 2003
Colloidal Particles	TEOS, Ethanol, HCl, H2O	80	30		Solution Grown	S-S Choi J.Mat.Sci Lett 2003

Appendix A: Continued

Table A.1 (Continued)

Ceramic Boat	SiO Powder + H2O	1200	60	Ar	VLS	Y.Hao APL, 2005
Alumina	Si Powder, SiO2, PbO, C	1200	90	Ar/O2	VLS	J.Zhang Jnl.Cryst. Growth, 2001
Si	Au	1000	180	N2/H2	SLS	Paulose M. Jnl.Nanosci and Nanotech.
Si	Fe	1200			Core-shell	Lieber, Science 1998

A.1 References

[1] L. Wang, D. Major, P. Paga, D. Zhang, M. G. Norton and D. N. McIlroy, "High yield synthesis and lithography of silica-based nanospring mats", Nanotechnology, 17, 298, 2006

[2] X. M. Cai, A. B. Djurišić, and M. H. Xie, "Growth of SiO*x* nanowire bunches cocatalyzed with Ga and Ni", Journal of Applied Physics, 98, 074313, 2005

[3] S. Luo, W. Zhou, W. Chu, J.Shen, Z. Zhang, L. Liu, D. Liu, Y. Xiang, W.Ma, and S. Xie, "Batchwise Growth of Silica Cone Patterns via Self-Assembly of Aligned Nanowires", Small, 3, 444, 2007

[4] B.T. Park and K. Yong, "Characterization of Silicon Oxide Nanowires Directly Grown From NiO/Si", Surface Review and Letters, 11, 179, 2004

[5] A. Woldegiorgis, K. Jansson, M. Curcio and J. Roeraade, "Nanowires for surface enlargement of narrow-bore fused-silica tubing", Electrophoresis, 25, 3660,2004.

[6] Y. Q. Zhu, N. Grobert, H. Terrones, Jonathan P. Hare, Harold W. Kroto, Wen Kuang Hsu, Mauricio Terrones and David R. M. Walton, "3D Silicon oxide nanostructures: from nanoflowers to radiolarian", J. Mater. Chem., 8, 1998, 1859

[7] Z. L. Wang, R. P. Gao, J. L. Gole, and J. D. Stout, "Silica Nanotubes and Nanofiber Arrays", Adv. Mater., 12, 24, 2000

[8] N. I.. Kovtyukhova, T. E. Mallouk, and T. S. Mayer, "Templated Surface Sol Gel Synthesis of SiO Nanotubes and SiO-Insulated Metal Nanowires", Adv. Mater., 15, 2003,780

[9] J-J. Wu, Te-Chi. Wong, and Chi-Chung. Yu, "Growth and Characterization of Well Aligned nc-Si/SiO Composite Nanowires", Adv. Mater., 14, 2002, 1643

Appendix A: Continued

[10] L. Dai, L.P. You, X.F. Duan, W.C. Lian, G.G. Qin, "Growth of silica nanowire arrays by reaction of Si substrate with oxygen using Ga as catalyst", Physics Letters A, 335 , 2005, 304

[11] S.H. Sun, G.W. Meng, M.G. Zhang, Y.T. Tian, T. Xie and L.D. Zhang, "Preparation and Characterization of oriented silica nanowires", Solid State Communications, 128, 2003, 287

[12] S. Kar andS. Chaudhuri, "Catalytic and non-catalytic growth of amorphous silica nanowires and their photoluminescence properties", Solid State Communications, 133, 151, 2005

[13] J.C. Wang, C.Z. Zhan and F.G. Li, "The synthesis of silica nanowire arrays", Solid State Communications, 125, 2003, 629

[14] X.S.Fang, C.H.Ye, T.Xie, G.He, Y.H. Wang and L.D.Zhang, "Synthesis and characterization of ultra-long silica nanowires", Appl. Phys. A, 80, 2003, 423

[15] DjamilaBahloul-Hourlier, "Thermodynamics of the Au-Si-O System: Application to the Synthesis and Growth of Silicon-Silicon dioxide Nanowires", Journal of Phase Equilibria and Diffusion, 28, 2007, 150

[16] F. Wang, M. Malac, R.F. Egerton, A. Meldrum, P. Li, M. R.Freeman and J. G. C. Veinot, "Controlled Growth of Silicon Oxide Nanowires from a Patterned Reagent", J. Phys. Chem. C, 111, 2007, 5

[17] D. P. Yu, Q. L. Hang, Y. Ding, H. Z. Zhang, Z. G. Bai, J. J. Wang, Y. H. Zou, W. Qian, G.C. Xiong, and S. Q. Feng, "Amorphous silica nanowires: Intensive blue light emitters", Applied Physics Letters , 73, 1998, 3076

[18] Z W. Pan, Z. R. Dai, Chris Ma, and Z. L. Wang, "Molten Gallium as a Catalyst for the Large-Scale Growth of Highly Aligned Silica Nanowires", J. Am. Chem.Soc, 124, 2002, 1817

[19] X.C. Wu, W.H. Song, K.Y. Wang, T. Hu, B. Zhao, Y.P. Sun and J.J. Du, "Preparation and photoluminescence properties of amorphous silica nanowires", Chemical Physics Letters, 336, 2001 , 53

[20] J.Q. Hu, Y. Jiang, X.M. Meng, C.S. Lee and S.T. Lee, "A simple large-scale synthesis of very long aligned silica nanowires", Chemical Physics Letters, 367, 2003, 339

[21] M. Zhang, Y. Bando, K.Wada, K. Kurashima, "Synthesis of nanotubes and nanowires of silicon oxide", Journal of Materials Science Letters 18, 1999, 1911

Appendix A: Continued

[22] J. L. Elechiguerra, A. Camacho-Bragado, J. Manriquez, J.P Zhou and M. Jose-Yacaman, "Growth of Amorphous SiO_2 Nanowires on Si using a Pd/Au ThinFilm as a Catalyst", Microsc Microanal, 10, 2004, 388

[23] H.F. Yan, Y.J. Xing, Q.L. Hang, D.P. Yu, Y.P. Wang, J. Xu, Z.H. Xi and S.Q. Feng, "Growth of amorphous silicon nanowires via a solid–liquid–solid mechanism", Chemical Physics Letters, 323, 2000, 224

[24] Ki-Hong Lee, Hyuck Soo Yang, Kwang Hyeon Baik, Jungsik Bang, Richard R. Vanfleet and Wolfgang Sigmund, "Direct growth of amorphous silica nanowires by solid state transformation of SiO_2 films", Chemical Physics Letters, 383, 2004, 380

[25] Ju-Hung Hsu, Ming-Hung Huang, Hsiao-Hsien Lin and Heh-Nan Lin, "Selective growth of silica nanowires on nickel nanostructures created by atomic force microscopy Nanomachining", Nanotechnology 17, 2006, 170

[26] B. T. Park and K. Yong, "Controlled growth of core–shell Si–SiO_x and amorphous SiO2 nanowires directly from NiO/Si" , Nanotechnology, 15, 2004, S365

[27] Yu-Chiao Lin, Wen-Tai Lin, "Growth of SiO_2 nanowires in presence of CuO/carbon mixed powders", Proceedings of 2005, 5th IEEE Conference on Nanotechnology

[28] J.-Q. Hu , X.-M. Meng, Y. Jiang, C.-S. Lee, S.-T. Lee, "Fabrication of Germanium-Filled Silica Nanotubes and Aligned Silica Nanofibers", Advanced Materials, 15, 2001 , 70

[29] R. Ma and Y. Bando, In–Ni microballs catalyzed growth of dense and highly aligned silica nanowires ", Chemical Physics Letters 377, 2003, 177

[30] J. Niua, J. Shaa; N. Zhangb, Y. Jia, X. Maa, D. Yanga; "Tiny SiO2 nano-wires synthesized on Si (1 1 1) wafer", Physica E, 23, 2004, 1

[31] J. Hu, Y. Bando, J. Zhan, X. Yuan, T. Sekiguchi, C. Li, and D. Golberg, "Silica Fibers with Triangular Cross Sections", Adv. Mater., 18 , 2006, 1852

[32] Q. Wei, G. Meng, X. An, Y. Hao, L. Zhang, "Synthesis and photoluminescence of aligned straight silica nanowires on Si substrate", Solid State Communications, 138 , 2006, 325

[33] K. Saulig-Wenger, D. Cornu, F. Chassagneux, T. Epicier and P. Mielea, "Direct synthesis of amorphous silicon dioxide nanowires and helical self assembled nanostructures derived therefrom", J. Mater. Chem., 13, 2003, 3058

[34] Sung-Seen Choi, S. G. Lee, S. Soon, S. H. Kim, Yong L. Joo, "Silica nanofibers from electrospinning/sol-gel process", Journal of Materials Science Letters , 22,2003, 891

Appendix A: Continued

[35] Y. Hao, G. Meng, C. Ye, and L. Zhang, "Reversible blue light emission from self-assembled silica nanocords", Appl. Phys. Lett. 87, 2005, 033106

[36] J. Zhang, F. Jiang, Y.Yang, J. Li, "Molten Pb as a catalyst for large scale growth of highly aligned silicon oxide nanowires", Journal of Crystal Growth 307, 2007, 76

[37] M. Paulose, O. K. Varghese, and C. A. Grimes, "Synthesis of Gold-Silica Composite Nanowires through Solid-Liquid-Solid Phase Growth", J. Nanosci. Nanotech., 2003, 3

[38] A M. Morales and C. M. Lieber, "A Laser Ablation Method for the Synthesis of Crystalline Semiconductor Nanowires", Science, 279, 1998, 208

Appendix B: Supplemental Materials

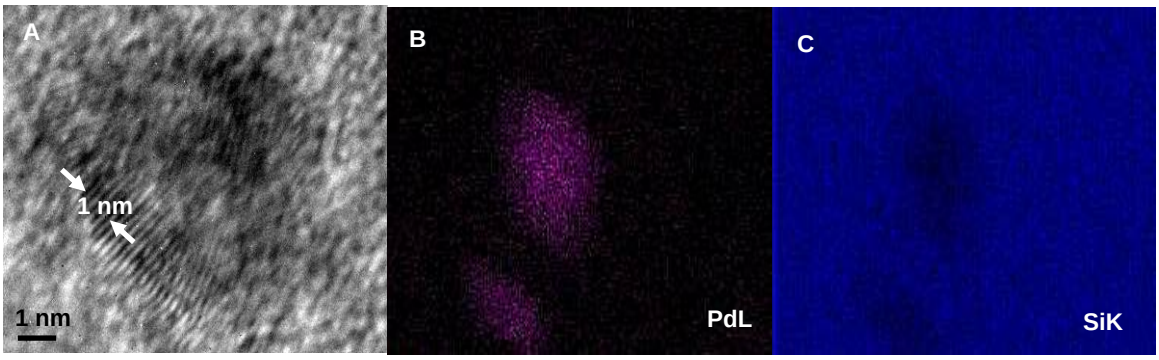

Figure B.1 Structural Composition of the Catalyst Particle Through TEM-EDS Studies (3E16 ions/cm^2, 1100^0 C, 60 mins)

(A) HRTEM Lattice Fringe Spacing = 0.25 nm indicating the presence of Pd (111), Average particle size = 6 nm, (B) EDS map showing Pd distribution (Source, figure 1B inset) and (C) EDS map of Si spread negating any silicide formation.

Appendix B: Continued

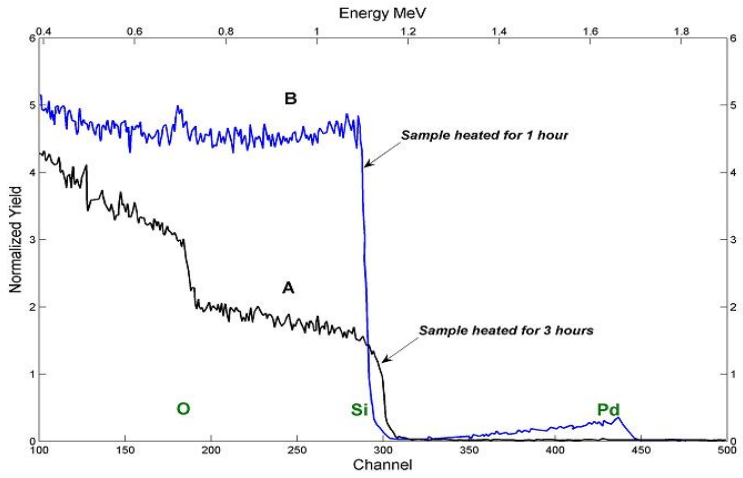

Figure B.2 Rutherford Backscattering Spectroscopy Indicating Catalyst Availability (Concentration) with Increase in Nanowire Growth (as a Function of Heating Time) (Incident beam of He ions at 2 MeV with a scattering angle of 160 degrees, Sample: 3E16 ions/cm^2, 1100 ^{0} C), (A) Sample heated for 3 hrs - Absence of Pd, catalyst action ceases to exist and (B) Sample heated for 1 hr – Presence of Pd, further growth of nanowires.

Appendix B: Continued

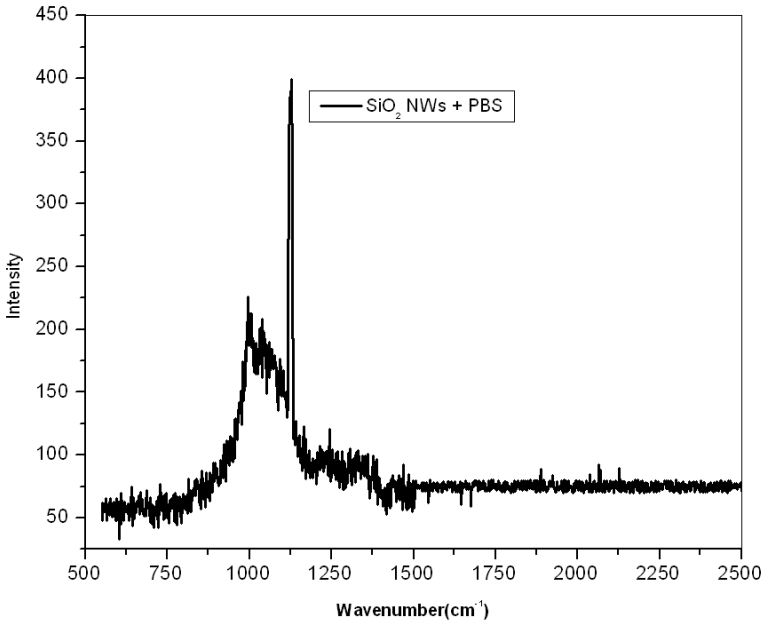

Figure B.3 Negative Control Experiment Using Phosphate Buffer Solution (PBS) as an Assay Target

MicroRaman Spectrum indicating the peaks of 994 and 1123 cm^{-1} devoid of activity around 2100 cm^{-1} suggesting the absence of IL-10.

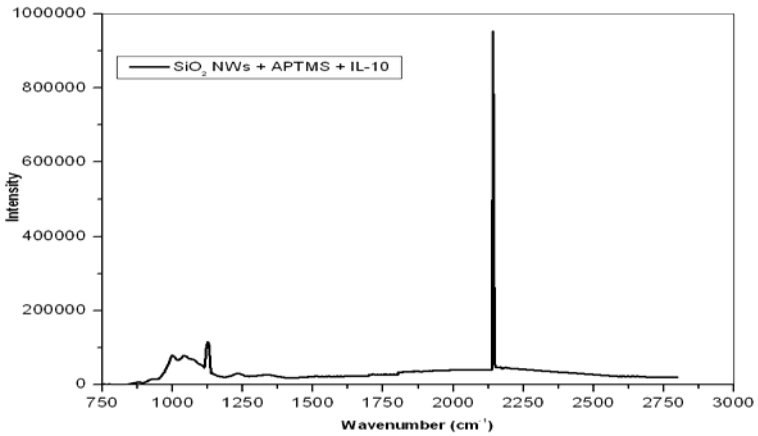

Figure B.4 Evaluation of Non-Specific Binding with the Attachment of IL-10 to Functionalized Nanowires in the Absence of Capture Antibodies

The Raman spectrum indicates the dominant signature of amine functionality at 2150 cm^{-1}.

Absence of IL-10 foot print around 2100 cm^{-1}

About the Author

Praveen Kumar Sekhar received the BE degree in Electrical and Electronics Engineering from Coimbatore Institute of Technology, Coimbatore, India in 2001 securing a distinction and MS in Electrical Engineering from University of South Florida (USF), Tampa, FL in 2005 with specialization in microelectronics. He is currently pursuing a PhD in Electrical Engineering at USF with specialization in nanosensors and bio-MEMS. As part of the Bio-MEMS and Microsystems Laboratory and Nanomaterials and Nanomanufacturing Research Center, his research includes nanoengineered materials for biosensing and photonic applications. In particular, his research focus is on manufacturing, characterization and applications of silica nanowires. The use of multi-functional materials for energy harvesting and exploring 'Nano-Bio' interface are his futuristic research interests.